Autophagy lipidation machinery regulates axonal microtubule dynamics but is dispensable for survival of mammalian neurons

Inaugural Dissertation

zur

Erlangung des Doktorgrades

Dr. rer. nat

der Mathematisch-Naturwissenschaftlichen Fakultät

der Universität zu Köln

vorgelegt von

Alberto Negrete Hurtado

Aus Esplugues de Llobregat

2020

Berichterstatter/in:	Dr. Natalia L. Kononenko
	Prof. Dr. Thorsten Hoppe
Verteidigung der Doktorarbeit:	19.09.2019

TABLE OF CONTENT

LIST OF FIGURES

ABBREVIATIONS

AAA	ATPases Associated with diverse Activities
AAV9	Adeno-associated virus serotype 9
Ac-TUB	Acetylated α-tubulin
AD	Alzheimer's disease
ATG	Autophagy-related protein/gene
AIS	Axon initial segment
APS	Ammonium persulfate
ATP	Adenosine triphosphate
BafA1	Bafilomycin A1
BDNF	Brain-derived neurotrophic factor
BSA	Bovine serum albumin
C	Celsius
CA1	*Cornu Ammonis* area 1 (Hippocampus)
cDNA	Coding DNA
CLASP	Cytoplasmic linker associated protein
CX	Cortex
deY α-TUB	Detyrosinated α-tubulin
DNA	Deoxyribonucleic acid
DMEM	Dulbecco's modified eagle medium
EB	Ending binding protein
EB3	Ending binding protein 3
ELKS	Protein-rich in glutamic acid (E), leucine (L), lysine (K) and serine (S)
EndoA	Endophilin A
ER	Endoplasmic reticulum
FBS	Fetal bovine serum
GABARAP	Gamma-aminobutyric acid receptor-associated protein
GABARAPL1	GABARAP-like 1, also termed as GEC1
GABARAPL2	GABARAP-like 2, also termed as GATE-16
GAPDH	Glyceraldehyde-3-Phosphate Dehydrogenase
GATE-16	Golgi-associated ATPase enhancer of 16 kDa
GEC1	Glandular epithelial cell protein 1
GFP	Green fluorescent protein
GTP	Guanosine triphosphate
HD	Huntington's disease
HEF 293T	Human embryonic fibroblasts 293 T cell line
HOPS	Homotypic fusion and protein sorting
HP	Hippocampus
HSP	Hereditary spastic paraplegia
ICC	Immunocytochemistry
IHC	Immunohistochemistry
kDa	kilodalton

KO	Knockout
LC3	Microtubule-associated protein 1 light chain 3
LC3I	Non-lipidated LC3
LC3II	Phosphatidylethanolamine lipidated LC3
LRRK2	Leucine-rich repeat kinase 2
LIR	LC3-interacting regions
MAP	Microtubule-associated protein
MAPK	Mitogen-activated protein kinase
MEFs	Mouse embryonic fibroblasts
MT	Microtubule
mTOR	Mammalian target of rapamycin
mTORC1/2	Mammalian target of rapamycin complex 1/2
Nes	Nestin
NBR1	Next to BRCA1 gene 1 protein
NDP52	nuclear domain 10 protein, also termed CALCOCO2
NGF	Nerve growth factor
ON	Overnight
OPTN	Optineurin
PCR	Polymerase chain reaction
PD	Parkinson’s disease
PE	Phosphatidylethanolamine
PI3K	Phosphatidylinositol 3-kinase
PI3P	Phosphatidylinositol 3-phosphate
PLCγ	Phospholipase C-gamma
P/S	Penicillin/Streptomycin
PTM	Posttranslational modifications
RAB7	Ras-related protein Rab-7
RFP	Red fluorescent protein
RNA	Ribonucleic acid
Rpm	Revolution per minute
RT	Room temperature
qRT-PCR	Quantitative real-time reverse transcription-PCR
SDS	Sodium dodecyl sulfate
SENDA	Static encephalopathy childhood with neurodegeneration in adulthood
siRNA	Short interfering RNA
SPG4	Spastic paraplegia type 4
SYB2	Synaptobrevin 2
Synj1	Synaptojanin 1
tau	Tau/MAPT
+TIP	Plus-end binding protein
-TIP	Minus-end binding protein
α-TUB	α-tubulin
Δ2-Tub	Δ2 α-tubulin

Tmx	Tamoxifen-inducible line
Trk	Tyrosine receptor-like
UB	Ubiquitin
UBL	Ubiquitin-like
UPS	Ubiquitin-proteasome system
VAMP8	Vesicle-associated membrane protein 8
VPS	Vacuole sorting protein
WB	Western blotting
WT	Wild-type
Y α-TUB	Tyrosinated α-tubulin

SUMMARY

Macroautophagy, hereafter referred to as autophagy, is a conserved degradation pathway that engulfs defective protein and cytoplasmic contents within autophagosomes for subsequent degradation intolysosomes. Such housekeeping role is especially important in neurons for two main reasons: First, neurons are postmitotic cells unable to dilute detrimental proteins and organelles by cell division. Second, these cells have extremely polarized structures, such as axons, which in humans can extend more than a meter long. Thus, neurons have evolved efficient and specialized mechanisms for the transport of cargo along axons, including autophagosomes, which must travel long distances along the microtubule (MT) cytoskeleton to finally fuse with lysosomes located at the cell soma. Impaired autophagosomal trafficking in axons hallmarks the pathology of many neurodegenerative disorders, whereas neuronal-confined knockout (KO) of several AuTophaGy (ATG)-related genes causes axonal pathology and neurodegeneration. Despite the critical importance of autophagy for the brain function, the precise physiological mechanism by which neurons with impaired autophagy undergo neurodegeneration remains obscure. Here in this thesis, I report on a novel role of core ATG proteins in the regulation of MT dynamics by using brain-confined mouse models and primary neuronal cultures lacking autophagy. Specifically, I found that ATG proteins required for the LC3 lipid conjugation are dispensable for the survival of forebrain excitatory neurons. Besides, the loss of the LC3 conjugation machinery impairs axonal trafficking and reveals axonal pathology. This phenotype is found to be independent of defective protein degradation and instead caused by the accumulation of a complex comprised by LC3, the active zone protein ELKS1, and the MT-stabilizing protein CLASP2. Finally, this thesis reveals that LC3-ELKS-mediated hyperstablilization of MTs impair the normal neurotrophic signaling in neurons. Taken together, this work reveals a new role for the LC3 function in the stabilization of MTs along the axon, which may help to understand better the physiopathology on neurodegenerative diseases.

ZUSAMMENFASSUNG

Makroautophagie, im Folgenden nur noch als Autophagie bezeichnet, ist ein evolutionär konservierter Prozess zum Abbau von mangelhaften Proteinen und cytoplasmischen Inhalten in Autophagosomes, mit anschließender Degradierung in Lysosomen. Dieser Prozess ist besonders wichtig für Neuronen, da es sich bei ihnen um postmitotische Zellen handelt. Sie untergehen keine Zellteilung und können die schädlichen Proteine somit nicht verdünnen. Zudem besitzen sie extrem polarisierte Strukturen, wie zum Beispiel Axone, welche in Menschen länger als einen Meter sein können. Deswegen haben Neuronen einen effizienten und hochspezialisierten Mechanismus entwickelt um Zellinhalte entlang des Axons zu transportieren, darunter auch Autophagosomen. Diese werden entlang des Mikotubuli (MT) Cytoskeletts zum Zellsoma transportiert wo sie mit den dort lokalisierten Lysosomen verschmelzen. In zahlreichen Neurodegenerativen Erkrankungen dient der beeinträchtigte Transport von Autophagosomes entlang des Axons als Kennzeichen, während der knock-out (KO) von verschiedenen AuTophaGy (ATG) zugehörigen Genen zu Neurodegeneration führt. Obwohl der Prozess der Autophagie in Neuronen von besonderer Wichtigkeit für die Gehirnfunktionalität ist, sind die physiologischen Mechanismen, durch die Neuronen bei eingeschränkter Autophagie zugrunde gehen, noch immer unklar. Mit dieser Arbeit möchte ich eine neue Funktion der wichtigsten ATG Proteine aufzeigen. Dazu arbeite ich mit auf das Gehirn begrenzten Mausmodellen und primären Neuronen in Kultur, in denen einzelne ATG Proteine nicht mehr exprimiert werden. In diesen Modellen zeige ich den Einfluss von ATG Proteinen auf die MT Dynamiken. Genauer gesagt habe ich herausgefunden, dass ATG Proteine, die für die Lipid Konjugation von LC3 notwendig sind, verzichtbar für das Überleben von exzitatorischen Vorderhirnneuronen sind. Jedoch führt ein Fehlen dieser zur Beeinträchtigung des Transportes entlang des Axons, sowieSchwellungen. Dieser Phänotyp präsentiert sich unabhängig von dem Prozess der Degradierung und ist begründet in der Anhäufung eines Komplexes bestehend aus LC3, dem aktiven Zonen Protein ELKS1, und dem MT stabilisierenden Protein CLASP2. Diese Arbeit zeigt, dass LC3-ELKS vermittelte Hyperstabilisierung von MTs die normale neurotrophe Signalübertragung in Neuronen beeinträchtigt.Zusammengefasst wurde eine neue Funktion von LC3 in der Stabilisierung der MT entlang des Axons aufgedeckt, welche zu einem besseren Verständnis der Pathologie von Neurodegenerativen Erkrankungen beitragen könnte.

1. INTRODUCTION

1.1 Microtubule-based transport in neurons

Neurons are extremely polarized cells typically characterized by a single axon and multiple dendrites which defines the pre- and post-synaptic regions, respectively. Indeed, some neurons are found to extend their axons for more than a meter long in humans (Stifani, 2014). These two properties of polarized morphology and length enforce the need for proteins and organelles to be actively transported between neuronal compartments (Terenzio et al., 2017). In fact, given that the passive diffusion of macromolecules has long-distance limitations and slow diffuse ratios (Wiegert et al., 2007), neurons highly rely on motor-driven mechanisms along the cytoskeletal architecture of the cell to achieve efficient intracellular communication and an effective neuronal function (Kapitein and Hoogenraad, 2015).

Among all different cytoskeletal components, microtubules (MTs) have been pointed out as critical structures for neuronal function. They play a fundamental role in the maintenance of axonal homeostasis: provide tracks for intracellular transport (Maday et al., 2014), produce cellular forces during development and cell division (Forth and Kapoor, 2017; Singh et al., 2018), and behave as platforms for the recruitment of signaling factors (Akhmanova and Steinmetz, 2008). Indeed, intracellular transport of membrane-bounded vesicles, organelles, and proteins must undergo anterograde (from the cell body to the periphery) and retrograde (from the periphery to the soma) transportalong neurites (axons and dendrites), a movement orchestrated by MT motor proteins (Maday et al., 2014). Such functions have been shown to be crucial in neurons since mutations in several tubulin isotypes and MT-related proteins are causative of several neurodevelopmental and neurodegenerative diseases, such as mutations in the α-tubulin isotype TUBA4A, associated with amyotrophic lateral sclerosis (Smith et al., 2014), or tau, which impair axonal transport in tauopathies (Kapitein and Hoogenraad, 2015; Yang et al., 2013).

1.1.1 Microtubule organization and dynamics

MTs are cytoskeletal polymers, composed of α- and β-tubulin heterodimers. These heterodimers assemble into linear protofilaments that associate laterally and form a hollow tube with an outer diameter of 25 nm (Howard and Hyman, 2003). MTs are also dynamic structures that undergo phases of growth and disassembly, a process called dynamic instability. This dynamic feature contributes to MTs properties to grow or retract under different conditions. Dynamic instability is given by the head-to-tail association of the α/β heterodimers, resulting in a polarized structure

which produces different polymerization rates at the two ends. β-tubulin monomers point towards the faster-growing end (plus end) and α-tubulin monomers toward the slower-growing end (minus end) (Akhmanova and Steinmetz, 2008). MT assembly and dynamics have been commonly attributed to the hydrolytic activity of the ß-tubulin: free ß-tubulin spontaneously binds to guanosine triphosphate (GTP) and promote polymerization and stabilization of growing MTs tips, whereas the hydrolysis of GTP to GDP provides structural instability, making MTs prone to depolymerization, or “catastrophe”, a period of rapid shrinkage (Alushin et al., 2014).

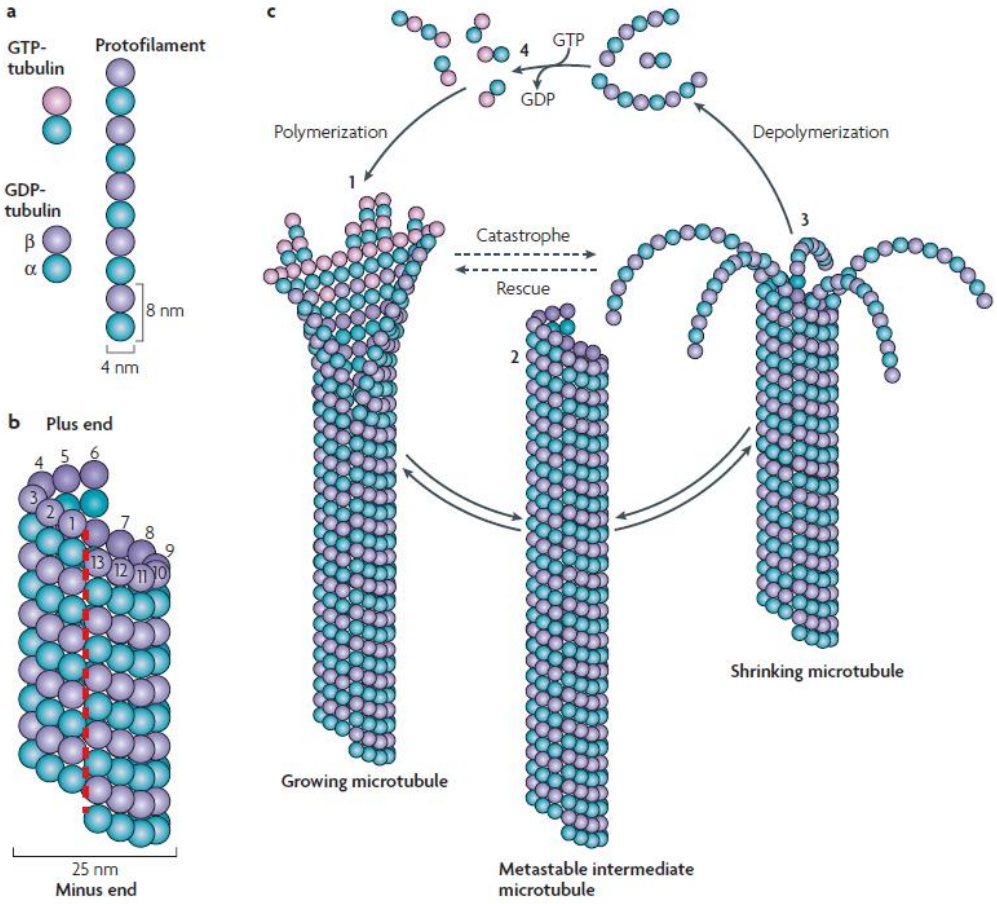

Figure 1. Schematic illustration of MT structure and dynamic instability. (**a**) α/β-tubulin heterodimers align to form a protofilament. (**b**) Protofilaments associates in a cylindrical manner to form a MT with a diameter of 25 nm. (**c**) MT polymerization depends on the incorporation of GTP-loaded tubulin subunits, whose GTP undergo hydrolysis shortly after incorporation and increases the chance of a catastrophe event. The figure is taken from Akhmanova and Steinmetz (2008).

Parallel bundles of MTs are differently organized in axons and dendrites. Axons display a uniform array of MTs with plus-end-outward orientation, whereas dendrites have equally mixed oriented

MTs (Yau et al., 2016). It is widely assumed that these different network properties provide the basis for cargo selectivity between axons and dendrites (Tas and Kapitein, 2018). Indeed, some motor proteins are found to be axon-specific, such as the kinesin-1, which preferentially binds to the minus-end of stable MTs, which are only found in the initial segment of the axon. In contrast, stable MTs in dendrites are only found to be plus-end-inward, blocking the access of kinesin-1 to the dendrites (Tas et al., 2017). In addition, cargo selectivity is also determined by the formation of the axon initial segment (AIS), a specialized zone involved in action potentials generation and filtering of intracellular cargos (Gumy and Hoogenraad, 2018; Lazarov et al., 2018). This axonal segment is characterized by the presence of tripartite motif 46 (TRIM46), a protein important for generating parallel MT bundles near the AIS (van Beuningen et al., 2015).

MT organization and dynamics crucially relies upon several regulatory factors such as different tubulin isoforms, post-translation modifications, and microtubule-associated proteins (MAPs). According to the mode of function, MAPs can be roughly classified into five groups: (1) modulators of MT number, such as regulators of nucleation, MT severing proteins, and minus-end targeting proteins (-TIPs); (2) motor proteins, such as kinesin and dynein; (3) regulators of MT dynamics, such as plus-end tracking proteins (+TIPs) and MT depolymerizers; (4) cross-linking proteins that align and form MT bundles, such as the classical MAPs; and (5) enzymes involve in the generation of post-translation modifications of tubulin, which allows the formation of distinct MT subtypes (Emoto, 2016).

MT nucleation, or *de novo* MTs formation, is typically initiated by the γ-tubulin ring complexes (γ-TuRCs), which commonly localize at the centrosome and form a structure where MTs emerge, called the MT organizing center (MTOC) (Teixido-Travesa et al., 2012). In neurons, it was initially believed that MTs were generated at the MTOC, cut and distributed through the cell. However, recent studies have demonstrated that neurons lacking the centrosome display normal MT network and morphology (Kapitein and Hoogenraad, 2015; Stiess et al., 2010). Alternatively, γ-TuRCs have been shown to nucleate MTs in both dendrites and axons at the Golgi apparatus or along existing MTs in a centrosomal-independent manner (Efimov et al., 2007; Sanchez-Huertas and Luders, 2015), a process, which is accentuated during neuronal maturation (Yau et al., 2014).

Another mechanism to form new MT arrays involves the use of severing enzymes, which cut the pre-existing MTs to generate templates for the elongation of new MTs. Fidgetin, katanin, and spastin are the three classes of MT-severing enzymes so far identified, all of which are members of the ATPases Associated with diverse cellular Activities (AAA) superfamily, involved with protein disassembly and unfolding activities (Erdmann et al., 1991; Frickey and Lupas, 2004). All three

severing enzymes are highly expressed in the nervous system and, particularly, katanin and spastin are described to have crucial roles in neuronal morphogenesis, function, and plasticity (Kapitein and Hoogenraad, 2015). Katanin is proposed to stimulate dendritic and axonal outgrowth by releasing MTs from centrosomes and cutting them off in segments to be transported along the neurites during neuronal morphogenesis, but also to play roles in other maturations stages and compartments (Sharp and Ross, 2012). Interestingly, it has been reported that tau, another MAP, protects MTs from katanin-severing activity, suggesting a regulatory mechanism which may be impaired in Alzheimer's disease (AD), where the MT number is found to be decreased (Brunden et al., 2017; Qiang et al., 2006). Sapstin is also active at different stages of neuron maturation, but in contrast with katanin, its function is not strongly affected by the presence of tau (Lacroix et al., 2010). Interestingly, spastin is reported to have specific influences on the organization of axonal MTs, since spastin mutations have been directly linked to axonal pathologies in hereditary spastic paraplegia (HSP), also referred as spastic paraplegia type 4 (SPG4) (Fink, 2013).

Intracellular cargos are transported in neurons by motor proteins. These motor proteins undergo cycles of adenosine triphosphate (ATP) hydrolysis and subsequent release of hydrolysis products to induce conformational changes and interactions with the cytoskeleton, which result in the generation of mechanical forces able to move the motor protein and the associated cargo (Sweeney and Holzbaur, 2018). In axons, two types of transport can be distinguished: the fast transport of membranous organelles, which move at a speed of ~1 μm/s, and the slow transport of some cytosolic proteins and cytoskeletal proteins, which achieve the speed of <0.1 μm/s (Maday et al., 2014). Motor neurons are classified into three superfamilies, the myosins, the kinesins, and the dyneins. Myosins are the motor proteins found in the actin networks, where they play important roles in presynaptic terminals and postsynaptic spines for proper synaptic function. In contrast, MTs, act as a major longitudinal cytoskeletal filament in axon and dendrites, allowing long-distance trafficking by serving as tracks for kinesins and dyneins, which in general move towards the MTs plus-end and minus-end, respectively. Kinesin family is composed by 45 *Kif* genes in humans and mice (38 of which are expressed in the brain (Miki et al., 2001)), which in turn are classified in 14 classes (kinesin- 1-14). All these different kinesins possess different tail regions that allow selectivity for cargo recognition and function, although these specific functions of each KIF are sometimes redundant. Dyneins, in contrast, have only two heavy chain family members, but it acquires cargo selectivity through direct binding or recruitment of multiple light/intermediate chains and dynactin complexes (Hirokawa et al., 2010; Maday et al., 2014).

The heterogeneous superfamily of +TIPs specifically accumulates at the plus end of MTs to control MTs dynamics, growth directionality, and crosstalk between MTs and the actin cytoskeleton. The most conserved and ubiquitous +TIPs are the end binding proteins (EBs). These are well-studied proteins, which are localized at the core of +TIPs complexes and able to autonomously track growing MTs plus ends and bind to numerous other regulatory proteins (Zhang et al., 2015). Mammalian cells express three members of the EB family, (EB1, EB2, and EB3), where EB1 and EB3 have been shown to have a stronger capacity to bind and track growing MTs (Komarova et al., 2009). Another family of +TIPs is the cytoplasmic linker associated proteins (CLASPs), which are also widely conserved in fungi, plants, and animals (Tirnauer and Bierer, 2000). Mammalian CLASPs are represented by two homologs, the ubiquitously expressed CLASP1, and the brain-enriched CLASP2. Both proteins prevent the catastrophe onset via direct interaction with MTs (Aher et al., 2018; Akhmanova and Steinmetz, 2010). Interestingly, studies in HeLa cells have demonstrated that CLASPs can localize to cortical regions and stabilize MT plus ends via its interaction with ELKS ("protein-rich in glutamic acid (E), leucine (L), lysine (K) and serine (S)", also known as CAST2, Rab6IP2, or ERC1) (Lansbergen et al., 2006). ELKS is a scaffolding protein expressed by two ELKS genes, Erc1 and Erc2, to produce ELKS1 and ELKS2, respectively. In neurons, ELKSs are mostly localized at the presynaptic active zone, where they are known to interact with other scaffolding proteins, such as RIM, Munc13, and Piccolo/Basson, forming multi-protein complexes that regulate synaptic vesicle exocytosis (Held and Kaeser, 2018). However, whether ELKS interacts with CLASPs to regulate MT stability in neurons is currently not known.

Classical MAPs, including MAP1, 2, 4, 6, 7, 9 and tau (also referred as structural MAPs), are generally showed to bind along the MT lattice and regulate MT polymerization, bundling, and stabilization. Despite that, the different MAPs' families possess unequal functions and characteristics (Emoto, 2016). MAP2 is the most abundant structural MAP in the brain, which is mainly expressed in neurons, but also detected in oligodendrocytes and astrocytes (Geisert et al., 1990; Muller et al., 1997). MAP2 isoforms are classified into high and low molecular weight proteins. Among all different isoforms, MAP2A is the most predominant one in the adult brain (Nunez, 1988). Moreover, and in contrast to low molecular weight MAP2, high molecular MAP2 is selectively localized in the soma and the dendrites. Next to its main function to bundle the MTs, MAP2 has also been shown to interact with several proteins and regulate processes such as neuronal plasticity and signaling (Emoto, 2016). Another interesting and much-studied structural MAP is tau/MAPT (tau). Mainly expressed in neurons and specifically localized in axons, tau is expressed in several isoforms during different stages of neuron maturation, and it is regulated by

different post-translational modifications, such as phosphorylation. Under pathological conditions, tau mislocalizes to dendrites and synaptic spines and impairs synaptic function, causing MT severing by spastin, traffic jams, and synapse loss (Zempel and Mandelkow, 2014).

MT dynamics are also intrinsically regulated by post-translational modifications (PTM) of tubulin subunits, including detyrosination, Δ2-tubulin generation, glutamylation, glycylation and acetylation (Janke and Kneussel, 2010; Witte et al., 2008). α-tubulin genes encode for a protein which contains a carboxy-terminal tyrosine. This tyrosine is reversely removed by detyrosination (unknown enzyme) in polymerized MTs and re-added by the tubulin tyrosine ligase (TTL) (Raybin and Flavin, 1977) in soluble tubulin. Following detyrosination, an additional amino acid residue of glutamate can be removed from the C-terminal tail of α-tubulin to generate Δ2-tubulin, a process mediated by deglutamylase enzymes and believed to be irreversible (Erck et al., 2005). Acetylation of the Lys40 of α-tubulin, similar to detyrosination, takes place on the MT polymers but is contrary to the rest of PTMs, it occurs in the lumen of MTs (Ly et al., 2016). Finally, (poly)glutamylation and (poly)glycylation are PTMs that are generated by the enzymatic addition of one or more glutamate or glycine residues as branched peptide chains to the C-terminal tails of α- and/or ß-tubulin, and are believed to regulate MT-MAP interactions (Song and Brady, 2015).

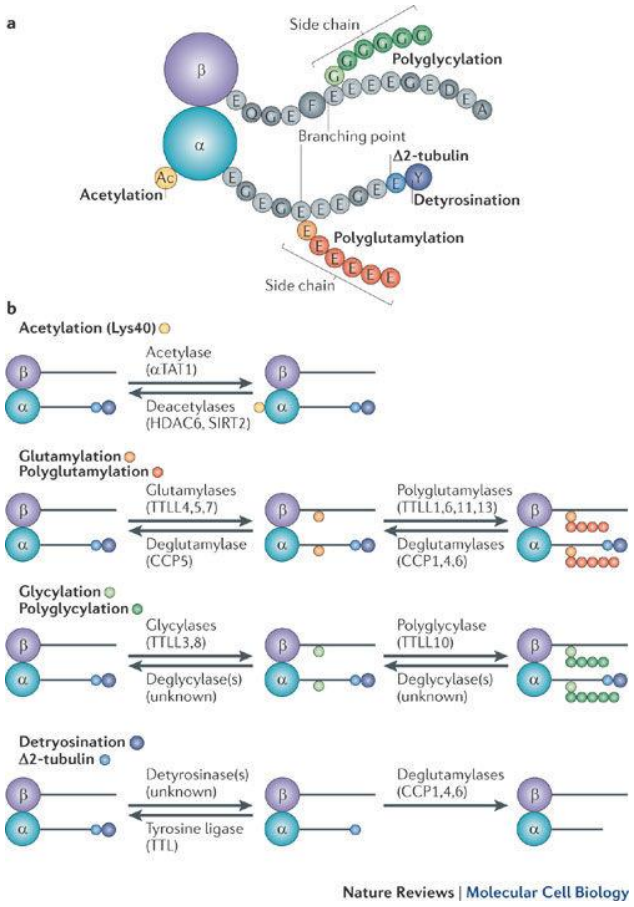

Figure 2: Schematic illustration of an α-tubulin and ß-tubulin dimmer and their PTM modifications. (a) PTM modifications of tubulin are mostly occurring in the carboxy-terminal tails of the α- and ß-tubulin. Detyrosination of the last Tyr residue and the irreversible follow-up removal of the penultimate Glu residue (Δ2-tubulin) are specific of the C-terminal tail of the ß-tubulin. Polyglutamylation and polyglycylation can occur on different Glu residues within the α- and ß-tubulin C-terminal domain. In contrast, acetylation of Lys40 is localized at the amino-terminal domain of α-tubulin. (b) Schematic representation of the different PTM reactions and their corresponding enzymes. The figure is taken from Janke and Bulinski (2011).

Nowadays, the precise mechanism of how PTMs of tubulin regulate MT dynamics is not completely understood, but recent studies indicate roles in interacting with motor proteins and MAPs. Detyrosination, Δ2-tubulin generation, and acetylation correlate with stable segments of MTs, such as the initial segment of the axons (Witte et al., 2008). In addition, detyrosination has been showed to regulate several molecular motors and prevent their disassembling from MTs, thus protecting from microtubule destabilization (Kaul et al., 2014). On the other hand, tyrosination preferentially localize in dynamic segments of microtubules, such as growth cones, where it can control the interaction with some plus-end tracking and motor proteins (McKenney et al., 2016).

Polyglutamylation, on the other hand, is suggested to regulate interactions with MAPs, motor proteins, and the activity of the microtubule-severing enzyme spastin (Gadadhar et al., 2017).

1.1.2 Altered microtubule dynamics and neurodegeneration

Several neurodegenerative diseases are characterized by impaired axonal transport, which leads to neuronal damage and death. Although causes of axonal transport deficiencies vary among different neurodegenerative diseases, many of them converge in altered MTs dynamics (Brunden et al., 2017; Dubey et al., 2016). Stable MTs in neurons are well studied to provide tracks for the transport of cargos over long distances. In contrast, the role of dynamic MTs in neurites of mature neurons, despite its suggested role in synaptic plasticity, MT turnover, and axonal regeneration (Bradke et al., 2012; Jaworski et al., 2009), it is not completely well understood. Reduced MT stability has been observed in several neurodegenerative diseases, such as the case of Alzheimer's disease (AD) or related tauopathies, where tau-mediated neurodegeneration is showed to impair axonal transport and signaling by decreased MT stability (Brunden et al., 2017). Similarly, neurons from Parkinson's diseases (PD) patients show a reduction in the neurite length. Moreover, a diminished number of neurite branches and synaptic terminals is observed in PD due to increased MT depolymerization in the absence of Parkin; an E3 ubiquitin ligase reported to bind and stabilize MTs (Ren et al., 2015). On the other side, hyper-stabilization of MTs also results in axonal degeneration; mutations in the MT-severing enzyme spastin are commonly found to impair its function and cause HSP. Dysfunctional spastin induces the accumulation of stable MTs and the reduction of MT dynamics, which in turn causes impaired axonal transport and the subsequent formation of axonal swellings (Fassier et al., 2013). More evidence come from the use of anti-cancer drugs such as taxol, a MT stabilizing molecule used in chemotherapy since it arrests mitosis and induces apoptosis. This drug is reported to have detrimental side effects on the peripheral nervous system by provoking degeneration, reduced axonal transport, axonal length, and axonal fragmentation in animal models (Dubey et al., 2016; Gornstein and Schwarz, 2014). Thus, a proper equilibrium between the stable and the dynamic populations of MTs is crucial for the correct function of neurons. However, although understanding the fine regulation of MT dynamics is pivotal to unravel the etiology of neurodegeneration, the precise mechanism that regulates the equilibrium between dynamic and stable MTs in axons is currently not well understood.

1.2 Intracellular degradation pathways

Practically all cellular functions are performed by proteins, and maintaining a healthy proteome is important to ensure cell function and viability. The process by which cells effectively and efficiently maintain the regulation and modulation of protein biogenesis and turnover is called protein homeostasis (proteostasis). Keeping a healthy proteome also involve the refolding or degradation of damaged or misfolded proteins, since their loss- or gain-of-function can impair cellular functions (Gregersen et al., 2006). The two major degradative pathways involved in protein homeostasis are autophagy and the ubiquitin-proteasome system (UPS). Whereas the UPS degrades small, short-lived misfolded proteins (Ciechanover, 2006), autophagy can selectively degrade larger structures, including protein aggregates and organelles (Rubinsztein, 2006).

1.2.1 The UPS

The UPS mediates the degradation of ubiquitin (Ub)-tagged proteins through the proteasome, a large multicomplex protein that requires ATP to exert its proteolytic activity. During all this process, Ub, a 9 kDa protein, is covalently attached to the N-terminus or internal lysine residues of the targeted proteins. Additionally, the attached Ub can then be the substrate for more ubiquitylation processes through the N-terminus or by its seven lysines (K) (K6, K11, K27, K29, K33, K48, and K63)(Hohfeld and Hoppe, 2018). K48-linked ubiquitin chains are the most abundant chains in mammal cells (Kaiser et al., 2011), and are commonly associated to proteasome degradation, although it has been shown that Ub lysines residues can also trigger proteasomal degradation (Ciechanover and Stanhill, 2014). Alternatively, Ub linkage is also related to proteasome-independent pathways. Such as the case of the monoubiquitylation of plasma membrane receptors, which can induce their endocytosis and subsequent lysosomal degradation (Haglund et al., 2003).

Ubiquitin is conjugated to targeted proteins by a process comprised of three enzymes E1-3: First, ubiquitin C-terminus is attached to the active site cysteine of the E1, also called ubiquitin-activating enzyme, by hydrolyzing ATP. Second, the E1-Ub binds to the E2, or ubiquitin-conjugating enzyme, and catalyzes the transfer of the Ub onto the E2 active site cysteine. Finally, the Ub from the E2-Ub is transferred to a lysine on the target protein by the E3 ligase. Once the targeted protein is fully tagged for proteasome degradation, Ub-tagged proteins are recognized by Ub receptors associated with the proteasome to facilitate their degradation. The proteasome, also referred to as 26S proteasome (number and “S” refers to their Svedberg sedimentation

coefficient) is composed by a barrel-like core complex termed the 20S, involved in the proteolysis of proteins, and two regulatory complexes termed 19S complexes, which cap each site of the 20S (Ciechanover and Stanhill, 2014).

UPS function is found to decrease during aging (Kevei and Hoppe, 2014), which is commonly linked to the formation of aggregate-prone neurotoxic proteins in several neurodegenerative diseases, such as AD, PD and Huntington's disease (HD)(Dantuma and Bott, 2014; Zheng et al., 2016). Indeed, the presence of protein aggregates is associated with the inhibition of the proteasome, such as α-synuclein aggregates (Lewi bodies) (Snyder et al., 2003). Interestingly, UPS is also shown to be involved in the correct turnover of presynaptic proteins in mature neurons, such as RIMI (Yao et al., 2007) and the *D.melanogaster* Bruchpilot (related to the mammalian ELKS) (Zang et al., 2013), and inhibition of the UPS is associated with dysfunctional synaptic activity (Wang et al., 2017).

Several lines of evidence interconnect the UPS and autophagy. Both pathways are reported to share certain substrates, such as α-synuclein (Webb et al., 2003), and have been suggested to be able to coordinate each other and have compensatory mechanisms (Nedelsky et al., 2008; Rubinsztein, 2006). Indeed, application of proteasome inhibitors is known to induce autophagy in cancer models (Wang et al., 2019). Moreover, compensatory autophagy was also found in *D.melanogaster* models of spinobulbar muscular atrophy, a neurodegenerative disease with mutants affecting the proteasome (Pandey et al., 2007). Finally, it is also observed that key autophagy proteins are regulated by proteasomal degradation, such as Beclin-1 (Ashkenazi et al., 2017) and ATG12 (Haller et al., 2014).

1.2.2 Autophagy

Autophagy is a cell self-digestive lysosomal degradation pathway that removes and recycles unwanted cytoplasmic material including damaged organelles and protein aggregates. There are three basic forms of autophagy: microautophagy, chaperone-mediated autophagy, and macroautophagy. Microautophagy is the simpler process, in which cytoplasmic contents are directly invaginated by the lysosomal membrane. The second one, the chaperone-mediated autophagy, degrades selective cytosolic proteins that are brought by chaperones to the lysosome membrane and then translocated inside by protein complexes. The latter one, the macroautophagy, is the best-characterized form of autophagy and involves the sequestration of

cytosolic components by double-membraned vesicles, which subsequently fuse with lysosomes (Galluzzi et al., 2017).

Macroautophagy, commonly and hereinafter referred to as autophagy, can be divided into several distinct stages: autophagosome biogenesis, docking, and fusion with the lysosome, and degradation of the lysosomal content. Autophagosome biogenesis is orchestrated and regulated by AuToPhagy (ATG) related proteins, whose core machineries can be grouped into several functional units, such as the ULK1 kinase complex for the induction of autophagy (ULK, ATG13, ATG101 and RB1CC1/FIP200; the ATG9 for delivery of other ATG proteins and recycling of membrane; the class III phosphatidylinositol 3-kinase (PI3K) complex (VPS34-Beclin1-VPS15) for vesicle nucleation; and the ATG12-ATG5-ATG16L conjugation system for the MT-associated protein 1 light chain 3 (MAP1LC3; best known as LC3) lipidation to phosphatidylethanolamine (LC3-PE or LC3-II), which allows for membrane expansion and enclosure of the autophagosome (See figure 3) (Ariosa and Klionsky, 2016; Hu et al., 2015). Once the autophagosome is formed, it matures by fusing with late endosomes and/or lysosomes to form autolysosomes, which provide an acidic environment and digestive function to the interior of the autophagosome. Lysosomal degradation is mediated by several dozens of hydrolytic enzymes of all types (proteases, lipases, and nucleases). These hydrolases, most of which have acidic pH optima, are activated when the autolysosomal lumen becomes acidified to pH ~ 4.5-5 by the V-ATPase, a large protein complex on the lysosomal membrane that imports hydrogen ions (Saftig and Klumperman, 2009).

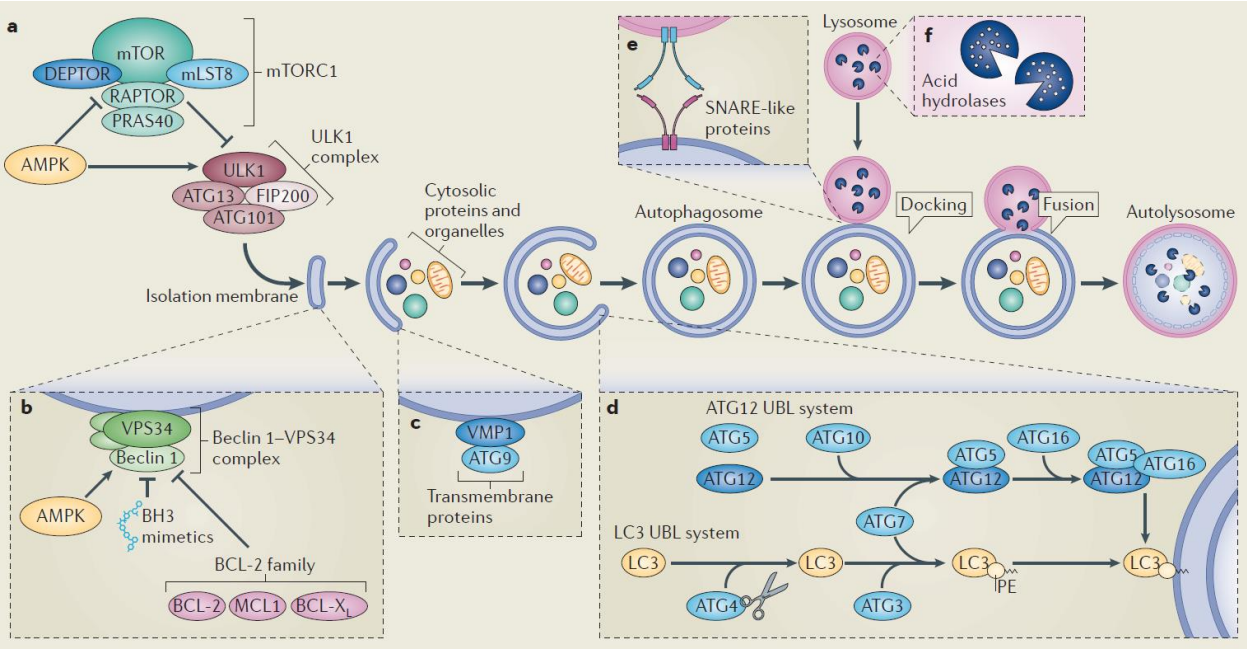

Figure 3. Schematic illustration of autophagosome formation and maturation. (**a**) Autophagy induction requires the inhibition of mTOR complex and the further activation of the ULK1 complex. (**b**) PI3K complex allows the production of PI3P by VPS34, which is tightly regulated by Beclin 1. (**c**) The transmembrane protein ATG9 plays a role in the delivery of proteins and lipids to the phagophore and the recycling between the Golgi, endosomes, and autophagosomes. (**d**) The LC3 and the ATG12 ubiquitin-like (UBL) protein conjugation systems allow the conjugation of LC3 to phosphatidylethanolamine. (**e**) several SNARE-like proteins mediate the fusion between autophagosomes and lysosomes. (**f**) Autolysosomes digest their cargo using hydrolytic enzymes. The figure is taken from Marino et al. (2014).

1.2.2.1 Autophagy induction

A well-known upstream regulation of the autophagy activity includes the mammalian target of rapamycin (mTOR) pathway, which negatively regulates autophagy. mTOR is a serine/threonine kinase which also mediates vital cellular functions such as protein translation and cellular growth. This pathway involves two distinct functional complexes, mTORC1 and mTORC2. mTORC2 includes the rapamycin-insensitive companion of mTOR (Rictor), and it is believed to partly inhibit autophagy through the Akt pathway (Guertin et al., 2006), although more research is needed to better understand the mTORC2. On the other hand, mTORC1, the better-characterized complex, includes the rapamycin-associated protein of mTOR (Raptor), which is known to sense different stimuli and directly inhibit autophagy (Jung et al., 2009). mTORC1 complex prevents autophagy induction through direct interaction with the ULK kinase complex, the main player for autophagy initiation. Thus, mTORC1 directly binds to ULK1/2 and promote a phosphorylation-dependent inactivation of ATG13 and ULK1/2 kinases. Growth factors and amino acids are the best-characterized extracellular stimuli that activate the mTOR pathway. In contrast, starvation, oxygen/hypoxia, and other stressors are found to inhibit mTOR and activate autophagy. Another upstream pathway which regulates autophagy is through the AMP-activated protein kinase (AMPK), an energy-sensing kinase which senses reduced ATP levels and promotes autophagy by inducing ULK1 activation and inactivation of mTORC1 (Sarkar, 2013). Once mTORC1 is inhibited, mTORC1 dissociates from the ULK kinase complex resulting in the dephosphorylation of ULK1/2 and its activation, which in turns phosphorylates and activates ATG13 and FIP200 for the full activation of the ULK complex (Ariosa and Klionsky, 2016). Activation of the ULK complex is believed to directly bind to membranes through ULK1 and ATG13, and thus determine the nucleation site for autophagosomes formation. Although several membranous structures are suggested to generate the nucleation site (endoplasmic reticulum (ER), the Golgi, endosomes, mitochondria, the plasma membrane), ER-mitochondria contact sides are pointed as the most

probable membranous structures (Hamasaki et al., 2013; Maday and Holzbaur, 2014; Mercer et al., 2018). However, more research is required to better understand the mechanism for determination of the nucleation site.

1.2.2.2 Membrane nucleation

Once the nucleation site is specified, ULK complex recruits its immediate downstream effector, the PI3K. The PI3K complex includes the lipid kinase vacuolar protein sorting 34 (VPS34, also called PIK3C3), 15 (VPS15/PIK3R4), Beclin-1 (BECN1), and ATG14. This complex allows VPS34 to generate phosphatidylinositol 3-phosphate (PI3P) and generate the first membranous compartment, the omegasome. This PI3P-enriched site recruits tryptophan-aspartic acid (WD) repeat domain phosphoinositide-interacting proteins (WIPIs) to the omegasome. In turn, other crucial downstream autophagic proteins are recruited, such as the case of ATG16L1, which interacts with WIPI2 (Menzies et al., 2017). The PI3K complex is found to be tightly regulated by Beclin-1, whose role as an adaptor protein allows the association of the different members of the complex, and can suppress or activate autophagosome formation upon interaction with several proteins, such as the apoptosis regulator BCL-2 and AMPK (Galluzzi et al., 2017).

1.2.2.3 Phagophore expansion and enclosure

The membranous expansion of the omegasome forms the phagophore: a double-membraned cup-shaped structure, whose elongation and enclosure leads to the autophagosome generation (Rubinsztein et al., 2012). The source of the membrane which allows phagophore expansion is still under debate, but several candidates are suggested to participate, including the ER, the Golgi apparatus, endosomes, mitochondria, and the plasma membrane (Ktistakis and Tooze, 2016). For example, the Golgi apparatus contributes to membrane nucleation and phagophore expansion by providing the ATG9-positive vesicles, and its defective sorting leads to reduced autophagosome generation and axonal degeneration (Ivankovic et al., 2019). Indeed, recent evidence suggests that ATG9 also traffics through the endosomal system, interplaying a role in sorting and recycling between the Golgi, endosomes, and autophagosomes (Yu et al., 2018).

The conjugation/lipidation of Atg8 homologs (LC3/GABARAPs) to phosphatidylethanolamine (PE) of the up-growing phagophore is another key process for efficient autophagy. Yeast possesses only one *atg8* gene, whereas mammals contain several homologs (LC3A, LC3B, LC3C,

GABARAP, GABARAPL1/GEC1 (Glandular epithelial cell protein 1) and GABARAPL2/GATE-16 (Golgi-associated ATPase enhancer of 16 kDa). Knockout (KO) for proteins involved in the conjugation of LC3/GABARAPs, such as ATG7 (Komatsu et al., 2006) or ATG5 (Hara et al., 2006), have been largely used as models for impaired autophagy (Mizushima and Levine, 2010). Both ATG7 and ATG5 work in two different ubiquitin-like conjugation systems for the lipidation of LC3/GABARAPs. One conjugating system requires the cleavage of the C-terminus part of LC3/GABARAP by the cysteine protease ATG4, which leads to the exposure of a glycine residue (LC3I). Cleaved protein is then processed by ATG7 and ATG3 (E1 activating-like and E2 conjugating-like ubiquitin systems, respectively). On the other hand, ATG12 irreversibly associates with ATG5 by the E1 activating-like enzyme ATG7 and the conjugating-like enzyme ATG10. ATG16L1 can then conjugate to ATG5-ATG12 and form a complex that serves as a E3 ligase-like enzyme which facilitates the lipidation of the processed LC3/GABARAP to PE (LC3II) (Ariosa and Klionsky, 2016; Menzies et al., 2017). Genetic ablation of the LC3/GABARAP lipidation machinery results in the accumulation of unsealed autophagosomes (Sou et al., 2008). In contrast, LC3/GABARAPs are found to be not essential for the enclosure of autophagosomes, suggesting that the conjugating machinery system may have additional functions (Nguyen et al., 2016). The process of phagophore sealing is then poorly understood, but some evidence shows that ATG2 and WIPI1 regulate this process (Menzies et al., 2017).

LC3s and GABARAPs are thought to share common functions during autophagy, since single KOs of the different Atg8 homologs show neither alterations in autophagy function nor cell viability, suggesting the redundant functions of these homologs (Kuma et al., 2017). Despite that, some evidence indicates that LC3s act at earlier stages of autophagosome formation, whereas GABARAPs function downstream in autophagosomes maturation and lysosome fusion (Ktistakis and Tooze, 2016; Nguyen et al., 2016). Indeed, further studies need to be conducted to clarify the distinct roles of LC3/GABARAP. Among all Atg8 homologs, LC3B is the most studied and it is used as a marker for autophagy. LC3B (as well as the rest of LC3s and GABARAPs) is found to be lipidated to both the inner and the outer membrane of pahgophores and autophagosomes. Moreover, while the inner LC3II is degraded by lysosomal enzymes, the outer LC3-II is cleaved and released by the ATG4. Thus, monitoring the ratio of LC3I and LC3II isoforms is a widely used tool to study autophagosome formation and processing (Mizushima and Komatsu, 2011).

Originally, it was believed that autophagy was a non-selective bulk degradation process, which engulfs and degrades any portion of the cytoplasm. Nowadays, it is accepted that autophagy can also behave as a selective process, which requires of autophagic receptors and adaptors to

specifically target cargos for degradation, a process termed selective autophagy. Actually, selective autophagy has raised as a more crucial process in most of the mammalian diseases than “bulk autophagy”, which it is thought to primarily act as a homeostatic mechanism during starvation (Kaur and Debnath, 2015; Levine and Kroemer, 2019). Depending on the target cargo, several selective autophagy pathways have been identified: mitophagy (mitochondria), aggrephagy (proteins aggregates), xenophagy (pathogens), ER-phagy or reticulophagy (ER), ribophagy (ribosomes), pexophagy (peroxisomes), nucleophagy (proteins of the nucleus), lipophagy (neutral lipid droplets), proteaphagy (proteasomes), lisophagy (damage lysosomes) (Galluzzi et al., 2017). As mentioned above, selective autophagy is driven by autophagy receptors, which bridge cargos to the forming phagophore via their interaction with LC3/GABARAP through LC3-interacting regions (LIR). As a consequence of their bridging function, autophagy receptors become degraded within the lysosomes, which make them suitable for monitoring functional autophagy (e.g., p62/sequestosome 1 (SQSTM1)) (Galluzzi et al., 2017; Kuma et al., 2017). Moreover, based on how autophagy receptors recognize and interact with targeted cargos, selective autophagy can be divided into ubiquitin (Ub)- dependent and independent pathways (Khaminets et al., 2016). In the Ub-dependent pathway, ubiquitinated cargo is recognized by autophagy receptors via Ub binding domains (UBD). The K63 type of Ub linkage appears to be often reported to induce autophagy degradation (Ito et al., 2013; Tan et al., 2008). However, later reports suggest that mostly substrate aggregation and receptor oligomerization, and not the type of Ub linkage, is responsible for the target to autophagy clearance (Hohfeld and Hoppe, 2018). Indeed, ATG5 and ATG7 KO autophagy-deficient mice are found to accumulate Ub chains of different topology (Riley et al., 2010). Interestingly, and similarly to the proteasome system, autophagy uses different autophagy receptors to recognize different ubiquitinated cargos. For example, protein aggregates are recognized by p62, NBR1 (next to BRCA1 gene 1 protein) and OPTN (optineurin); mitochondria are recognized by OPTN, NDP52 (nuclear domain 10 protein, also called CALCOCO2); peroxisomes are recognized by (NBR1); bacteria are recognized by p62, OPTN, NDP52; and proteasomes are recognized by RPN10 (Khaminets et al., 2016). On the other hand, Ub-independent autophagy is characterized by the utilization of autophagy receptors that recognize different types of signals of different nature (proteins, lipids, or sugars). Many of these receptors are yet undiscovered, but an example is the FAM134B (family with sequence similarity 134 member B), also termed as reticulophagy regulator1 (RETREG1), which mediate ER-phagy via LIR and reticulon domains (ER binding) (Khaminets et al., 2016).

1.2.2.4 Autophagosome-lysosome fusion

Once the phagophopre is enclosed, autophagosomes are transported along the MTs to the perinuclear region of the cell, where lysosomes are generally located in most of the cell types. Dynein-dependent retrograde transport is essential to accomplish autolysosomes formation, but kinesins and actin-based motors are also shown to participate in autophagosomes-lysosome tethering and fusion (Ktistakis and Tooze, 2016). Prior to autophagosomes-lysosome fusion, both membranous organelles are tethered each other by several complexes, including the homotypic fusion and protein sorting (HOPS) complex, and the ras-related protein Rab-7 (RAB7). HOPS is composed of several vacuole sorting proteins (VPS), which interact with the Q-SNARE Syntaxin 17 (STX17) located on autophagosomes. At the same time, RAB7, together with other proteins, simultaneously binds to the HOPS complex on one side, and to membranes and membrane-anchored proteins on the other side. Thus, assembly of the HOPS-RAB7 complex can bridge opposing membranes and facilitates their close proximity. Finally, STX17 is able to interact with synaptosomal-associated protein 29 (SNAP29) and the lysosomal R-SNARE vesicle-associated membrane protein 8 (VAMP8) to form the trans-SNARE complex, which provides the force required for autophagosome-lysosome fusion. The specificity of vesicle fusion is not only provided by the core tethering and SNAREs complexes, but also additional adaptor proteins ensure it. For example, LC3/GABARAPs and ATG12-ATG5 are able to interact with the RAB7-HOPS and the SNARE complexes (Ktistakis and Tooze, 2016).

Lysosomal fusion let the release of lysosomal hydrolases into autophagosomes, which degrade the inner membrane of the autophagosomes and any other macromolecule, including DNA, RNA, proteins, lipids, and carbohydrates. Metabolites generated in these proteolytic processes, such as amino acids, are actively pumped out into the cytosol to be reutilized (Ariosa and Klionsky, 2016). Lysosomal hydrolases have acidic pH optima around 4.5-5. This pH gradient is generated and maintained by the activity of a proton-pumping V-type ATPase, which hydrolyzes ATP to pump protons into the lysosomal lumen (Ferguson, 2019). Inhibitors of lysosomal acidification and autophagosome-lysosome fusion are commonly used for monitoring the turnover of LC3 and p62, a read-out of autophagy flux. Bafilomycin A1 (BafA1 or Baf) and chloroquine (CQ) are the more common drugs used for this propose. BafA1 have been shown to act at two different steps: inhibiting the proton-pumping V-type ATPase, and also by disrupting autophagosome-lysosome fusion via inhibiting Ca-P60A/SERCA (Ktistakis and Tooze, 2016). CQ impairs autophagosomes-lysosome fusion rather than affecting the acidity of the organelle (Mauthe et al., 2018).

1.2.2.5 Genetic mouse models of autophagy

The generation of autophagy-deficient mice lacking specific ATG proteins has been extensively used to understand the physiological roles of autophagy in mammals. Phenotypes produced by null deletion of core *Atg* genes can be classified by the stage of death: (1) Embryonal death is found in knockouts (KO) of genes that function upstream of the ATG conjugation system (except ULK1/2 double KO, which die after birth). Interestingly, depending on the targeted gene, death appears at different stages of embryonic development and show tissue heterogeneity abnormalities. A possible explanation for such differences may come from the multifunctionality of these proteins, which can participate in non-autophagic functions (Kuma et al., 2017). (2) Postnatal death within 1 day after birth is common for KO of genes involved in the ATG conjugation system. Death results of malnutrition due to lack of self-derived nutrients and suckling failure (Kuma et al., 2017). Interestingly, it has been demonstrated that suckling failure is due to neuronal dysfunction in ATG5-null mice, and neuronal-specific re-expression of ATG5 can rescue these mice from premature death (Yoshii et al., 2017). Thus, the ATG conjugation system appears to be essential for neuronal function. On the other hand, it is reported that autophagosomes can also form in the absence of the ATG conjugation system at a much-reduced rate (Tsuboyama et al., 2016), which in turn may explain the milder phenotype observed in ATG conjugating system-deficient mice compared with the ones working upstream (Kuma et al., 2017). (3) Absence of mortality and no obvious or weak phenotypes are characteristic for mouse models where the KO gene possesses a homolog that is functionally redundant (i.e., ULK single KO, ATG4, and LC3/GABARAP).

1.2.2.6 Role of MT dynamics in autophagy

Autophagosomes rely on the MT-based transport to move within the cell and fuse with lysosomes. Despite no much is known about how MTs and autophagosomes regulate themselves to ensure efficient transport, cumulative evidence highlights the importance of a proper relation between both structures. Indeed, it is suggested that starvation-induced autophagosome formation requires labile MTs for the recruitment of autophagosome precursors and motor proteins (Geeraert et al., 2010). In contrast, mature autophagosomes may require stable MTs for efficiently move and fuse to lysosomes (Kast and Dominguez, 2017). In agreement with this concept, low treatment of nocodazole, a MT-depolymerizing drug, was found to only depolymerize the labile MT subset and subsequently block the formation of new autophagosomes in HeLa cells (Geeraert

et al., 2010). In neurons, it is known that autophagosomes form in distal parts of axons, where the subset of labile MTs is higher (Kapitein and Hoogenraad, 2015). In this labile region, autophagosomes are shown to have an initial bidirectional movement, which later is switched to a robust dynein-dependent retrograde transport in the middle and initial segments of the axon (Maday et al., 2012). Interestingly, axonal initial and middle segments are enriched in stable MTs (Kapitein and Hoogenraad, 2015). Thus, it is suggested that MT dynamics may affect the recruitment of motor proteins for the trafficking along MTs, although little is known yet (Tas and Kapitein, 2018).

1.2.2.7 Role of autophagy in neurons

The majority of our neurons accompany us for most of our lifetime, and due to their post-mitotic nature, neurons cannot dilute detrimental proteins and organelles by cell division, in contrast to other cell types. This fact, combined with extremely polarized neuronal morphology, has made neurons to develop efficient and tight mechanisms to control protein degradation. Indeed, neuronal autophagy is highly compartmentalized. Most of the mature and fully functional lysosomes accumulate within and near the soma (Kulkarni and Maday, 2018). Therefore, newly formed autophagosomes coming from distal regions of the axon are retrogradely transported along microtubules towards the soma, where autophagosomes mature along the way (Maday et al., 2012). Once these organelles enter the soma, autophagosomes are confined into the somatodendritic region and are impeded from returning to the axon (Maday and Holzbaur, 2016). This compartmentalization may, in turn, ensure efficient recycling of the lysosomal products in the primary site of macromolecule biogenesis, the soma (Kulkarni et al., 2018). Whether axonal autophagy performs only selective degradation or also “bulk degradation” of axonal content remains unclear. However, it was shown that most of autophagosomes are positive for ubiquitin (Maday et al., 2012). The soma of the neuron is also able to generate autophagosomes, but the biogenesis in dendrites is more limited in basal conditions. Despite that, autophagosome density in dendrites is increased upon enhanced synaptic activity, mostly due to local biogenesis in dendrites or by the recruitment from the soma, where autophagosomes can bidirectionally move, in contrast with axons (Kulkarni et al., 2018).

Alternatively, emerging evidence suggests the existence of trans-cellular autophagy, a pathway shown by axons of retinal ganglion to throw out mitochondria to adjacent astrocytes for their degradation (Davis et al., 2014). A mechanism further supported by the demonstration that

C.elegans neurons can extrude organelles and protein aggregates in vesicles termed exophers, which are subsequently phagocytosed by surrounding cells (Kulkarni et al., 2018; Melentijevic et al., 2017).

1.2.2.8 Autophagy at the synapse

Synapses are dynamic structures that allow neurons to communicate with each other via the release of neurotransmitters. Action potentials generated in the soma travel along the axon and evoke, at the presynapse, the release of vesicles containing neurotransmitters, which in turn bind to receptors to modulate/trigger the neuronal activity of the postsynaptic neuron (Vijayan and Verstreken, 2017). The release of neurotransmitters not only requires the membrane fusion of synaptic vesicles with the plasma membrane, but also the retrieval of the membrane by endocytosis to form new vesicle pools, receiving then the term of synaptic vesicle cycle (Kononenko and Haucke, 2015; Soykan et al., 2017). To accomplish that, large groups of proteins are involved in proper function and coordination. Indeed, it is estimated that only in the presynaptic region there is an average of 300,000 proteins (Wilhelm et al., 2014). Such a vast amount of proteins in a rather small volume coordinate repeatedly the synaptic vesicle cycle, which in some neurons is performed in high frequencies (Kononenko and Haucke, 2015). These stressful conditions let proteins to be susceptible to damage, which will require of degradative pathways to keep proper protein homeostasis in the synapses.

Cumulative studies point to autophagy as synapse regulator, more specifically in the presynaptic region. Impaired autophagy causes a reduction in the number of neuromuscular junctions in *D. Melanogaster* (Shen and Ganetzky, 2009). ATG9 and the subsequent formation of autophagosomes are required for proper synapse formation in developing axons of *C.elegans*(Stavoe et al., 2016). Moreover, neuronal activity has been proved to up-regulate autophagy in neuromuscular junctions of *Drosophila* and at pre- and postsynaptic sites of rat hippocampal neurons (Vijayan and Verstreken, 2017). Indeed, several synaptic proteins have been recently reported to interact with autophagy proteins. Rab26, a member of the Rab-GTPase superfamily, was found to selectively localize to presynaptic membrane vesicles and recruit components of the pre-autophagosomal machinery (e.g., ATG16L1) (Binotti et al., 2015). Endophilin A (EndoA) and its binding partner Synaptojanin 1 (Synj1), two proteins enriched at the presynapses with a known role in synaptic vesicle endocytosis, were reported to interact with autophagy proteins and modulate autophagy: Phosphorylation of EndoA by the leucine-rich

repeat kinase 2 (LRRK2) kinase selectively activates synaptic autophagy via recruiting ATG3, which in turn promotes its co-localization with the *Drosophila* Atg8 (LC3/GABARAP). On the other hand, mutations in Synj1, a lipid phosphatase of phosphoinositisides, were reported to decrease autophagy flux due to its loss-of-function to detach the *D. melanogaster* Atg18 (WIPI2) (Vijayan and Verstreken, 2017). One recent interesting report showed that Bassoon, a scaffold protein involved in the organization of the presynaptic active zone, was able to directly sequester ATG5, and that the loss of Bassoon triggered synaptic autophagy, suggesting a negative control of autophagy, in contrast with the previous studies mentioned above (Okerlund et al., 2017).

Altogether, it seems that presynaptic-enriched proteins have evolved to interact with the autophagy machinery to regulate autophagy in synapses. Since many presynaptic proteins are shown to be excluded from the soma, and several autophagy-deficient models show specific axonal degeneration, it is suggested that autophagy in the axons and synapses may have different functions, comparing to autophagy occurring in the somatodendritic area (Vijayan and Verstreken, 2017).

1.2.2.9 Autophagy and neurodegeneration

Loss of protein quality control appears to be a common hallmark across organisms during aging and age-related diseases (Labbadia and Morimoto, 2015). In fact, regular autophagy seems to decline with age, with decreased levels of key autophagy proteins in the human brain (Lipinski et al., 2010; Rubinsztein et al., 2011). Neurons may be particularly sensitive to decreased autophagy during aging since most of the late-onset neurodegenerative diseases accumulate damaged organelles and harmful cytoplasmic aggregates, which are substrates for autophagy degradation. Such as the case of Alzheimer's disease (AD), Parkinson's disease (PD), and Huntington's disease (HD), where tau and amyloid ß (Aß), α-synuclein, and huntingtin aggregates, respectively, are shown to be degraded by autophagy. However, whether these aggregates are a result of the loss of protein quality control or a cellular attempt to restore homeostasis remains under strong debate (Hohfeld and Hoppe, 2018; Koyuncu et al., 2017; Menzies et al., 2017; Vijayan and Verstreken, 2017).

The majority of neurodegenerative diseases in patients are not caused by the monogenic inheritance of mutated genes, which reflects the heterogeneity and polygenetic factors involved in these diseases. However, a subset of cases corresponds to familial cases with inherited genetic mutations, which are useful to understand the mechanisms of pathogenesis. Thus, cumulative

studies have revealed that many of these disease-associated genes affect autophagy (Menzies et al., 2017). In some other cases, direct mutations in core autophagy genes have been implicated in the pathogenesis of neurodegenerative diseases. Such as the case of the missense E122D ATG5 mutation, which was identified in two siblings with mental retardation and childhood ataxia, a disease characterized by cerebellar hypoplasia and subsequent lack of coordination. Mutant ATG5 was found to poorly associate with its partner ATG12, resulting in impaired autophagosomes formation and reduced autophagy flux (Kim et al., 2016). Another autophagy gene mutation was found in the gene *WDR45* (which encodes for WIPI4). WIPI proteins are PI3P sensors that facilitate the recruitment of autophagy proteins during phagophore expansion. Mutations in human were causative for static encephalopathy childhood with neurodegeneration in adulthood (SENDA/BPAN), which was characterized by impaired autophagy flux and accumulation of lipidated LC3-positive membranes (Saitsu et al., 2013).

Neurodegeneration was also shown in various *Atg* KO mouse brains. Since conventional KO of ATG proteins is associated with embryonic or neonatal lethality, conditional nervous system-confined *Atg* KO mouse models have been generated to investigate the different roles of autophagy in the brain. Most of these mouse models have been developed under the Nestin-Cre (Nes) promoter, which is active in neuronal precursor cells at embryonal stages (E7.75) (Dahlstrand et al., 1995). In these KO mice, targeted floxed alleles are deleted in both neurons and glia (Menzies et al., 2017). *Atg5*, *Atg7*, *FIP200*, *Ulk1/2*, and *Atg9a* are examples of Nes-KO models found in the literature (Hara et al., 2006; Joo et al., 2016; Komatsu et al., 2006; Liang et al., 2010; Yamaguchi et al., 2018). All models share increased mortality several weeks after birth, progressive neurodegeneration in different brain areas, and growth retardation. With the exception of Ulk1/2 double-KO, all mice models showed accumulation of p62- ubiquitin-positive inclusion bodies, abnormal membranous structures, and impaired motor functions. Axonal pathology was also detected by the formation of axonal swellings in different neuronal types. In addition, the Nes-*Wdr45/WIPI4* KO has also been reported to generate axonal swellings and accumulate p62-positive inclusion bodies within somas and axonal swellings (Zhao et al., 2015). Despite these common features, the nature of pathology varies according to targeted gene; brain regions have different susceptibility for each KO gene; progressive spongiosis (intracellular vacuolations) are detected in *FIP200* and Atg9a KO mice, but not in Atg5, Atg7; Ulk1/2 double-KO had non-autophagy functions in the trafficking of ER-to-Golgi, impairment of which was responsible for neuronal death. Thus, the variability observed among models may suggest unequal patterns of autophagy across brain regions and the existence of non-canonical functions for the autophagy machinery.

1.2.2.10 Axonal degeneration

Axon degeneration is a characteristic event in many neurodegenerative diseases, including stroke, glaucoma, and motor neuropathies (Wang et al., 2012). Prominent axonal pathology precedes the cell body loss in the form of “dying-back”, in which axons from the synaptic regions gradually degenerate toward the cell body. Despite differences in the rate of degeneration, this process mirrors many morphological features of transected nerves, including the formation of axonal swellings, microtubule disassembly, and eventual fragmentation of the axonal cytoskeleton. All these steps are followed by an upregulation of autophagy for local degradation of proteins and organelles such as mitochondria. Indeed, increased autophagic vacuoles have been found in synapses and spheroids during axonal degeneration (Wang et al., 2012; Yang et al., 2013).

The early-onset degenerative event is characterized by a channel-mediated influx of extracellular calcium. Increased levels of calcium activate the serine-threonine protease calpain, which is capable of cleaving axonal neurofilaments and MT-associated components, such as spectrin and tubulin. Other degradative pathways, like autophagy, are also triggered by the calcium influx (Knoferle et al., 2010). However, more studies are needed to understand the mechanism of action in axonal degeneration.

Axonal swellings (also termed as beadings or spheroids) are appeared in the first steps of axonal degeneration and are often associated with jamming of intracellular organelles and the accumulation of autophagosomes. Indeed, several neurodegenerative diseases such as Alzheimer´s, Parkinson´s, and Huntington´s diseases develop axonal swellings preceding axonal degeneration (Yang et al., 2013). This is also evidenced in axons, where organelle trafficking was disrupted by inhibition of lysosomal proteolysis, a phenotype, which leads to accumulation of autophagosomes specifically within axonal swellings, mimicking AD-like axonal dystrophy (Lee et al., 2011). As mentioned above, the deletion of *Atg5*, *Atg7*, *FIP200*, *WIPI4*, or *Atg9a* under Nes-Cre promoter induces the formation of axonal swellings in neurons. However, and despite the above observations, the pathological significance and the mechanism behind beading and swelling formation remain controversial.

1.3 BDNF-TRKB neurotrophic signaling

Neurotrophins are a family of proteins that play critical roles in neuronal development and maintenance of the nervous system, including a multitude of biological roles such as survival, differentiation, cell cycle arrest, neurodegeneration, neuroprotection, apoptosis, and modulation of synaptic plasticity (Park and Poo, 2013; Sasi et al., 2017). These wide ranges of functions are mediated by four different neurotrophins; nerve growth factor (NGF), brain-derived neurotrophic factor (BDNF), neurotrophin 3 (NT-3), and neurotrophin 4 (NT-4), whose mature forms predominantly bind to tyrosine receptor-like kinases (TRK) A, B, or C. NGF binds preferentially to TrkA, BDNF and NT4 bind to TRKB, and NT-3 binds to TRKC, leading to subsequent activation of specific well-characterized signaling pathways that are predominantly neurotrophic. All mature neurotrophins also bind to the p75 neurotrophic receptor ($p75^{NTR}$) with low affinity, whereas immature forms are specific for this receptor. $p75^{NTR}$ acts predominantly to promote neuronal degeneration, growth cone collapse, or to inhibit axonal regeneration (Blum and Konnerth, 2005; Sasi et al., 2017).

Among all neurotrophin proteins, BDNF is the most studied neurotrophic signal due to its potential neuroprotective and restorative treatment for neurodegenerative diseases. Indeed, BDNF is widely expressed in the central nervous system, and its levels are found downregulated in several neurodegenerative diseases (Lu et al., 2013). Accordingly, substantial *invitro* and *in vivo* studies have revealed BDNF pro-survival effects upon several types of insults, such as glucose deprivation (Tong and Perez-Polo, 1998), glutamate excitotoxicity (Lindholm et al., 1993), and in AD models overexpressing amyloid-beta (Arancibia et al., 2008). Interestingly, it is also reported that reduced levels of BDNF levels during mice development worsen epileptic phenotypes and cause neuronal loss (Tandon et al., 1999). In the brain, BDNF is also involved in neuronal morphology and synaptic function. For instance, BDNF loss causes reduced neuronal complexity in cortical neurons (Gorski et al., 2003), and abolish long-term potentiation (LTP) required for memory consolidation (Panja et al., 2014; Sasi et al., 2017).

At the molecular level, BDNF-binding to TRKB commonly promote the homodimerization of receptors and activates its intrinsic kinase activity, which undergoes autophosphorylation and activates three intracellular signaling cascades: (1) the PI3K/AKT pathway; (2) the ERK (extracellular signal-regulated kinase, also termed MAPK) pathway; (3) the phospholipase C-gamma (PLCγ) pathway. Once the TRKB receptor is activated, several scaffolding proteins are recruited; the scaffold SHC protein interacts via the phosphorylated tyrosine 515 at the TRK

receptors and mediates the activation of the PI3K/Akt pathway. Similarly, SHC also mediates the recruitment of the GTPase Ras and the subsequent activation of the ERK pathway. Downstream of ERK and PI3K/AKT, MAP kinase-interacting kinases (MNK), and mTOR-signaling mediate BDNF/TRKB functions for translational control. On the other hand, phosphorylation of the tyrosine 816 at the C-terminus of TRKB (Tyr^{816}) creates the binding site for the PLCγ, which subsequently induces the release of calcium ions from intracellular calcium stores. Calcium release links BDNF signaling with many calcium-dependent proteins, such as CaMKII, a master regulator of synaptic plasticity (Sasi et al., 2017).

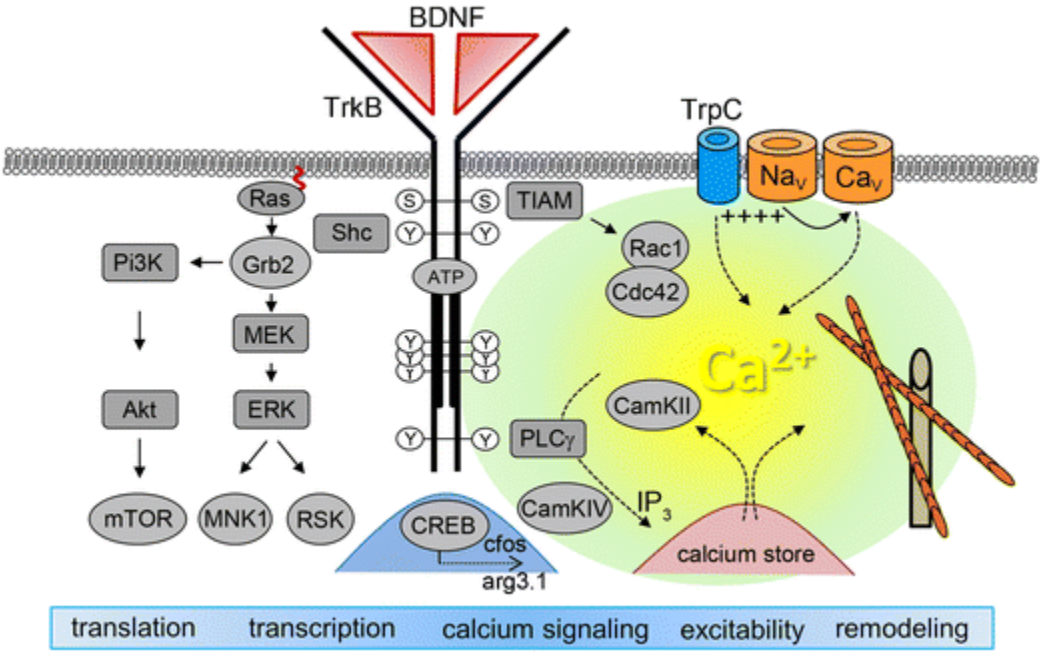

Figure 4. Schematic illustration of the BDNF/TRKB signaling. BDNF binding and subsequent TRKB activation activate three different downstream molecular pathways: the PI3K/AKT, the ERK (MAPK), and the PLCγ. The figure is taken from Sasi et al. (2017).

TRKB receptors are found at both pre- and postsynaptic terminals, thus modulating synaptic plasticity at both sides (Dieni et al., 2012). Once BDNF binds and activates TRKB receptors, TRKB is endocytosed and internalized together with its activated effectors, such as p-ERK, into endosomes, also referred as “signaling endosomes”, since the signaling is sustained in these structures (Watson et al., 2001). Although TRKB-mediated endocytosis was commonly believed to be clathrin-dependent (Ginty and Segal, 2002), later reports have revealed that this internalization mostly occurs via a clathrin-independent mechanism, the EHD4/pincher-

dependent micropinocytosis (Kononenko et al., 2017b; Philippidou et al., 2011). Such endocytic pathway is responsible for the internalization of TrkB-activated receptors into TrkB-multivesicular bodies, which are refractory to lysosomal degradation, thus ensuring persistent signaling (Philippidou et al., 2011). “Signaling endosomes” are retrogradely transported along MTs to the soma, where the sustained signaling induce neurotrophic gene expression (Matusica and Coulson, 2014). Our lab has also recently published that autophagosomes carry TrkB-signaling complexes along the axons into the soma to promote neuronal branching and prevent neurodegeneration, whose neuroprotection effect is blocked in the autophagy-deficient model of ATG5 KO (Kononenko et al., 2017b). Despite this novel process, the precise cellular mechanism underlying defective neurotrophic signaling in autophagy-deficient neurons remains yet unclear.

2. AIMS OF THE STUDY

Most of the studies using autophagy-deficient mice have generated conditional KOs under the brain-specific promoter *Nestin*, which targets for both neurons and glia (Hara et al., 2006; Komatsu et al., 2006; Liang et al., 2010; Yamaguchi et al., 2018; Zhao et al., 2015). Such studies have revealed tissue-specific susceptibility to the lack of autophagy, being the cerebellum the area generally most affected. Cortex and hippocampus were also shown to be severely vulnerable, but at different extent according to the targeted KO gene. Although Purkinje neurons have been directly targeted with specific promoters (Nishiyama et al., 2007), no studies have demonstrated whether the corticohippocampal neuronal degeneration is only due to the lack of autophagy in neurons or in both, neurons and glia.

Loss of core autophagy genes such as *Atg5* or *Atg7* suffer from neurodegeneration, accompanied by axonal pathology and the accumulation of p62- and ubiquitin-positive inclusion bodies (Hara et al., 2006; Komatsu et al., 2006). Given the role of autophagy in regulation of protein homeostasis, these studies suggested that impaired degradation and accumulation of abnormal proteins can disrupt neuronal function and lead to neurodegeneration. However, a following publication showed that the abolishment of inclusion bodies in autophagy-deficient brains did not prevent neurodegeneration, although axonal pathology persisted in neurons (Komatsu et al., 2007). Indeed, later studies from autophagy-deficient mouse brains have also revealed axon-specific susceptibility, which is mainly characterized by the formation of axonal swellings or spheroids, which in turn is a common hallmark displayed in several neurodegenerative diseases (Yang et al., 2013). Thus, axonal dystrophy, and presumed trafficking impairment, are pointed as leading cause of degeneration in autophagy-deficient brains. However, the exact mechanism by which the lack of autophagy leads to axonal pathology and subsequent neuronal loss is poorly understood.

Alternatively, our lab previously reported a non-canonical role of autophagy by which autophagosomes can traffic neurotrophic signals along the axon. Interestingly, ATG5-deficient neurons were shown to suffer from defective neuronal branching (Kononenko et al., 2017), a common feature found in neurodegenerative diseases (Baloyannis, 2009; Gonatas, 1967). However, the exact molecular and cellular mechanism leading to reduced neuronal arborization in autophagy-deficient neurons requires further investigation.

Taken together, this work intended to:

1. Investigate the lack of autophagy in corticohippocampal-specific neurons.
2. Decipher the exact molecular mechanism leading to axonopathy and subsequent neuronal loss in autophagy-deficient neurons.
3. Further demonstrate and characterize the impaired neurotrophic signaling in autophagy-deficient neurons

3. RESULTS

3.1 Forebrain excitatory neurons lacking the LC3 lipidation machinery survive normally but develop severe axonal pathology.

To investigate the lack of autophagy in forebrain excitatory neurons, the commonly used *Atg5*$^{flox/flox}$ mouse line (Hara et al., 2006; Kononenko et al., 2017b; Nishiyama et al., 2007) was crossbred with the CamKIIα-Cre mice, expressing Cre specifically in forebrain excitatory neurons (Dragatsis and Zeitlin, 2000a). In detail, *Atg5*^{flox}allele contains two *loxP* sequences at the same orientation flanking the exon 3 of the *Atg5* gene. In the presence of the Cre recombinase expressed under the CamKIIα promoter (CamKIIα-Cre), Cre binds to both equally oriented *loxP* sequences and excises the targeted exon. Excision of the exon 3 in the *Atg5* gene was demonstrated to abolish the protein expression levels of ATG5 and impair autophagy (Hara et al., 2006)

3.1.1 Forebrain excitatory neurons lacking ATG5 have impaired autophagy

To analyze the role of autophagy in excitatory neurons, we first examined the levels of ATG5 in cortical lysates extracted from CamKIIα-Cre (*Atg5*$^{flox/flox}$:*CamkIIα*-Cre (ATG5 KO)) mice and compared them to lysates obtained from *Atg5*$^{flox/flox}$(WT) mice. As demonstrated in **Fig.5a,b**, the levels of ATG5 were almost abolished in our conditional ATG5 KO mice. Autophagy flux is typically monitored via LC3A/B lipidation to autophagosomes (conversion of LC3I→LC3II), which indicates successful autophagosome formation and maturation. Due to the small molecular weight and sequence similarity between LC3A and LC3B isoforms (82.5%), most of the available antibodies recognize both isoforms. Thus, LC3 levels have been commonly monitored using antibody recognizing LC3A/B, which hereinafter is referred to as LC3. On the other hand, p62 protein levels are also commonly used as a marker of autophagic flux, since p62 is degraded by autophagy and, thus, reports the autophagosome degradation (Kuma et al., 2017). Decreased LC3II levels (**Fig.5c,d**) and accumulation of p62 protein levels (**Fig.5e,f**) in ATG5 KO cortical brain lysates confirmed autophagy impairment in ATG5 excitatory neurons-confined KO mice. To validate that CamKIIα-dependent Cre recombinase expression is confined to mouse forebrain, CamKIIα-Cre mice were crossbred with the Rosa-tdTomato reporter mouse line. This reporter allele contains a CAG promoter followed by a *loxP*-flanked STOP cassette, which suppresses the expression of a red fluorescent variant of tdTomato. In the presence of the Cre-recombinase, the

STOP cassette is excised, allowing the fluorescence expression (Madisen et al., 2010). *CamkIIα*-Cre/Rosa-tdTomato mice displayed strong fluorescence expression in the cortex and the hippocampus, but not in midbrain areas (**Fig.5g**), in agreement with previously published data (Dragatsis and Zeitlin, 2000a).

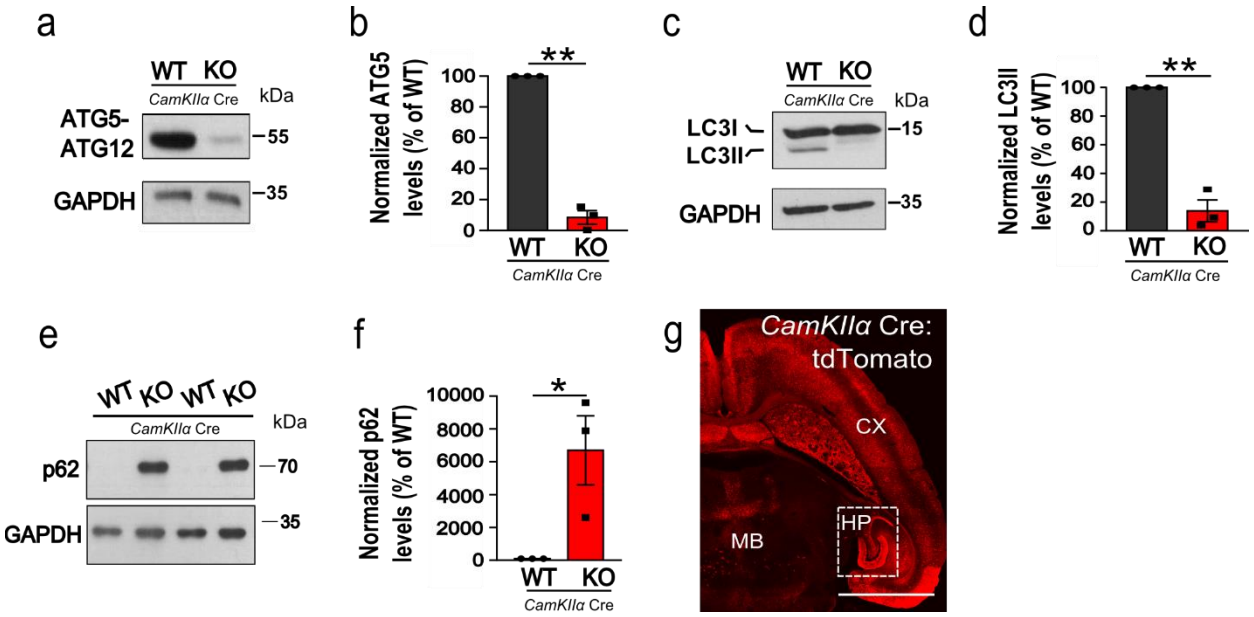

Figure 5: Impaired autophagy in *Atg5*$^{flox/flox}$:*CamkIIα*-Cremice. Western blot of cortical brain lysates from 13 week-old ATG5 KO mice compared to controls. (**a**,**b**) ATG5 expression levels are significantly decreased in ATG5 KO lysates. Protein levels in the KO are normalized to the WT set to 100%. KO: 8.40±4.39, p=0.001, N=3. (**c**,**d**) LC3II expression levels are significantly decreased. Protein levels in the KO are normalized to the WT set to 100%. KO:10.29±4.62%, p=0.001, N=3. (**e**,**f**) p62 expression levels are significantly increased in ATG5 KO lysates. Protein levels in the KO are normalized to the KO set to 100%. KO: 6696.69±2105.47%, p=0.044, N=3. (**g**) Representation of the Cre activity from a horizontal section of the brain of*CamkIIα*-Cre/Rosa-tdTomatomice. CX: cortex, HP: hippocampus (white rectangular area depicts all the hippocampal area), MB: midbrain. All data shown represent the mean ± SEM from N independent experiments.

3.1.2 Mice lacking ATG5 in forebrain excitatory neurons suffer from weight reduction and epileptic seizures which compromises their survival

Nestin-Cre ATG5 KO mice were reported to die several weeks after birth, suffering from weight reduction and ataxia, a loss of voluntary coordination of muscle movements (Hara et al., 2006). In contrast, CamKIIα-Cre ATG5 KO mice were viable and did not display any ataxic disorder, showing both normal walking pattern and non-impaired limb clasping reflexes (data not shown).

However, ATG5 KO mice revealed a cessation of weight gain starting about one month of age when compared to their wild-type littermates (**Fig.6a**), independently of sex (data not shown). Moreover, 64% of ATG5 KO mice started to display epileptic seizures at about 12 weeks (84 days) of age (**Fig.6b**), which subsequently lead to the death of ATG5 KO mice with epilepsy attacks few days or weeks after the of the first seizure (**Fig.6c**). Conversely, seizure-resistant ATG5 KO mice showed no premature death. Taken together, these data suggest a critical role of ATG5 and/or autophagy in CamKIIα-expressing excitatory neurons for the survival of mice.

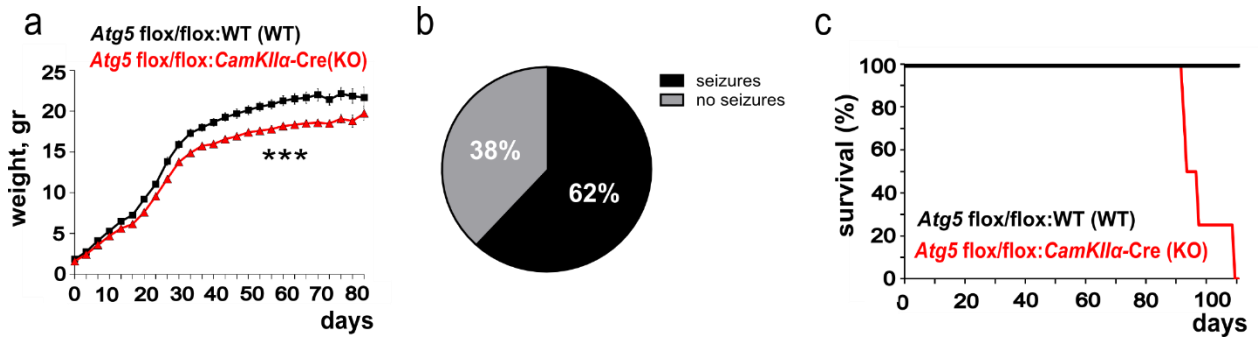

Figure 6: *Atg5*$^{flox/flox}$:*CamKIIα*-Cremice suffer from weight reduction and reveal epileptic seizures. (**a**) Growth curves of WT and ATG5 KO mice. N: WT=28, KO=22 animals. Data analyzed using Two-Way repeated measures ANOVA. (**b**) Percentages of mice displaying epileptic seizures or not in conditional ATG5 KO mice. N: seizures=21, no seizures=8, total=21. (**c**) Kaplan-Meier survival curves of conditional ATG5 KO mice displaying seizures and their littermate controls. N=5.

3.1.3 ATG5 KO or ATG16L1 is dispensable for the survival of CamKIIα-expressing excitatory neurons

Brain-confined autophagy-deficient mouse models have been extensively reported to show neuronal loss and apoptotic cell death across brain areas (Hara et al., 2006; Joo et al., 2016; Marino et al., 2014; Menzies et al., 2017). We, therefore, hypothesized that compromised survival of ATG5 KO mice is caused by apoptosis-induced neuronal loss. First, to examine the neuronal loss, we analyzed Nissl-stained brain sections obtained from perfused 13-week old ATG5 KO mice. Surprisingly, no sign of neuronal loss was neither found in the cortex (**Fig.7a,b**) nor in the hippocampus (**Fig.7c,d**), which both maintained a proper structure and organization. Next, we analyzed the induction of apoptosis by performing the immunostaining of brain sections with an antibody recognizing the cleaved-caspase 3, a reporter of activated apoptosis (Chollat et al., 2019). Although p62 was clearly found accumulated in the cortex, no sign of cleaved-caspase 3

was detected in ATG5 KO brains (**Fig.7e**). In addition, subsequent western blot analysis of cortical lysates from WT and ATG5 KO mice showed no activation of caspase 3 in both conditions (**Fig.10a**).

To reveal whether the mere lack of ATG5 or the impaired autophagy per se was responsible for the phenotype observed in conditional ATG5 KO mice, *Atg16L1*$^{flox/flox}$:*CamkIIα*-Cre (ATG16L1 KO) mouse line was generated. In this mouse line, *Atg16L1*^{flox} allele is flanked by the loxP sequences between the promoter region of *Atg16l1* and the intron 1 (Adolph et al., 2013b). ATG16L1 functions as another critical component of the LC3 lipidation machinery and is crucial for functional autophagy. Similar to ATG5 KO mice, ATG16L1 levels were almost abolished in the KO condition, accompanied by impaired LC3 lipidation and accumulation of p62 (data not shown). Moreover, ATG16L1 KO mice also showed epileptic seizures at around the same time that ATG5 KO mice (data not shown, currently studied by another PhD student in the lab). In agreement with data obtained from ATG5 mice, analysis of Nissl-stained ATG16L1 KO cortical brain areas revealed no sign of neuronal loss (**Fig.7f,g**). Collectively, these data reveal that the lack of ATG5 or ATG16L1, and therefore the LC3 lipidation machinery, are dispensable for the survival of CamKIIα-positive excitatory neurons in cortex and hippocampus.

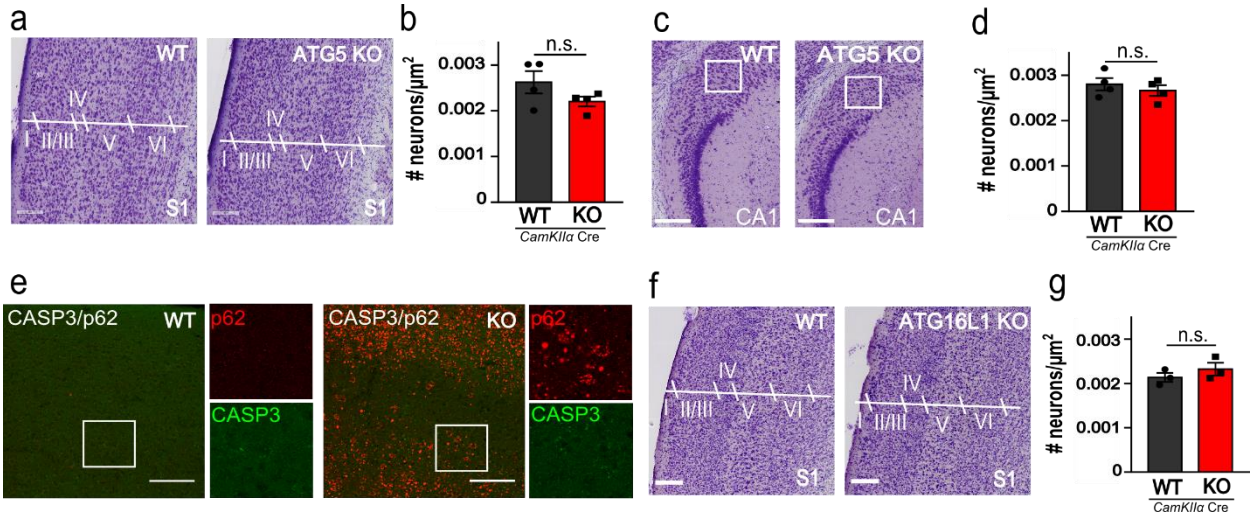

Figure 7. Survival of CamKIIα-expressing excitatory neurons in the mouse brain is dispensable of ATG5 and ATG16L1. Histopathological analysis of Nissl-stained brain sections of ATG5 KO brains at 13-week old reveals no loss of cortical (**a**,**b**) andCA1 (*Cornu Ammonis* area 1)hippocampal neurons (**c**,**d**): Cortex: WT:0.0026±0.0002, KO: 0.0022±0.0001. p=0.163. N=4. Hippocampus: WT:0.0028±0.0003, KO: 0.0026±0.0002, p=0.465, N=4. Scale bars: 200µm (**e**) Representative confocal images of cortical brain sections from WT and ATG5 KO mice immunostained for cleaved-caspase 3 (CASP3, green) and co-immunostained for p62 (red). White rectangular boxes indicate areas magnified to the right. Scale bars:

200µm (**f,g**) Histopathological analysis of Nissl-stained brain sections of WT and ATG16L1 KO cortical brains at 13 weeks old: WT:0.0021±0.0001, KO: 0.0023±0.0001, p=0.354, N=3. Scale bar: 200µm. n.s.-non significant.All data shown represent the mean ± SEM from N independent experiments.

3.1.4 Loss of ATG5 causes axonal neurodegeneration in forebrain excitatory neurons

Despite most of the CamKIIα expression was confined to the cortex and the hippocampus (**Fig.5g**), Nissl-stained brain sections from 13-week old ATG5 KO mice revealed a substantial neuronal loss in the midbrain structure of the thalamus, concretely, in the posterior and ventral nuclei (**Fig.8a**). Interestingly, this area was not targeted by the activity of CamKIIα promoter driving the Cre recombinase expression (**Fig.8b**). Since thalamic atrophy is known to occur in a number of axonal-dystrophy associated diseases (Minagar et al., 2013; Schonecker et al., 2018), and axonal pathology is a common hallmark of autophagy-deficient neurons (Menzies et al., 2017), we hypothesized that structural changes observed in the thalamus of ATG5 KO mice were caused by the degeneration of long-range corticothalamic axons. To investigate that, efferent projections of the motor cortical deep layer neurons targeting the thalamus were labeled by injecting adeno-associated virus expressing GFP under CamKIIα promoter (AAV9-GFP^{CamkIIα}) via stereotaxic surgery (**Fig.8c**). Corticothalamic axons of ATG5 KO neurons revealed signs of axonal degeneration, characterized by *en-passant* axonal swellings (**Fig.8d**). Taken together, we found that although ATG5 is dispensable for the survival of CamKIIα-expressing excitatory neurons in the cortex and the hippocampus, ATG5 KO neurons develop a severe axonal pathology, which may drive the degeneration of other brain areas.

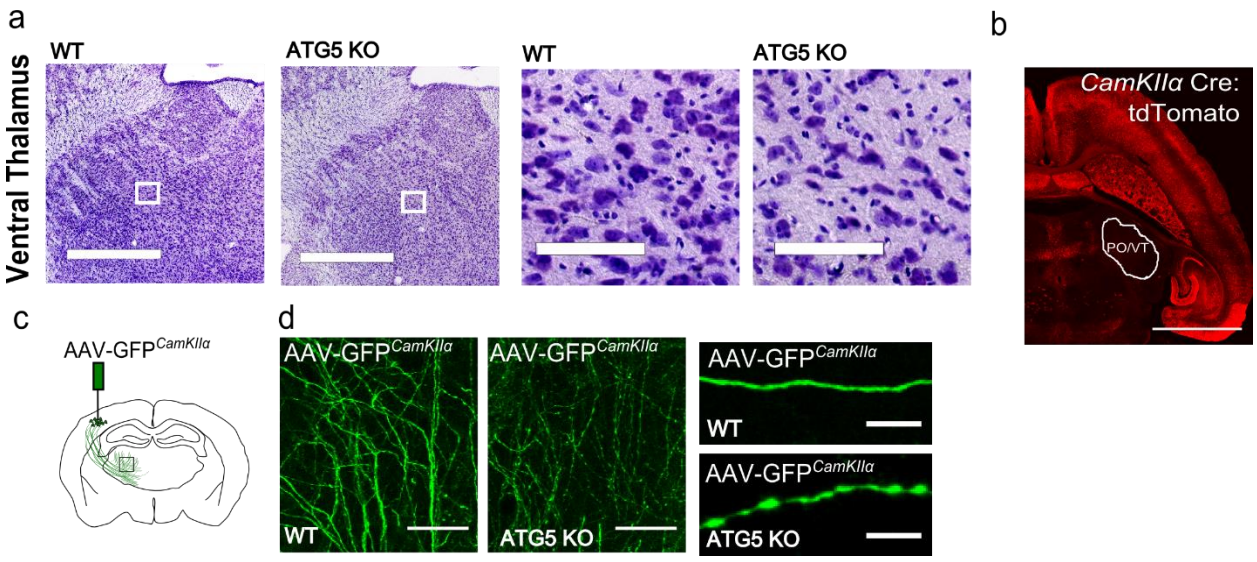

Figure 8. Neurodegeneration of thalamus is associated with axonal pathology of cortical neurons in ATG5 KO mice. (**a**) Histopathological images of Nissl-stained brain sections of ATG5 KO brains at 13-week old reveals neuronal loss in the posterior and ventral nuclei of the thalamus. Scale bar: 900µm. White rectangular boxes indicate areas magnified to the right. Scale bar: 200µm. (**b**) The same image from Fig.5g was modified to select the posterior/ventral nuclei (**c**) Schematic illustration of stereotaxic delivery of AAV9-GFP$^{CamkII\alpha}$ into deep layers of primary motor cortex which connect to midbrain areas. (**d**) Representative horizontal brain sections images of posterior thalamus brain sections from WT and ATG5 KO 13-week old mice after stereotaxic AAV9-GFP$^{CamkII\alpha}$ injection. Confocal images depict GFP-expressing axons. Scale bar: left images: 200µm. Magnified areas in the right: 10µm.

3.2 LC3 lipidation machinery regulates axonal homeostasis

To further investigate the molecular and cellular mechanisms by which the lack of ATG5 or autophagy *per se* drives the axonal pathology, an *in vitro* model for autophagy-deficient primary neuronal cultures was developed. *Atg5*$^{flox/flox}$ or *Atg16L1*$^{flox/flox}$ mice were crossbred with a tamoxifen-inducible CAG-Cre recombinase line (Kononenko et al., 2017) to generate either *Atg5*$^{flox/flox}$:CAG-Cre or *Atg16L1*$^{flox/flox}$:CAG-Cre. CAG is a synthetic promoter which combines the cytomegalovirus immediate-early enhancer, the chicken ß-actin promoter, and the splice acceptor of the rabbit ß-globin gene (Niwa et al., 1991). Tamoxifen-inducible CAG-Cre contains the Cre recombinase fused to a mutant form of the mouse estrogen receptor which does not bind to the natural ligand, but to 4-hydroxytamoxifen (tamoxifen, Tmx). Tamoxifen-inducible CAG-Cre is restricted to the cytoplasm but can be translocated to the nucleus of the cell upon tamoxifen binding (The Jackson Laboratory). Thus, the addition of tamoxifen (KO) or the vehicle solution (WT) at the day in vitro (DIV) 0 defined the genetic background of neuronal cultures. Moreover, neuronal cultures were prepared from cortex and hippocampus brain areas, which are known to have a high expression of excitatory neurons, e.g., 70-80% of the neurons in the cortex are excitatory (Lodato and Arlotta, 2015)

3.2.1 Autophagy is impaired in ATG5 and ATG16L1 KO neurons *in vitro*

First, ATG5 and ATG16 KOs were validated in cortical/hippocampal cultured neurons (hereafter referred to as cultured neurons). We detected almost a complete loss of each protein in KO lysates of cultured neurons at DIV16 (**Fig.9a,d**), the age when cultured neurons are reported to be fully mature (Moutaux et al., 2018). Similar to *in vivo* data, neurons lacking ATG5 and ATG16L1

accumulated p62 and had impaired LC3 lipidation showed by decreased LC3II protein levels (**Fig.9b,c,** and **e,f**). Thus, ATG5- and ATG16L1-deficient neurons have impaired autophagy *in vitro*.

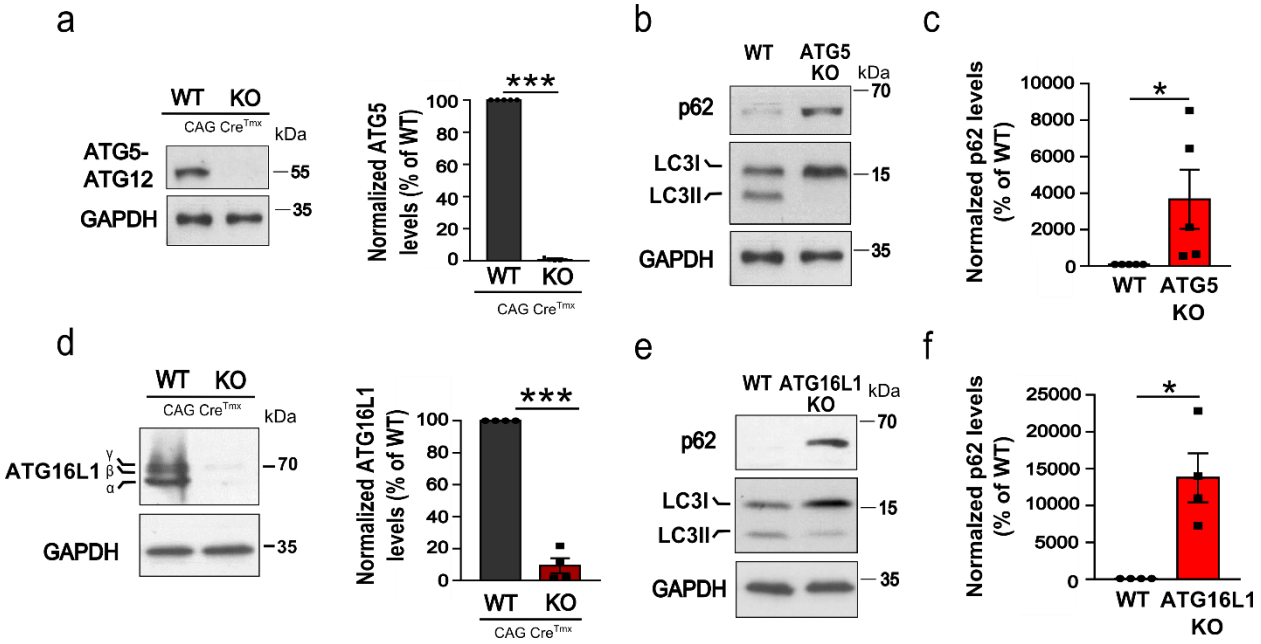

Figure 9. Cultured neurons lacking either ATG5 or ATG16 have defective autophagy in vitro. (**a**) ATG5 expression levels are significantly decreased in ATG5 KO lysates from cultured neurons at DIV16. Protein levels in the KO were normalized to the WT set to 100%. KO: 1±0.00%, p<0.000. N=5. (**b**) p62 and LC3 blots in WT or ATG5 KO lysates at DIV16. (**c**) Analysis of p62 expression from b: KO: 3661.93±1618.82%. Protein levels in KO condition were normalized to the WT set to 100%. p=0.046, N=5. (**d**) ATG16L1 expression levels are significantly decreased in ATG16L1 KO lysates from cultured neurons at DIV 16-18. Protein levels in the KO were normalized to the WT set to 100%. KO: 9.34±4.69%, p<0.000. N=4. (**e**) p62 and LC3 blots in WT or ATG16L1 KO lysates at DIV16-18. (**f**) Analysis of p62 expression from e: KO: 13757.23±3317.55%. Protein levels in KO condition were normalized to the WT set to 100%. p=0.013, N=4. All data shown represent the mean ± SEM from N independent experiments.

3.2.2 ATG5- and ATG16L1-deficient cultured neurons show neither apoptosis nor neuronal death

Since neither neuronal degeneration nor apoptosis was detected in autophagy-deficient CamKIIα-expressing neurons *in vivo* (**Fig.7**), we next used ATG5 KO and the ATG16L1 KO *in vitro* models to investigate whether cultured neurons are resistant to neuronal death upon defective autophagy. First, levels of cleaved caspase 3 were analyzed by Western blotting. Neither ATG5 nor ATG16L1

KO lysates from cultured neurons showed signs of apoptosis, in contrast to hydrogen peroxide-treated cells, a known inducer of apoptosis (**Fig. 10a,b**). Strikingly, cultured ATG16 KO neurons were apoptosis-resistant even under starvation (**Fig.10b**), a known stress condition, which induces autophagy (Young et al., 2009). These data were further supported by the analysis of mRNA levels of apoptotic genes, which revealed no changes between WT and ATG5 KO conditions (**Fig.10c**). Finally, since apoptosis is only one of the multiple molecular mechanisms inducing neuronal death, a live/dead imaging assay was performed to identify neuronal death in autophagy-deficient condition. ATG5 KO neurons were viable and had a similar WT ratio of live (green) and dead (red) cells (**Fig.10d,e**). Collectively, these *in vivo* and *in vitro* data demonstrate that cortical/hippocampal neurons are viable and do not undergo apoptosis upon ATG5- and ATG16L1-deficiency.

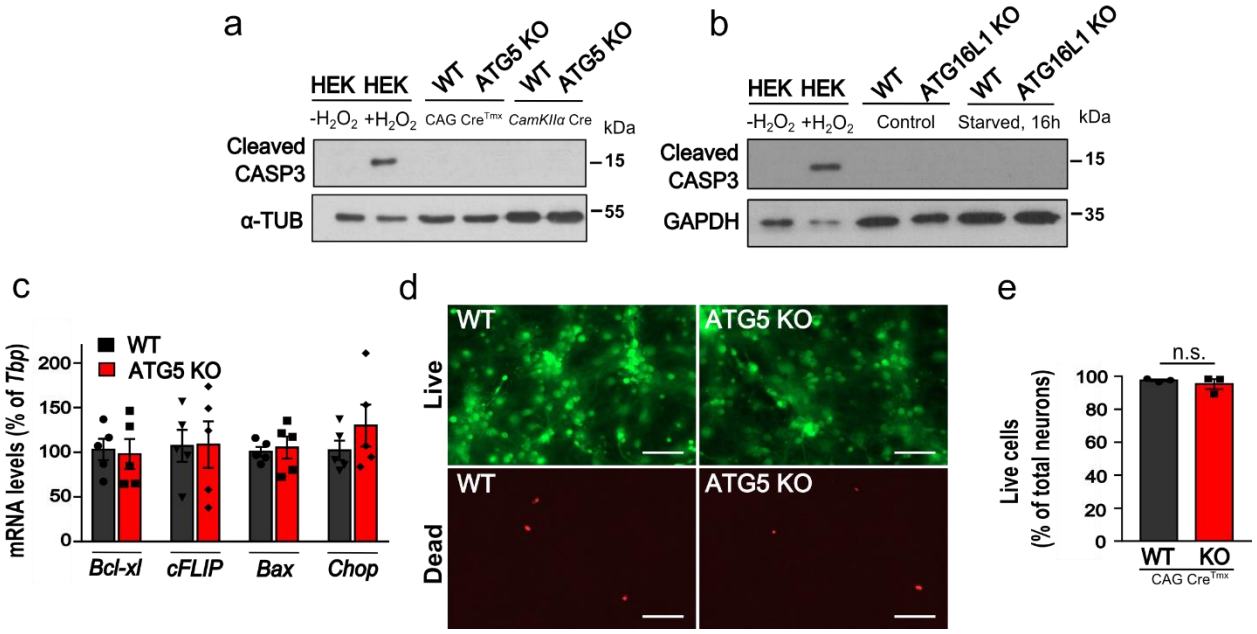

Figure 10. ATG5- and ATG16L1 deficient neurons do not show apoptosis or neuronal death *in vitro*. (**a**) Western blot illustrating cleaved-caspase 3 (CASP3) levels in lysates from cultured WT and ATG5 KO neurons (CAG-Cre), as well as cortical lysates from WT and ATG5 KO mice (CamKIIα-Cre). HEK293T cells treated with H_2O_2 were used as a positive control. (**b**) Western blot depicting cleaved-CASP3 levels from WT and ATG16L1 cultured neuronal lysates without treatment (Control) or starved 16 hours. HEK293T cells treated with H_2O_2 were used as a positive control. (**c**) *Bcl-xl*, *cFLIP*, *Bax,* and *Chop* mRNA levels analyzed by qPCR are not significantly altered in ATG5 KO neurons compared to controls. mRNA levels were normalized to the levels of the housekeeping gene *Tbp* set to 100%. (**d,e**) Representative fluorescence images of WT and ATG5 KO primary neurons after performing Live/Dead cell viability assay. The total number of living (green) and dead (red) neurons were counted and compared with the total number

of neurons as a percentage of alive neurons: WT: 97.55±0.60%, KO: 95.25±3.04%. In total, 6796 WT and 6220 KO cells were counted from N=3. n.s.-non significant. All data shown represent the mean ± SEM from N independent experiments.

3.2.3 Loss of ATG5 or ATG16L1 in primary neurons causes selective axonal degeneration

As described previously, cortical neurons from *Atg5*$^{flox/flox}$:*CamkIIα*-Cre mice showed axonal pathology characterized by the formation of axonal swellings (also termed spheroids). Taken advantage of the *in vitro* model, we performed a detailed morphological analysis of autophagy-deficient neurons transfected with GFP. The presence of spheroids in only MAP2 (dendritic marker)-negative neurites confirmed that axons, but not dendrites, suffer from the axonal pathology upon ATG5-deficiency (**Fig.11a,b**). Interestingly, although 5% of WT neurons developed axonal swellings, about 30% of all ATG5 KO neurons displayed these spheroids (**Fig.11c**). We also found that 58% of axonal swellings were co-localized with the presynaptic marker synaptobrevin 2 (SYB2) (**Fig.11d**). The phenotype was rescued by re-expression of ATG5-eGFP at DIV 7-8 for 7 days (**Fig.11c**). Moreover, spheroids were mostly present in the last segment of the axon, showing a size-range from 2 to 7µm of diameter, of which 2-4µm diameter spheroids were significantly upregulated in ATG5 KO neurons (**Fig.11e**). WT neurons mostly contained 1-1.9µm diameter varicosities, regular size for presynaptic sites, further confirmed by their colocalization with synaptic marker Syb2 (data not shown). Finally, dendritic spine density was not affected by the ATG5 deletion (**Fig.11f,g**). Collectively, these data confirm that ATG5-deficient neurons have increased susceptibility for axonal degeneration, in agreement with *in vivo* data.

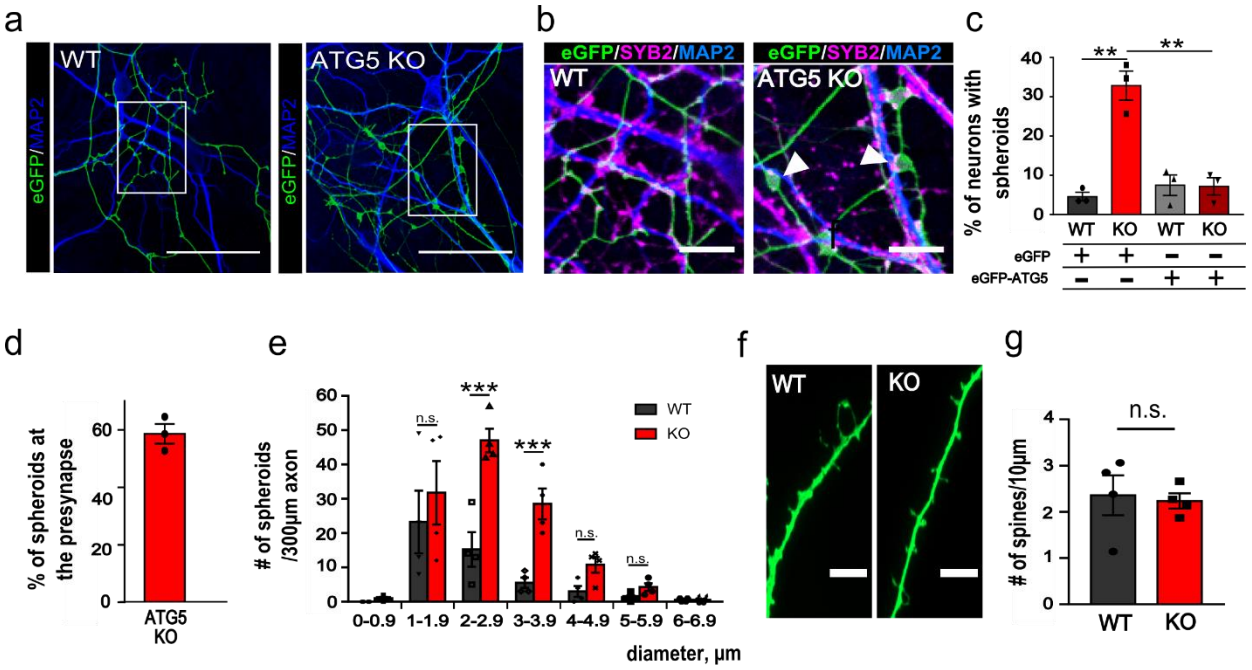

Figure 11. Axons, but not dendrites, degenerate under autophagy-deficient conditions. (**a**) ATG5-deficient primary neurons transfected with eGFP (green) and immunostained for MAP2 (blue) and synaptobrevin 2 (SYB2) (magenta). SYB2 channel was hidden to better distinguish the other two channels. White rectangular boxes depict areas magnified in b. DIV 16.Scale bar: 50µm (**b**) Amplified images showing the SYB2 channel. White arrows indicate axonal swellings positive for SYB2. Scale bar: 50 µm. (**c**) Percentage of WT and ATG5 KO neurons revealing spheroids when transfected with eGFP (WT: 4.60±1.09%, KO: 32.82±3.70%) or with ATG5-eGFP (WT: 7.47±2.60%, KO: 7.18±2.20%). pWT^{GFP} vs KO^{GFP} =0.001, pWT^{ATG5} vs KO^{ATG5} =0.002. In total, 596 WT and 421 KO neurons fromN=3. (**d**) Majority of spheroids are found at synapses (58.62±0.81%). (**e**) Histogram showing the number of axonal swellings in WT and ATG5 KO neurons plotted as a function of their diameter. Statistical significance was tested via two-way ANOVA repeated measures.***pWT vs KO<0.0001. N=4, in total 40 WT and 40 KO neurons.(**f**,**g**) Unaltered spine density in ATG5 KO neurons compared to controls (WT: 2.36±0.36, KO: 2.24±0.14). N=4. Scale bar, 5µm.n.s.-non significant. All data shown represent the mean ± SEM from N independent experiments.

3.2.4 Loss of core autophagy machinery involved in the LC3 lipid conjugation and processing cause axonal degeneration

To further investigate whether the lack of ATG5 or autophagy per se was responsible for the formation of axonal pathology, we analyzed axonal pathology in several other models of autophagy deficiency. Similarly to *Atg5*$^{flox/flox}$:CAG-Cre, *Atg16L1*$^{flox/flox}$:CAG-Cre neurons also revealed a significantly increased number of axonal swellings (**Fig.12a,b**). Since ATG5 and

ATG16L1 work in the same pathway and their interaction directly regulates LC3 lipidation (Romanov et al., 2012), we tested whether the overexpression in WT neurons of the inactive C74A form of ATG4B, involved in the LC3 processing outside of the ATG5-ATG12-ATG16L1 complex (see Figure 1 in the introduction), could lead to the formation of axonal spheroids. In line with our previous models, neurons overexpressing ATG4B^{C74A} developed significantly more axonal swellings compared to controls (**Fig.12c,d**). On the other hand, deletion of FIP200 using smart pool of short interfering (si) RNA, a manipulation that prevents autophagy induction, not directly affecting the levels of LC3 (Hara and Mizushima, 2009), was not sufficient to cause the formation of axonal swellings in cultured neurons (**Fig. 12e-g**). Similarly, downregulation of ULK1 expression levels via short hairpin RNA plasmid transfection of WT cultured neurons do not reveal the formation of axonal swellings (ongoing research). Taken together, these data indicate that impaired LC3 conjugation system, but not the global loss of autophagy function, is responsible for axonal pathology in neurons, suggesting a novel function in axonal homeostasis.

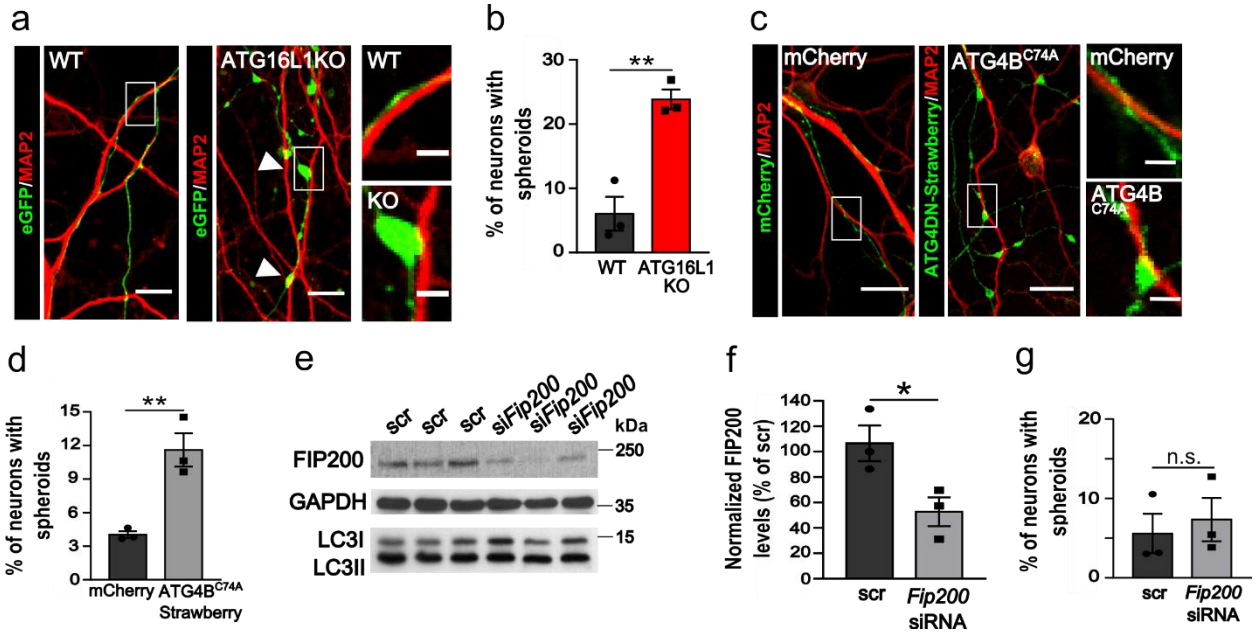

Figure 12. Impaired LC3 lipid conjugation and processing cause axonal degeneration. (**a**) WT and ATG16L1 KO cultured neurons transfected with eGFP (green) and immunostained for MAP2 (red). Scale bar 10μm. White rectangular boxes depict areas magnified to the right. Scale bar: 2μm. (**b**) Percentage of WT and ATG16L1 KO neurons revealing axonal swellings. WT: 6.05±2.14%, KO: 23.85±1.24%. p=0.004, in total 234 WT and 238 KO neurons from N=3. (**c**) Primary control neurons transfected with either mCherry or pmStrawberry-ATG4B^{C74A} (green) and immunostained for MAP2 (red). Scale bars: left panels 10μm, right panels 2μm. (**d**) Percentage of control neurons with axonal swellings transfected either with mCherry (4.03±0.25%) or pmStrawberry-Atg4BC74A (11.60±1.22%). p=0.008. In total, 486 WT and 360 KO

neuronsfrom N=3. (**e**,**f**) Validation of small interfering RNA (siRNA) against *Fip200*.Expression levels of FIP200 in MEF cells transfected either with scramble (scr) (106.70±14.04%) or with *Fip200* siRNA (52.67±11.34%). P=0.042. N=3. Protein levels in KO condition were normalized to the WT set to 100%. (**g**) Axonal swellings are absent in neurons with *Fip200* siRNA-mediated knockdown (KD). Scr:4.46±2.40%, *Fip200* siRNA:5.78±2.87%, p=0.659. In total, 534 control and 820 *Fip200* siRNA neurons from N=4.n.s.-non significant.All data shown represent the mean ± SEM from N independent experiments.

3.2.5 Impaired LC3 lipidation and accumulation of non-lipidated LC3 causes axonal swellings

Previous data suggest that axonal pathology in autophagy-deficient neurons might be caused by defects in LC3 lipidation machinery. Indeed, ATG5 and ATG16L1 KO neurons not only failed to conjugate LC3 (**Fig.9b,e**) but also revealed the accumulation of non-lipidated LC3 form (LC3I) (**Fig. 9b,e,** and **Fig.13a,b**). Thus, we hypothesized that the accumulation of LC3I in the absence of ATG5 and ATG16L1 is responsible for the formation of axonal swellings. To directly test that, control neurons were transfected with a lipidation-deficient construct of LC3B, which contains a single point mutation that substitutes the glycine responsible for lipid conjugation by an alanine residue (G120A) (Kabeya et al., 2000). Overexpression of the RFP-LC3BG120A caused an upregulation of the number of neurons containing spheroids comparing with neurons overexpression the wild-type RFP-LC3B (**Fig. 13c,d**). Moreover, downregulation of LC3B protein levels using siRNA against *Lc3b* (**Fig.13e,f**) diminished axonal pathology in ATG5 KO neurons (**Fig.12g,h**). Interestingly, LC3 was accumulated in axonal swellings of ATG5 KO cultured neurons, which corresponds presumably to LC3I, since lipidation machinery is impaired (**Fig.13g**). Collectively, these data strongly suggest that non-lipidated LC3 accumulates in axonal swellings and promotes axonal pathology.

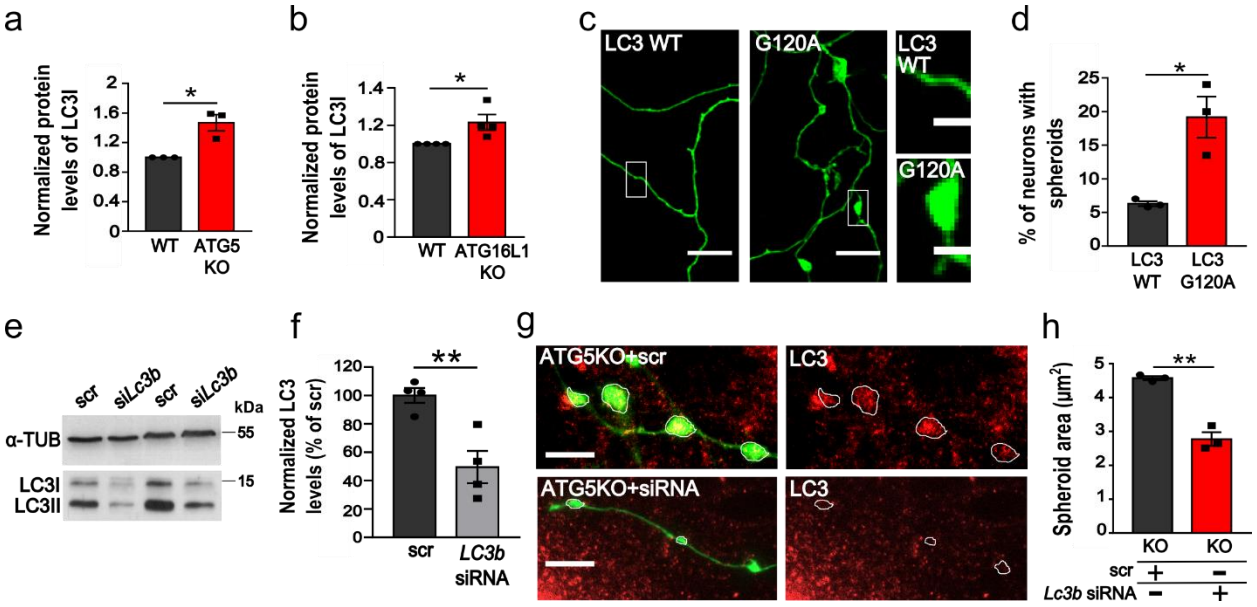

Figure 13. Accumulation of non-lipidated LC3 in axons causes axonal pathology. LC3I protein levels are significantly increased in (**a**) ATG5 KO (1.47±0.11, p=0.025, N=3) and (**b**) ATG16L1 KO (1.23±0.08, p=0.04, N=4) cultured neurons, compared to WT controls set to 1. Representative blot images in Fig.8b (ATG5 KO) and Fig.8d (ATG16L1 KO). (**c**) Representative fluorescent images of control neurons transfected either with full-length ptagRFP- LC3B (proLC3) or ptagRFP-LC3BG120A and co-transfected with eGFP to visualize the axons (green). Scale bars: left panels 10µm, right panels 2µm. (d) Percentage of neurons with axonal swellings expressing either full-length ptagRFP- LC3B (6.29±0.30%) or ptagRFP-LC3BG120A (19.16±2.50%). p=0.014. In total, 332 ptagRFP-LC3B neurons and 251 ptagRFP-LC3BG120A from N=3. (**e**,**f**) Validation of siRNA against *Lc3b*.Expression levels of LC3 in MEF cells transfected either with scr (100±4.5%) or with *Lc3b* siRNA (49.48±9.86%). P=0.007. N=4). (g) Primary ATG5 KO neurons transfected with eGFP (green) to visualize the axons and co-transfected with either scrambled siRNA (scr) or *LC3b* siRNA and immunostained for LC3 (red). White circles indicate *en-passant* axonal swellings. Scale bars: 5µm. (**t**) Loss of LC3B in ATG5 KO neurons significantly decreases axonal spheroid area KO^{scr}: 4.57±0.06µm², $KO^{si\mathit{LC3b}}$2.78±0.20µm², p=0.001. In total, 417 for scr, and 502 for siRNA from N=3. All data shown represent the mean ± SEM from N independent experiments.

3.3 Axonal swellings are not a result of defective protein clearance but accumulate components of MT-based trafficking machinery

Axonal swellings have been reported to accumulate different sorts of proteins and membranous organelles, which in turn is commonly associated with jamming of intracellular organelles (Yang et al., 2013). To further understand the mechanism by which the lack of LC3-lipidation machinery causes axonal pathology, we sought to investigate the precise content of axonal swellings.

3.3.1 Protein inclusion bodies are not accumulated in spheroids from ATG5- and ATG16-deficient neurons

Accumulation of protein aggregates is a common hallmark of defective autophagy. Indeed, accumulation of Ub- and p62-positive inclusion bodies have been largely reported in autophagy-deficient neurons (Hara et al., 2006; Komatsu et al., 2007b; Liang et al., 2010; Zhao et al., 2015). Accordingly, p62 levels were increased in ATG5 and ATG16L1 KO neurons *in vivo* (**Fig. 5e**) and *in vitro* (**Fig.9c,f**). Thus, we investigated whether protein inclusion bodies accumulate within ATG5 and ATG16L1 KO axonal swellings due to their defective clearance. To prove that, ubiquitinated proteins and p62 levels were analyzed by immunocytochemistry in WT and KO cultured neurons. While ATG5 and ATG16 KO soma clearly revealed massive accumulation of p62-positive inclusion bodies (**Fig.14a-c**), axonal compartments and spheroids were devoid of such protein aggregates (**Fig.14d-g**). Similarly, ubiquitin staining showed Ub-positive inclusion bodies in the soma but not in the axon of ATG5 KO neurons (**Fig.14h-j**). These data are in agreement with the previous report that neurodegeneration is independent of protein inclusions in ATG7 KO brains (Komatsu et al., 2007a), and thereby confirms that axonal swellings are not a result of defective protein clearance.

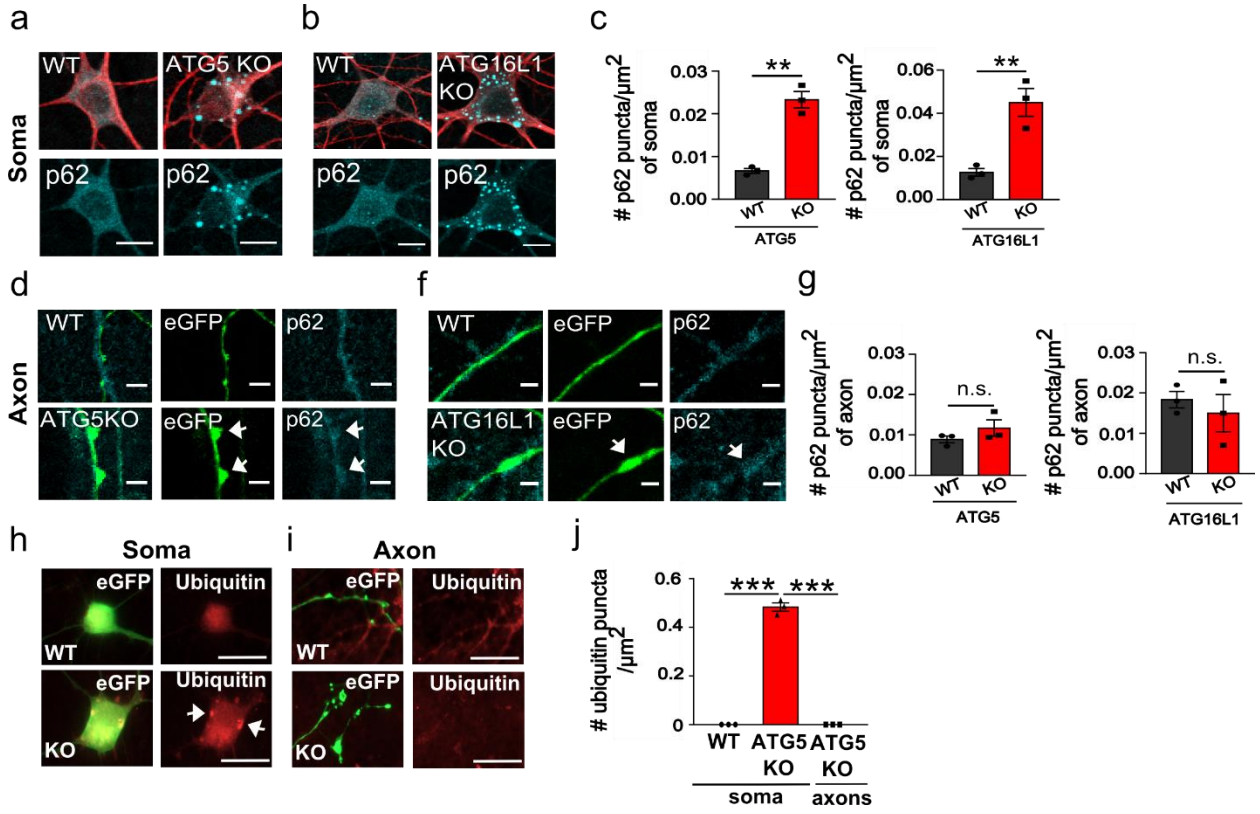

Figure 14. Spheroids do not accumulate Ub- and p62-positive inclusion bodies in neither ATG5 nor ATG16L1 KO neurons. (**a-c**) Representative fluorescence images and analysis of p62-containing puncta in somas of primary ATG5 KO and ATG16L1 KO neurons, immunostained for MAP2. WT: 0.007±0.001, KO^{ATG5}: 0.023±0.002, p=0.001. In total, 27 WT and 33 KO neurons from N=3; WT: 0.013±0.002, $KO^{ATG16L1}$: 0.045±0.007, p=0.009. In total, 31 WT and 28 KO neurons from N=3. Scale bars: 10µm. (**d-g**) Representative fluorescence images and analysis of p62-containing puncta in axons of primary ATG5 KO and ATG16L1 KO neurons. WT: 0.009±0.001, KO^{ATG5}: 0.012±0.002, p=0.131. In total, 29 WT and 30 KO axons from N=3; WT: 0.018±0.002 0, $KO^{ATG16L1}$: 0.015±0.005, p=0.545. In total, 31 WT and 22 KO neurons from N=3. Scale bars: 5µm. (**h-j**) Representative fluorescence images and analysis of ubiquitin-containing puncta in somata and axons of primary ATG5 neurons (WT^{soma}: 0, KO^{soma}: 0.05±0.00, p<0.000; WT^{axon}: 0, KO^{axon}: 0, p KO^{soma} vs KO^{axon}<0.000. In total, 30 WT and 30 KO neurons from N=3. Scale bars: 10 µm. n.s.-non significant.All data shown represent the mean ± SEM from N independent experiments.

3.3.2 Axonal swellings accumulate components of MT-based trafficking machinery

Since axonal swellings were enriched at presynaptic terminals (**Fig.11b,d**), we hypothesized that axonal swellings could be a result from distended synapses in the axon due to either defective synaptic vesicle (SV) exocytosis or impaired trafficking of synaptic membranous compartments. To address the first hypothesis, the levels of SV marker synaptobrevin 2 (SYB2) were analyzed within axonal terminals by immunocytochemistry. We found no alterations in the levels of SYB2

at the presynapses in ATG5 KO neurons compared to controls (**Fig.15a,b**). Next, WT and ATG5 KO cultured neurons were transfected with the pH-sensitive GFP (pHluorin) fused to SYB2 (Kononenko et al., 2013). pHluorins undergo quenching within the acidic SV lumen and are unquenched upon exocytotic fusion, thereby serving as reporters for SV exocytosis (Kononenko and Haucke, 2015). No significant differences were shown by analyzing the SYB2-pHluorin decay fluorescence upon stimulation with 200 action potentials at 50 Hz, further indicating that neurons are capable of normal activity-dependent SV exocytosis (**Fig.15c**).

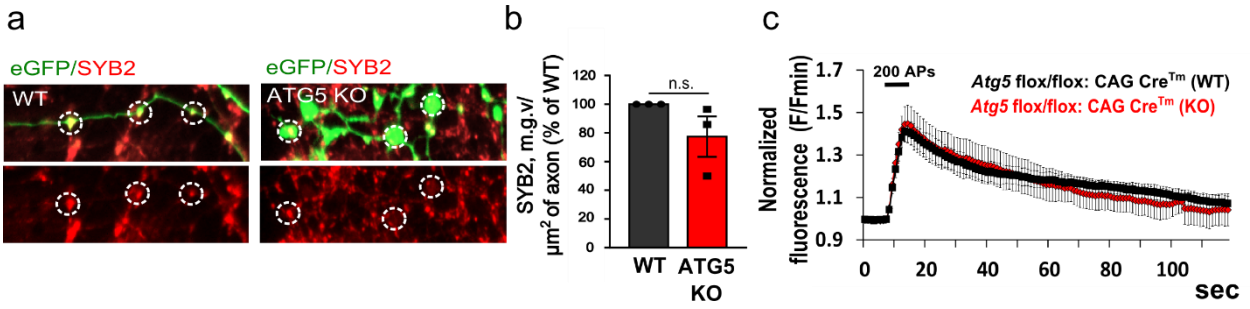

Figure 15. ATG5-deficient neurons neither accumulate SV nor have impaired SV exocytosis. (**a**) Representative confocal images from eGFP transfected WT and ATG5 KO neurons and immunostained for synaptobrevin 2 (SYB2) (red). White circles surround axonal varicosities and spheroids. (**b**) Analysis of the mean grey value of SYB2-containing puncta/area of axonal varicosity or spheroid in axons of WT and ATG5 KO neurons. KO:77.39±14.05%, protein levels in KO condition were normalized to the WT set to 100%. p=0.124, N=3. (**c**) Average SYB2-pHluorin responses to 200 APs at 50 Hz in WT and ATG5 KO neurons (>400 boutons from N=3). Fluorescence transients were normalized to the initial baseline fluorescence before stimulation. n.s.-non significant. All data shown represent the mean ± SEM from N independent experiments.

Previous studies from mouse models and brain biopsies of patients suffering from axonopathies revealed the accumulation of multiple membranous organelles, including late endosomes and mitochondria within axonal spheroids (Wang et al., 2012; Yang et al., 2013). Moreover, several autophagy-deficient mice models evidenced the presence of aberrant membranous structures and accumulation of tubular ER-like structures in soma and axons, respectively (Ivankovic et al., 2019; Nishiyama et al., 2007). Thus, the soma and presynaptic terminals of ATG5 KO neurons were examined by electron microscopy. In line with previously published, aberrant membranous structures, 1-2 µm diameter size, were found in the soma of ATG5 KO neurons compared to WT (**Fig.16a,b**). Presynaptic sites of ATG5 KO neurons were frequently found together with endosome-like structures (**Fig.17a**) and mitochondria (**Fig.17b,c**). Strikingly, ATG5 KO axonal

swellings not only showed an increased presence of late endosomes and mitochondria, but also a massive accumulation of tubular ER-like structures (**Fig.17d**)

a

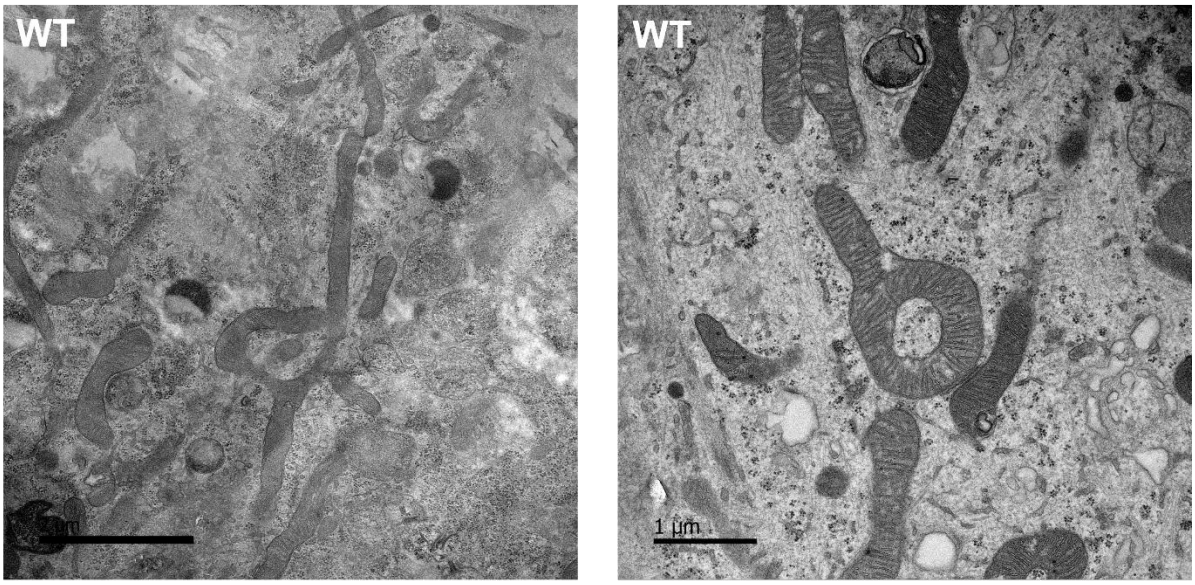

b

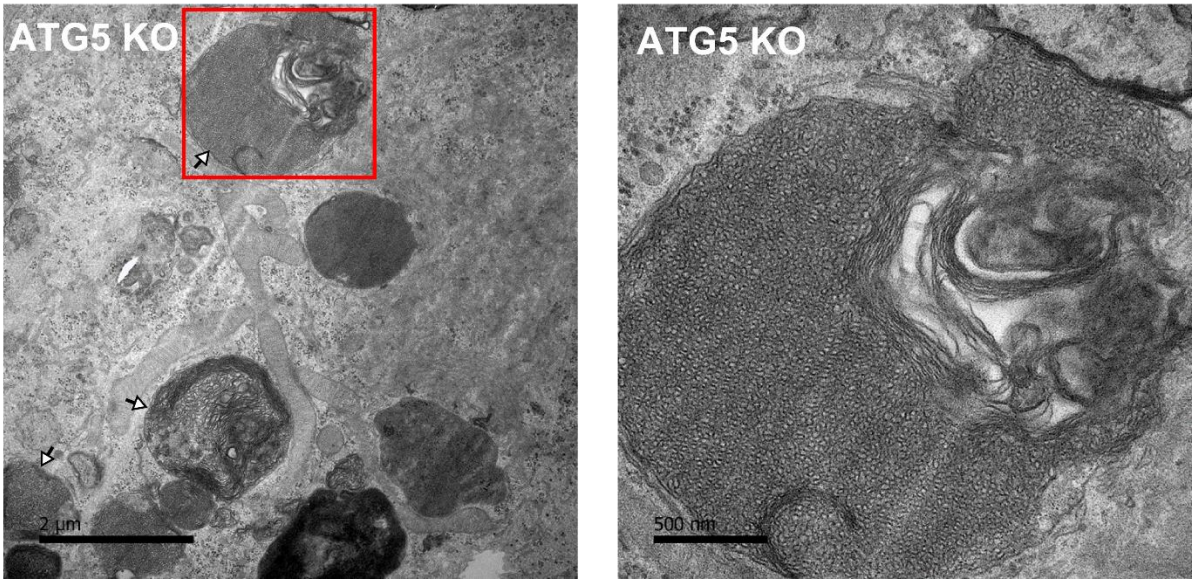

Figure 16. Aberrant membranous structures are formed in ATG5 KO neurons. Electron micrographs of the soma of WT and ATG5 KO cultured neurons at DIV 16. (**a**) Two different pictures from WT neurons. Scale bars: 2µm (left) and 1 µm (right). (**b**) Picture from ATG5 KO soma illustrating several aberrant membranous structures (arrows). The red rectangular box depicts an area magnified to the right. Scale bars: 2µm (left), 0.5µm right (right).

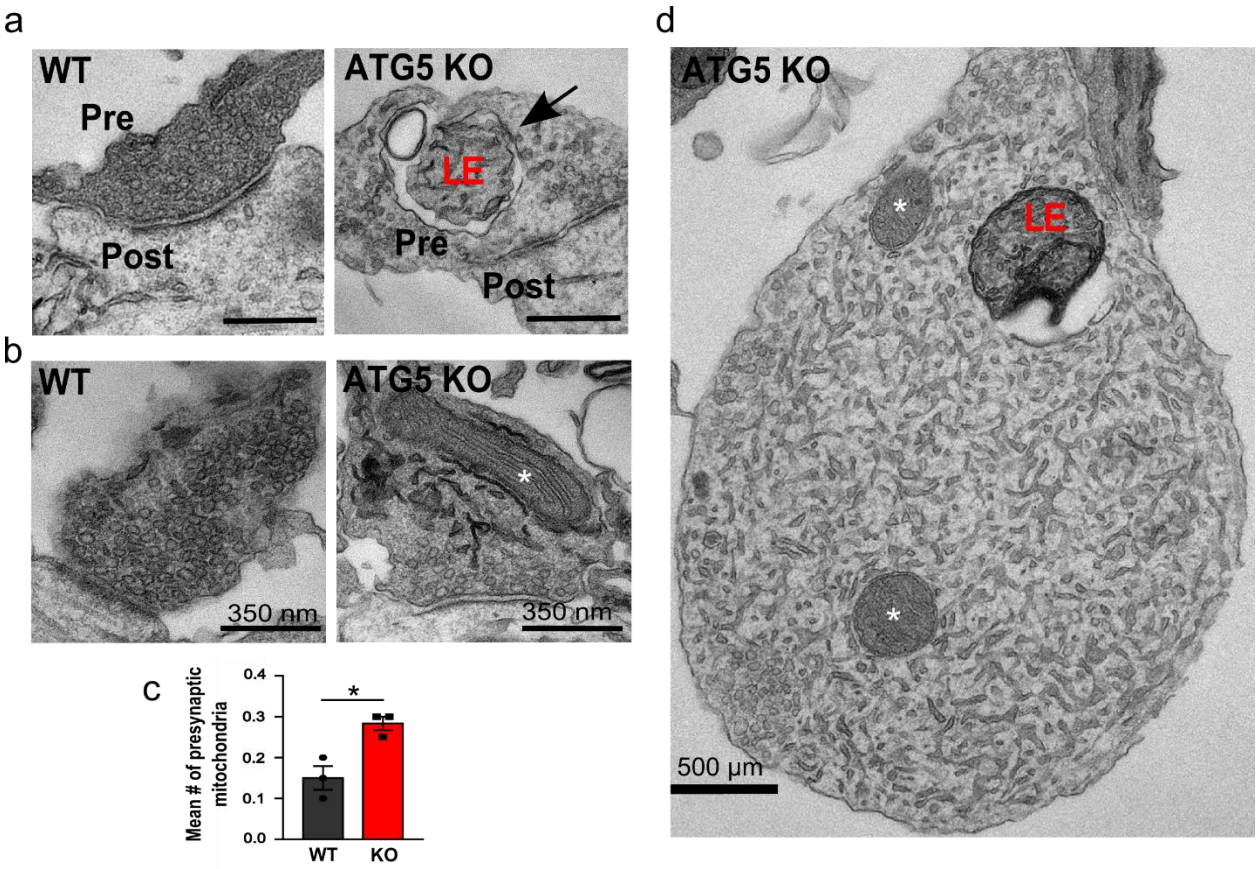

Figure 17. Axonal swellings from ATG5 KO neurons retain mitochondria, endosome- and tubular ER-like structures. Electron micrographs of synapses from cultured WT and ATG5 KO neurons at DIV 16. (**a**) Endosome-like structures were found at presynapses (Pre). LE: late endosomes-like structures (arrow). Scale bars: 200nm. (**b**,**c**) The average number of mitochondria is significantly increased within 500nm of the active zone in ATG5 KO presynapses compared to controls. WT: 0.15±0.03, KO: 0.28±0.02, p=0.016, N=3, 60 synapses per condition. (**c**) Representative axonal swelling from an ATG5 KO axon filled with ER-like structures.

To confirm that membranous structures accumulate in ATG5 KO neurons, cultured neurons were also analyzed by immunocytochemistry. Axonal swellings accumulated the late endosomal marker RAB7 (**Fig.18a,b**). Moreover, live-imaging of mito-mCherry-transfected WT and ATG5 KO neurons revealed not only an increased accumulation of mitochondria in the KO condition, but also a decreased number of moving mitochondria along the axon (**Fig.18c,d**).

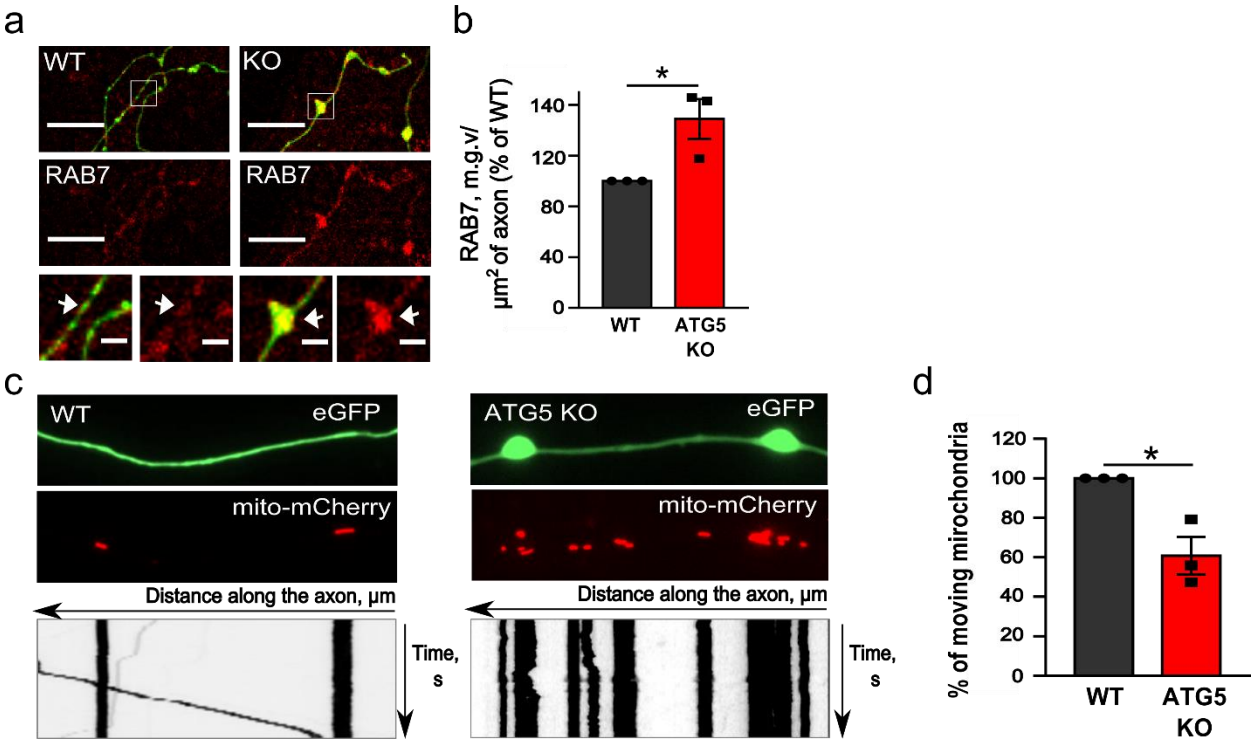

Figure 18. Axonal swellings accumulate RAB7-positive structures and mitochondria, which suffer from impaired axonal mobility in ATG5 KO cultured neurons. (**a**,**b**) RAB7-containing puncta density in axons of eGFP-transfected WT and ATG5 KO neurons at DIV 15-17. KO: 148.84±15.63%. p=0.044. In total, 27 WT and 25 KO axons from N=3. Fluorescent levels in the KO were normalized to the WT set to 100%. Scale bars: 10µm upper panels, 2µm lower panels. (**c**,**d**) Mito-mCherry (mCherry containing the mitochondrial targeting sequence)and eGFP co-transfection of WT and ATG5 KO neurons. KO: 60.83±7.79%, p=0.02, N=3. Axonal mobility of mitochondria in KO condition was normalized to the WT set to 100%. All data shown represent the mean ± SEM from N independent experiments.

Ongoing experiments in the laboratory are trying to identify the nature of accumulated ER-like structures in axonal swellings from ATG5 KO neurons. So far, data failed to identify them with the ER marker protein disulfide isomerase (PDI) (Hewett et al., 2000) and by overexpression of the fluorescence-tagged ER targeting sequence KDEL (Valdes et al., 2012). Furthermore, our preliminary data (done as a part of the revision for the manuscript submitted to Nature Communications) do not support the hypothesis that ER-like tubules in autophagy-deficient neurons may correspond to pre-autophagic structures incapable of autophagosome enclosure, since these structures are not positive for the phagophore markers ATG13, ATG9A, WIPI2, and FIP200, upstream proteins from the ATG5 recruitment. In addition, markers of ER-stress response were preliminarily tested by analyzing the levels of phosphorylated eIF2α (p-eIF2α), which is known to be phosphorylated upon ER stress (Remondelli and Renna, 2017). Levels of

p-eIF2α appeared to be unchanged in ATG5 KO neurons compared to WT (**Fig.19a,b**). Future experiments may conclude this result by comparing the phosphorylated levels/total levels of p-eIF2α.

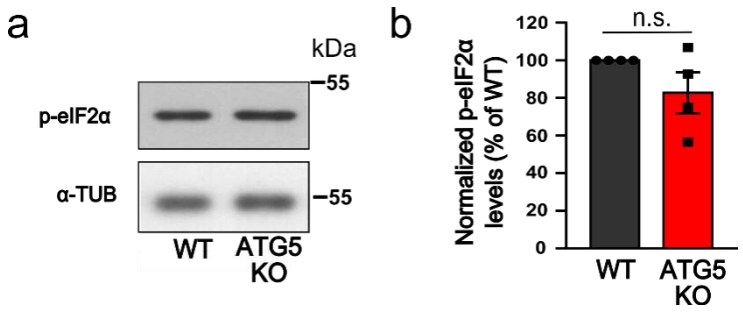

Figure 19. ATG5 KO neurons may not have an ER stress response. (**a**,**b**) Western blot analysis of phosphor-eIF2α (Serine 51) levels in WT and ATG5 KO at DIV 16. KO: 82.75±10.91, p=0.1651, N=4. n.s.-non significant. All data shown represent the mean ± SEM from N independent experiments.

All membranous structures found accumulated within axonal swellings have the common property of been trafficked along the axons via the MT-based trafficking machinery (Farias et al., 2019; Maday et al., 2014). Moreover, reduced mitochondria mobility enforced the hypothesis that ATG5 KO neurons may suffer from impaired axonal trafficking of intracellular cargo. To elucidate this hypothesis, the levels of the MT-associated dynein activator Dynactin (DYNC1) were examined in axonal spheroids of ATG5 KO neurons by immunocytochemistry. Data revealed that whereas in control axons DYNC1 shows a longitudinal appearance, likely corresponding to its association with MT-based motor dynein, ATG5 KO neurons revealed large spheroid-like accumulations of DYNC1 (**Fig.20a,b**). Furthermore, these DYNC1-positive accumulations contained activated tropomyosin-related kinase receptor B (TRKB) receptors (**Fig.20c,d**), a known cargo of dynein motors in axons (Kononenko et al.,2017).

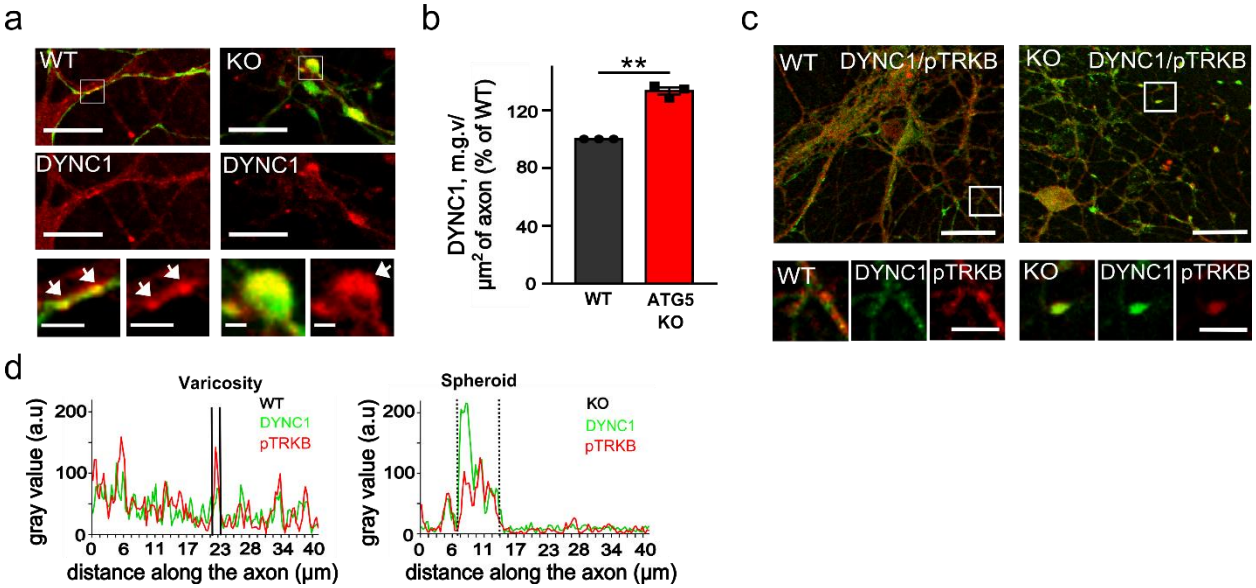

Figure 20. Axonal swellings accumulate components of retrograde MT-based trafficking. (a,b) DYNC1-containing puncta density in axons of eGFP-transfected of WT and ATG5 KO neurons. KO: 133.26±2.53%), p=0.003. In total, 28 WT and 27 KO axons from N=3. Fluorescent levels in the KO were normalized to the WT set to 100%. Scale bars in (a): upper panels, 10µm, lower panels, 2µm.(**c**) Confocal images of WT and ATG5 KO neurons immunostained for DYNC1 (green) and phosphorylated TRKB receptors (Py816TRKB) (red). Scale bars: upper panels, 30µm, lower panels, 10 µm. (**o**) Representative fluorescent profiles through the axons of WT and ATG5KO neurons, illustrating the accumulation of DYNC1 and pTRKB within axonal spheroids in KO condition. All data shown represent the mean ± SEM from N independent experiments.

To ultimately prove the hypothesis that ATG5 KO neurons have defective axonal trafficking, fluorescently-tagged TRKB (TRKB-mRFP) construct was transfected in WT and ATG5 KO neurons and monitored by live imaging (**Fig.21a**). In line with mitochondria results, the relative number of TRKB-positive vesicles moving anterogradely and retrogradely along the axon was significantly reduced in ATG5 KO condition compared to the WT (**Fig.21b**). Furthermore, speed analysis of TRKB-positive vesicles revealed that the retrograde velocity, but not the anterograde, is impaired in axons of ATG5-deficient neurons (**Fig.21c**).

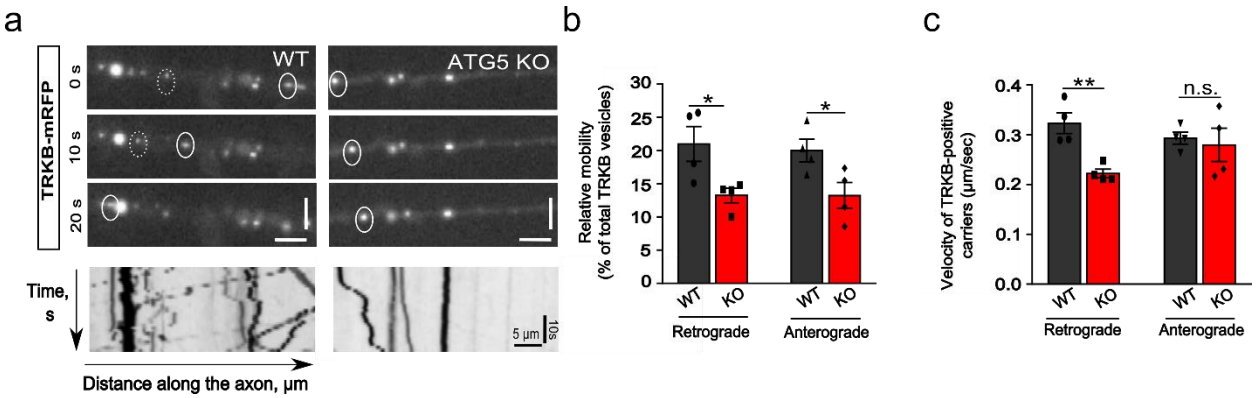

Figure 21. Trafficking of TRKB-positive vesicles along the axon is impaired in ATG5-deficient neurons. (a) Representative images at different time points and respective kymographs of TRKB-mRFP carriers. (**b**) Loss of ATG5 significantly decreased the mobility of TRKB carriers compared to WT controls. WT^{Retro}: 20.99±2.63%, KO^{Retro}: 13.23±1.09%, WT^{Antero}: 20.00±1.72%, KO^{Antero}: 13.22±1.97%. p^{Retro}=0.034, p^{Antero}=0.041. In total, 29 neurites per each condition from N=4. (**c**) Loss of ATG5 significantly decreased the retrograde TRKB velocity compared to WT controls. WT^{Retro}: 0.32±0.02µm/s, KO^{Retro}: 0.22±0.01µm/s, WT^{Antero}: 0.29±0.01µm/s, KO^{Antero}: 0.28±0.03µm/s). p^{Retro}=0.004, p^{Antero}=0.721.In total, 29 neurites per each condition from N=4. n.s.-non significant. All data shown represent the mean ± SEM from N independent experiments.

Taken together, these results demonstrate that axonal swellings under conditions of defective LC3 lipid conjugation machinery are not a result of inadequate clearance of protein inclusions, and instead accumulate ER-structures and components of MT-based trafficking machinery, including RAB7-positive structures, mitochondria, and TRKB-activated receptors. Furthermore, this phenotype is accompanied by defective axonal trafficking, presumably due to a novel LC3 function since modulation of non-lipidated LC3 levels is able to decline or rescue the axonal pathology.

3.4 LC3 lipidation-deficient neurons have impaired MT-dynamics

Initially, LC3 was identified in rat brain samples as a protein associated with microtubules (MTs). Based on this, LC3 was proposed to influence the binding of MAP1A and MAP1B to the tubulin cytoskeleton (Mann and Hammarback, 1994). Since LC3I was found to accumulate in axonal swellings of autophagy-deficient neurons (**Fig.13g**), we asked whether accumulated LC3I may bind to MTs and alter their dynamics. To test this hypothesis, endogenous α-tubulin (α-TUB) from WT or ATG5 cultured neuronal lysates was immunoprecipitated, and LC3A/B was co-

immunoprecipitated with a specific antibody. To investigate the LC3 association specifically with soluble and polymerized MTs fractions, we adopted a previously published protocol for extraction of soluble and polymerized MTs to our cultured primary neurons (Sharma et al., 2011a). Interestingly, in both WT and KO conditions, only a tiny fraction of LC3I was found to be associated with α-tubulin in either soluble or polymerized MT fractions (**Fig.22a,b**).

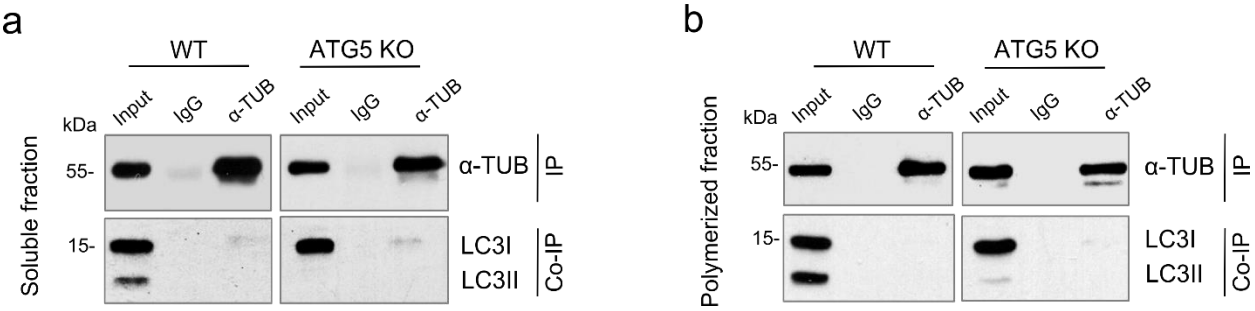

Figure 22. LC3A/B barely associates with soluble α-tubulin or MTs. Immunoprecipitation of either IgG (negative control) or α-tubulin in soluble-tubulin fractions (**a**) or in polymerized-tubulin fractions (**b**) from cultured WT and ATG5 KO neurons. Inputs, 5% from the soluble lysate and 8% from the polymerized lysate. A representative example from N=3 independent experiments.

Although no strong association between LC3 and α-tubulin could be detected in autophagy-deficient neurons, axonal traffic jams have been largely reported to be a consequence of impaired MT dynamics in the axon (Wang et al., 2012). Thus, we next investigated whether ATG5 KO neurons suffer from impaired MT dynamics. To test this, we monitored the dynamics of the plus-end MT-binding protein EB3-tdTomato in cultured WT and KO neurons. EB3 binds to the plus-end tip of the growing MT, thus allowing for tracking polymerization rates, so-called “comets” (Stepanova et al., 2003). Interestingly, whereas EB3-positive comets were evident along control axons, the overall number of EB3-positive comets were severely decreased in ATG5 KO condition, a phenotype rescued by the re-expression of ATG5 (**Fig.23a,b**). Similarly, ATG16L1 KO neurons displayed a significant reduction in the number of polymerization events (**Fig.23c,d**). Thus, deficient LC3-lipidation reduces the dynamism of the MT cytoskeletonin neurons.

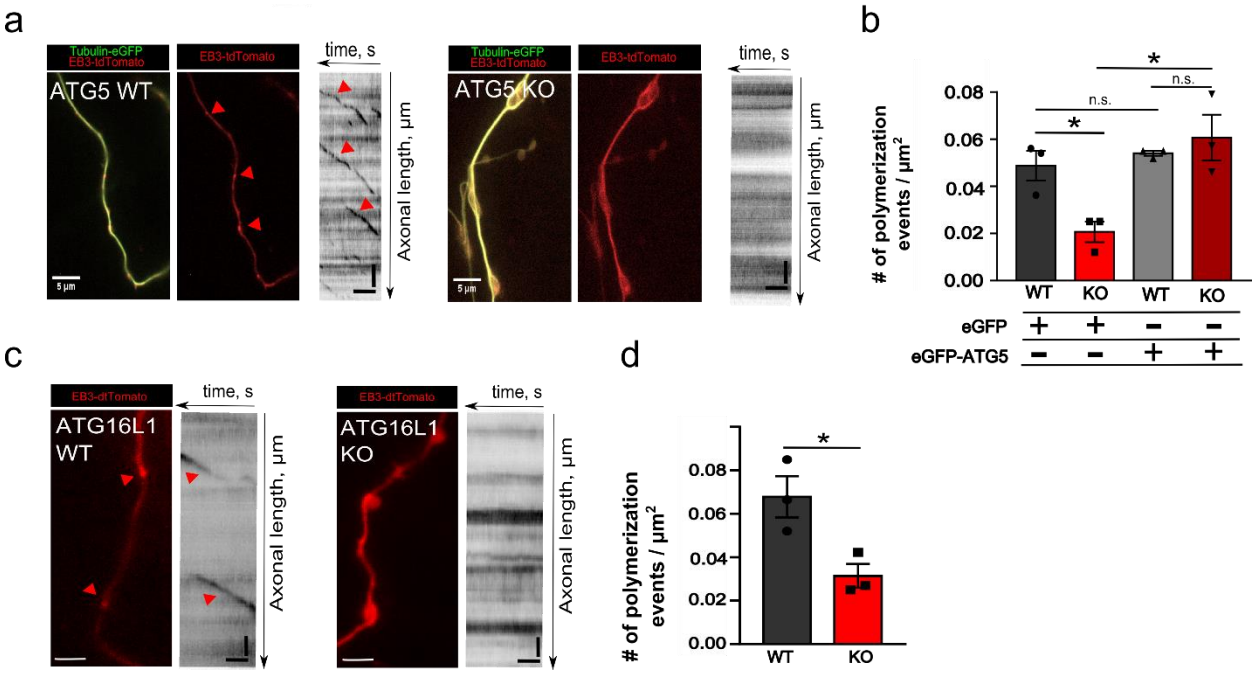

Figure 23. Defective MT dynamics in ATG5- and ATG16L1-deficient neurons. (**a**) Representative fluorescent images from time-lapse videos of WT and ATG5 KO neurons co-transfected with Tubulin-eGFP and EB3-tdTomato. Corresponding kymographs are shown to the right. Red arrows indicate retrograde EB3 comets. Scale bars; x=5µm, y=30s. (b) Analysis of EB3 comet density in axons from (**b**). WT^{GFP}: 0.05±0.01, KO^{GFP}: 0.02±0.00, or with eGFP-ATG5; WT^{ATG5}: 0.05±0.00, KO^{ATG5}: 0.06±0.01. pWT^{GFP} vs KO^{GFP} =0.032, pKO^{GFP} vs KO^{ATG5} =0.019. In total, 45 WT and 50 KO axons from N=3. (**c**) Representative fluorescent images from time-lapse videos of WT and ATG16L1 KO neurons transfected with EB3-tdTomato. Corresponding kymographs are shown to the right. Red arrows indicate retrograde EB3 comets in WT neurons, which are absent in KO. Scale bars, x: 5µm, y: 30s. (**d**) EB3 comet density from c. WT: 0.07±0.01, KO: 0.03±0.01. p=0.029: In total, 27 WT and 26 KO axons from N=3. n.s.-non significant. All data shown represent the mean ± SEM from N independent experiments.

3.4.1 MTs are more stable in ATG5 and ATG16L1 KO neurons

Since MTs appear to be less dynamics in ATG5- and ATG16L1-deficient neurons, an engaging scenario suggests that autophagy-deficient MTs are generally hyperstable. To answer that, first, the amount of labile and stable MTs were quantified by analyzing the levels of tyrosinated and detyrosinated α-tubulin. Tyrosinated α-tubulin is found in dynamics segments of MTs, such as the growth cone. Oppositely, detyrosinated α-tubulin is enriched labels stable parts of MTs (Cambray-Deakin and Burgoyne, 1987). Western blot analysis of tubulin polymerized fractions showed a significant decreased in tyrosinated α-tubulin (Y α-TUB) in ATG KO neurons compared to the WT,

whereas detyrosinated α-tubulin (deY α-TUB) levels were upregulated (**Fig.24a**). Similarly, the levels of acetylated (Ac-TUB) and Δ2 tubulin (Δ2-Tub), PTMs of α-tubulin occurring exclusively in stable MTs, were found to be upregulated in ATG5- (**Fig.24c-f**) and ATG16-deficient neurons (**Fig.24g-i**). Importantly, changes observed in PTMs of α-tubulin were not due to altered levels of total α-tubulin in ATG5 KO neurons compared to WT (**Fig. 24j**).

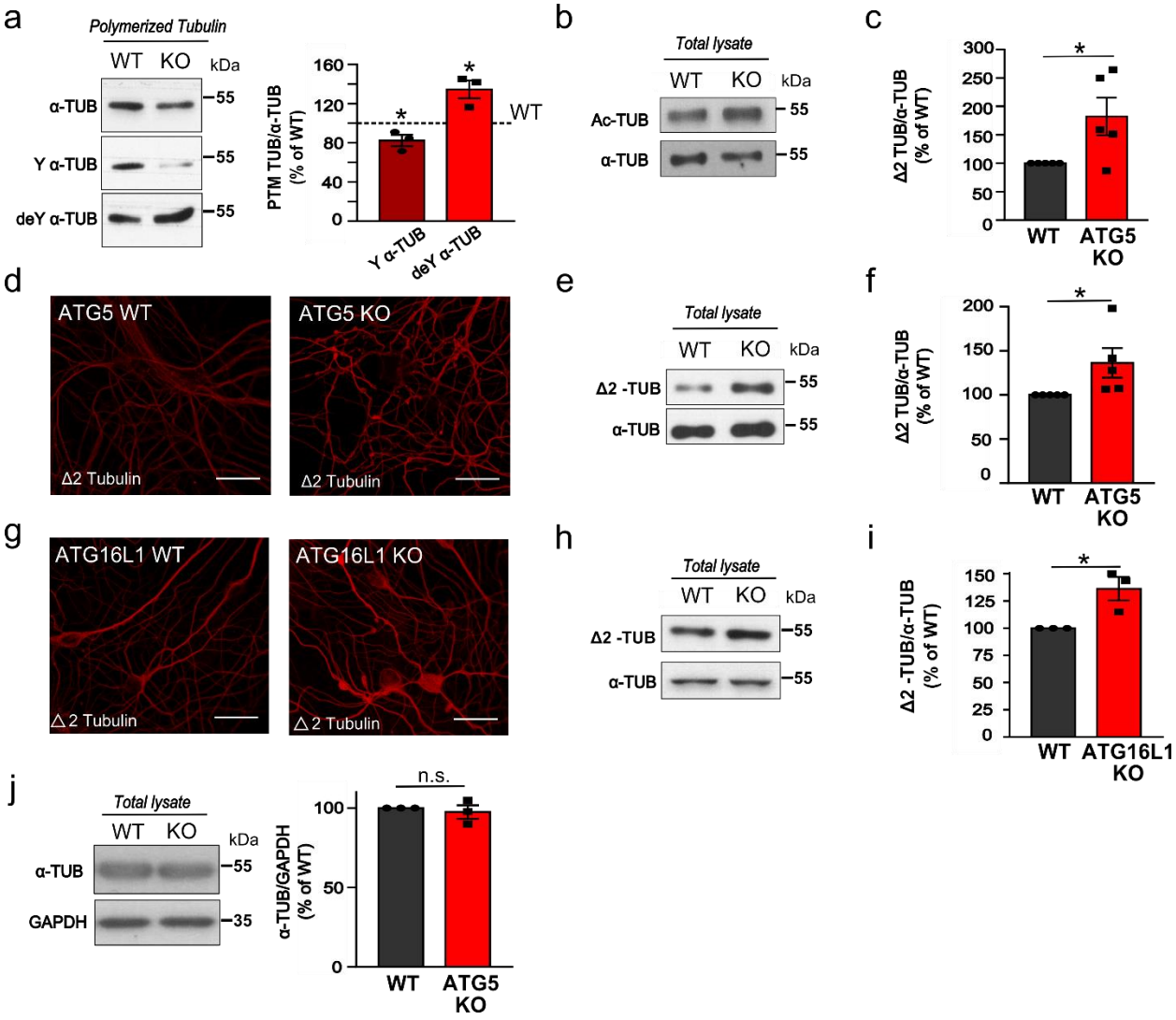

Figure 24. Increased stable-resident PTM of α-tubulin in ATG5- and ATG16L1-deficient neurons. (**a**) Western blot analysis from polymerized MTs isolated from ATG5 KO neurons compared to the WT set to 100%. Tyrosinated (Y) α-tubulin levels are significantly decreased: $KO^{Y\ \alpha\text{-Tubulin}}$: 82.25±5.75%, p=0.045, N=3, while the levels of detyrosinated (deY) α-tubulin are significantly upregulated: $KO^{deY\ \alpha\text{-Tubulin}}$: 134.49.25±9.09%, p=0.032, N=3. (**b**,**c**) Levels of acetylated tubulin (Ac) are significantly increased in lysates from cultured ATG5 KO neurons compared to controls: KO: 182.25±33.07%. Protein levels in KO

condition were normalized to the WT set to 100%. p=0.034. N=5. (**d**) Representative fluorescent images of cultured WT and ATG5 KO neurons immunostained for Δ2 α-Tubulin. Scale bars, 50µm. (**e,f**) Δ2 α-Tubulin levels are significantly increased in lysates of ATG5 KO neurons compared to the WT set to 100%. KO: 136.13±16.78%, p=0.049, N=5. (**g**)Representative fluorescent images of cultured WT and ATG16L1 KO neurons immunostained for Δ2 α-Tubulin. Scale bars: 50µm. (**h,i**) Δ2 α-Tubulin levels are significantly increased in lysates of ATG16L1 KO neurons compared to the WT set to 100%. KO: 136.18±10.79%, p=0.039, N=3. (**j**)Levels of α-tubulin are not changed in ATG5 KO neurons compared to the WT. KO: 97.51±4.28%.Protein levels in KO condition were normalized to the WT set to 100%. p=0.593, from N=3.n.s.-non significant. All data shown represent the mean ± SEM from N independent experiments.

Having shown that ATG5 and ATG16L1 KO neurons have increased levels of stable MTs, we wanted to ultimately prove the increased MT stability in KO condition by treating ATG5 KO neurons with the MT disassembly drug nocodazole (Fassier et al., 2013). In line with previous results, ATG5 KO neurons were resistant to the nocodazole after 40 min of treatment, whereas WT neurons started to display MT depolymerization after 10 min of treatment (**Fig.25a,b**). Taken together, these data reveal that the loss of core autophagy machinery involved in lipid conjugation of LC3 regulates MT stability in neurons.

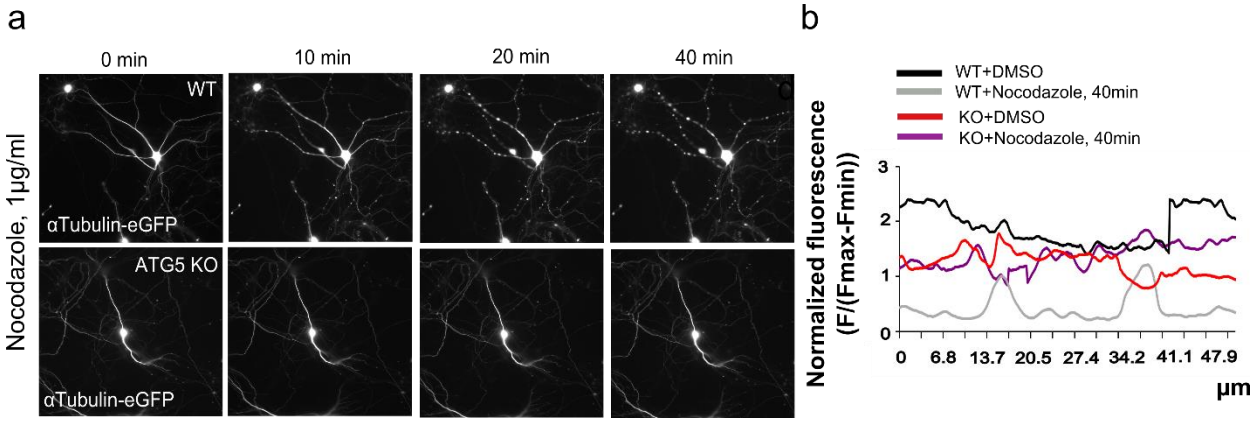

Figure 25. Hyperstability of MTs in ATG5 KO neurons. (**a**) Time-lapse images of WT and ATG5 KO neurons transfected with α-tubulin-eGFP treated with 1µg/ml of nocodazole for 40 min. (**b**) WT neurons treated with nocodazole have a profound loss of α-tubulin-eGFP immunofluorescence along the neurite. In contrast, ATG5 KO neurons either treated with DMSO or with nocodazole were indistinguishable from DMSO-treated controls.

3.5 LC3A and LC3B, but not GABARAPL1, associate with the active zone protein ELKS1

Thus far, these data suggest a model where increased levels of LC3I are causative of impaired axonal trafficking and formation of axonal swellings. However, the exact molecular mechanism by which increased LC3I levels modulate MT dynamics remained elusive. Since LC3 itself barely binds to MTs (**Fig.22**), we searched for new possible interacting partners of LC3 by mass spectrometry. LC3A/B was immunoprecipitated from lysates of adult mouse brain cortex, and its interaction partners were analyzed by another PhD student from the lab (Melina Overhoff), together with the CECAD proteomic facility. This is the reason why these data are not shown in this thesis. Interestingly, one of the highest hits corresponded to the ELKS1 (glutamic acid/leucine/lysine/serine-rich protein 1, also known as RAB6IP2, CAST2, or ERC1 (Monier et al., 2002)). ELKS1 is a scaffolding protein ubiquitously expressed, but abundantly found in the brain, where it mainly localizes at the active zone of presynaptic terminals (Wang et al., 2002). Intriguingly, ELKS1 is known to regulate MT dynamics via its interaction with the MT-associated protein CLASP in non-neuronal cells (Lansbergen et al., 2006). To investigate whether this function of ELKS1 is conserved in neurons, we first verified the interaction of LC3 and ELKS1 by performing a co-immunoprecipitation assay in HEK cells. Ectopically expressed ELKS1, tagged with tdTomato, was co-immunoprecipitated either eGFP-LC3A (**Fig.26a**) or eGFP-LC3B (**Fig.26b**), comparing to control HEK cells only transfected with GFP. In contrast, GABARAPL1, another member of the LC3/GABARAP family, did not interact with tdTomato-ELKS1 (**Fig.26c**). Reciprocally, eGFP-LC3A and eGFP-LC3B were co-immunoprecipitated with tdTomato-ELKS1 (**Fig.26d,e**). Moreover, pull-down experiments with native proteins *in vitro* confirmed that ELKS1 and LC3 directly interact (**Fig.26f**).

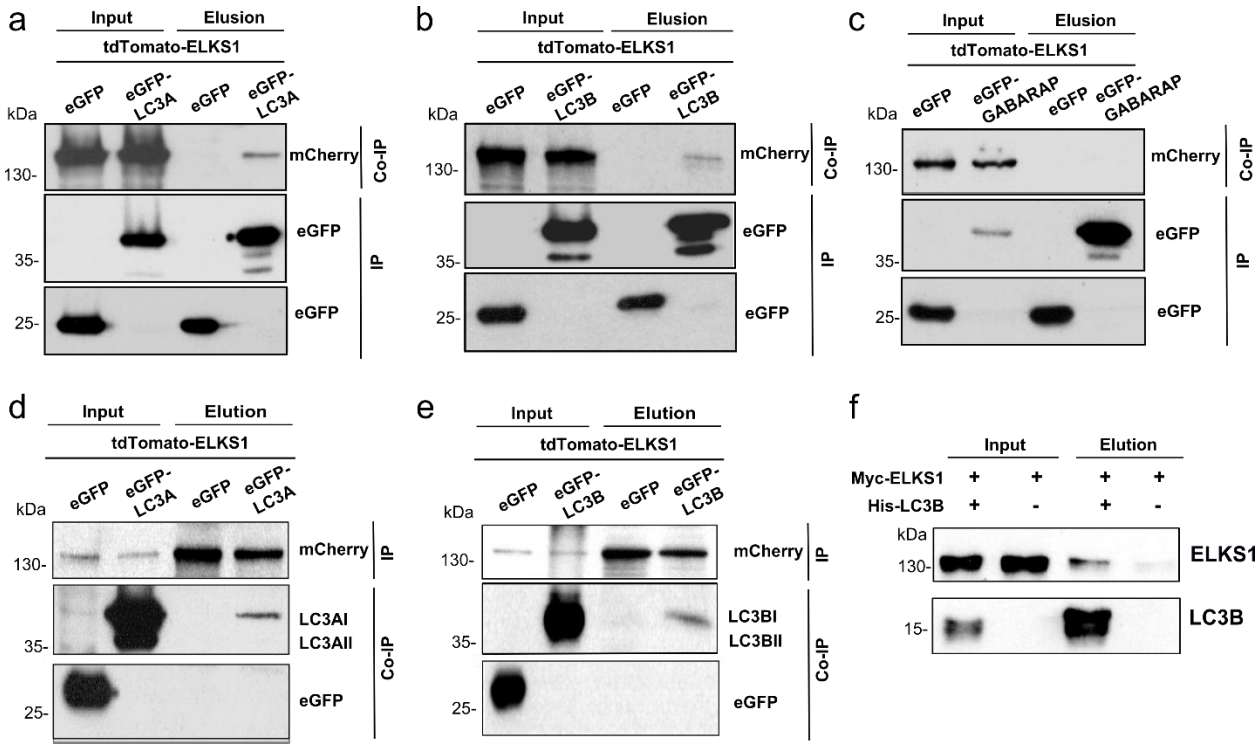

Figure 26. LC3 directly associates with ELKS1 *in vitro*.Ectopically expressed ELKS1, tagged with tdTomato is co-immunoprecipitated (Co-IP) with eGFP-tagged LC3A (**a**) and LC3B (**b**) but not with GABARAP (**c**). HEK cell lysates were directly analyzed (Input) or subjected to GFP immunoprecipitation (Elution) and further immunoblotted against mCherry (Co-IP). Input, 1% of the total lysate was added to the assay. (**d,e**) Ectopically expressed LC3A and LC3B, tagged with eGFP are co-immunoprecipitated with tdTomato-ELKS1. HEK cell lysates were directly analyzed (Input) or subjected to ELKS1 immunoprecipitation (Elution) and further immunoblotted against GFP (Co-IP). Input, 1% of the total lysate was added to the assay. (**f**) Purified recombinant His_6-LC3B, detected by immunoblotting with LC3B antibody directly binds Myc-ELKS1. Input, 5% of the total recombinant LC3B added to the assay.

Next, ELKS1-LC3 interaction was investigated in neurons. Immunofluorescence analysis of co-transfectedtdTomato-ELKS1 and eGFP-LC3B cultured WT neurons showed an 80% overlap coefficient between these two proteins (**Fig.27a,b**).

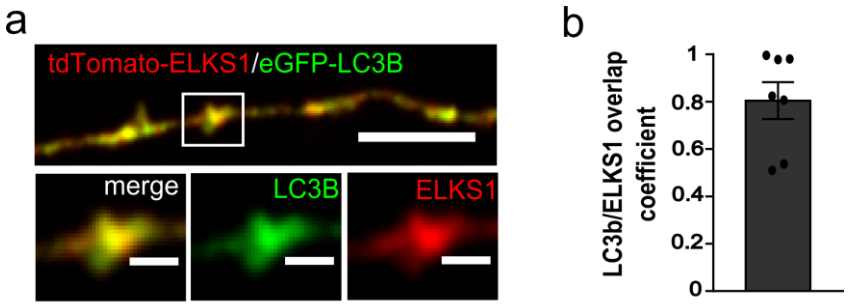

Figure 27. Close co-localization of tdTomato-ELKS1 and eGFP-LC3B in WT axons. (a) Axons of primary WT mouse neurons co-transfected with tdTomato-ELKS1 (red) and eGFP-LC3B (green). Scale bars: 5µm (upper panel), 1µm (lower panels). (b) Analysis oftdTomato-ELKS1 and eGFP-LC3Bco-localization by Mander´s overlap coefficient: 80.42±7.22 %. N=7. Data shown represent the mean ± SEM from N independent experiments.

3.6 LC3 regulates MT stability via ELKS1/CLASP2 function

Given that LC3 associates with ELKS1 in neurons, we next determined whether ELKS1-CLASPs function might mediate MT stability in LC3 lipidation-deficient neurons. To investigate that, first, protein levels of ELKS1 were analyzed in ATG5 KO neurons in *vitro* and *in vivo*. ELKS1 levels were found significantly upregulated in lysates from cultured neurons (**Fig.28a,b**) and within the brain (**Fig.28d,e**) of neurons lacking ATG5. Indeed, ELKS1 accumulated within axonal swellings of cultured neurons lacking the LC3 lipid conjugation machinery (**Fig.28c**). Since ELKS1 could be accumulated due to defective degradation via autophagy, ELKS1 proteins levels were studied upon treatment with BafilomycinA, an inhibitor of the V-type ATPase that blocks lysosomal degradation. Strikingly, we found that ELKS1 is not degraded via autophagy (**Fig.28f**). Thus, these data suggest that LC3 regulates ELKS1 via a non-canonical degradation independent pathway.

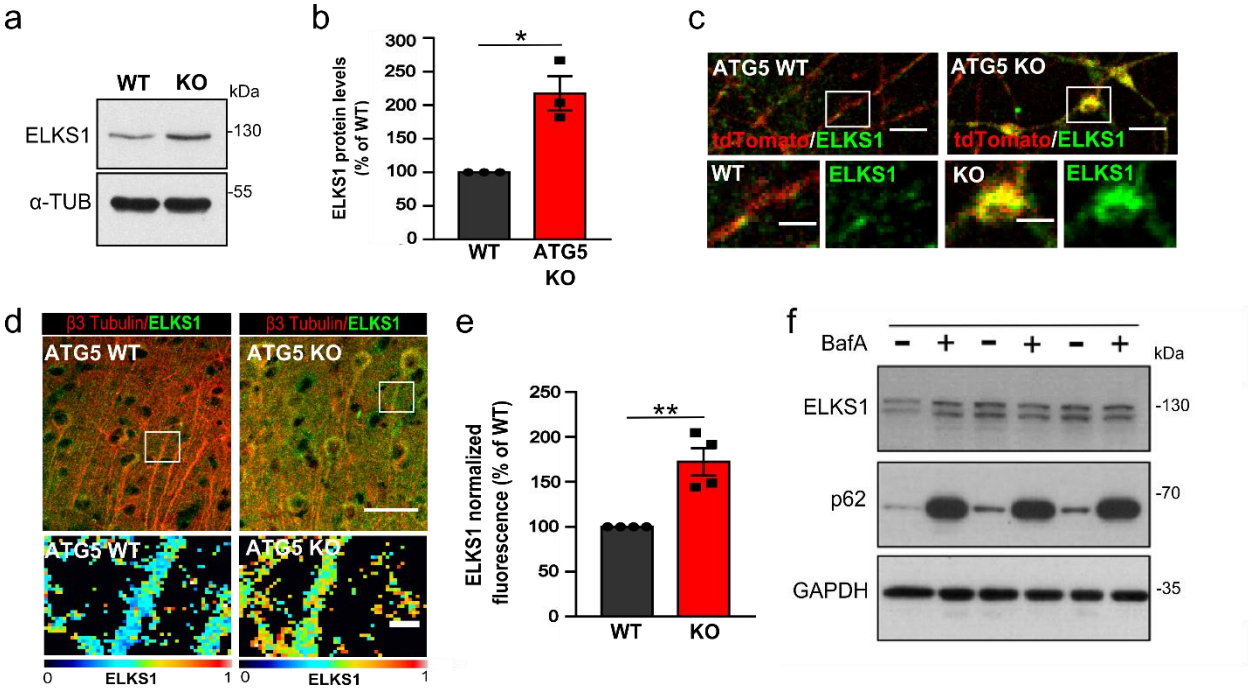

Figure 28. ELKS1 levels are stabilized in ATG5 KO neurons via an independent degradation mechanism.(**a**,**b**) Western blot analysis of ELKS1 levels in cultured ATG5 KO neurons compared to the WT set to 100%. KO: 217.44±25.52%. p=0.022. N=3. (**c**)Cultured neurons from WT and ATG5 KO mice, carrying tdTomato allele as a reporter of Cre-recombination (red), were immunostained for ELKS1 (green). White boxes depict the magnified areas underneath. Scale bars, 10μm upper panels, 4μm lower panels. (**d**) Representative confocal images of cortical sections from WT and ATG5 KO mice immunostained for ELKS1 (green) and co-immunostained for β3-Tubulin (red) to reveal neuronal processes. In lower panels, ELKS1 fluorescent intensity in neurites was false color-coded with warm colors representing high intensities. Scale bars, 50μm upper panels, 5μm lower panels. (**e**)ELKS1 levels are significantly increased in ATG5 KO brains compared to the WT set to 100%. KO:180.12±15.20%. p=0.009. N=4. (**f**) ELKS1 protein levels upon 67μM BafilomycinA (BafA) or vehicle solution (DMSO) treatments for 16h in NSC34 neuronal-like cell line. p62 blot illustrates the inhibition of the autophagy-lysosome degradation pathway. All data shown represent the mean ± SEM from N independent experiments.

3.6.1 CLASP2 levels are increased in neuronal processes of ATG5 KO mice

Next, we investigated CLASP2 protein levels in WT and ATG5 KO neurons. In line with ELKS1 data, CLASP2 levels were upregulated in ATG5 KO mouse brain (**Fig.29a,b**). Moreover, superresolution STED imaging highlighted an increased abundance of CLASP2 association along MTs in ATG5 KO cultured neurons compared to WT (**Fig.29c,d**). Collectively, these data suggest

that ELKS1 retention via LC3I accumulation in ATG5 KO neurons alters the levels of the MT stabilizing protein CLASP2.

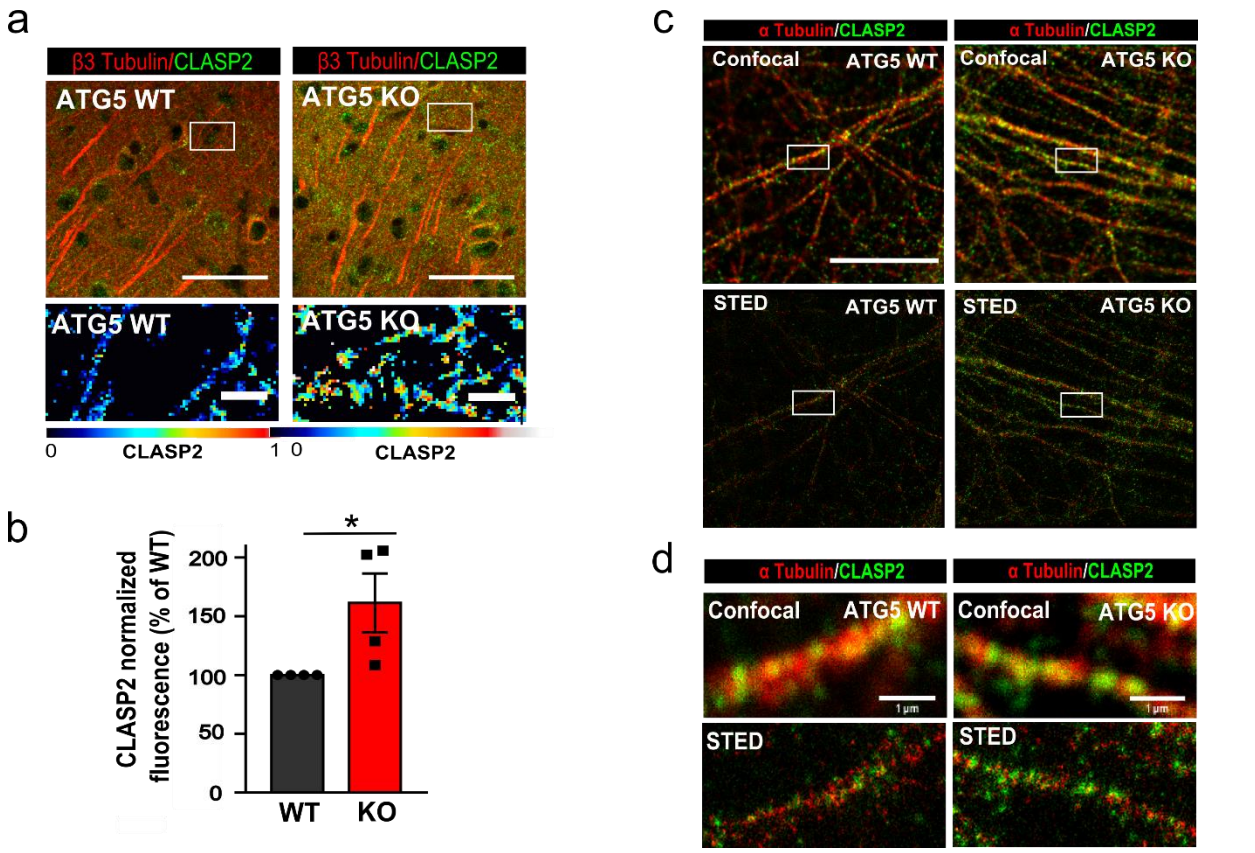

Figure 29. CLASP2 levels are increased in KO axonal swellings. (**a**) Representative confocal images of cortical sections from WT and ATG5 KO mice immunostained for CLASP2 (green) and co-immunostained for β3-Tubulin (red) to reveal neuronal processes. In lower panels, CLASP2 fluorescent intensity in neurites was false color-coded with warm colors representing high intensities. Scale bars, 50µm upper panels, 10µm lower panels. (**b**) CLASP2 levels are significantly increased in ATG5 KO brains compared to the WT set to 100% (179.08±25.04%). p=0.046.N=4. (**c**,**d**) Confocal and STED images of neurons of CLAPS2 (green) and α-tubulin (red). White rectangular boxes depict images in e. Scale bars: 10µm. (e) Amplified images from d. Scale bars: 1µm. All data shown represent the mean ± SEM from N independent experiments.

3.6.2 Non-lipidated LC3 regulates MT dynamics via ELKS1-CLASP2 dependent mechanism in axons

Thus far, we hypothesized that the non-lipidated LC3 stabilizes ELKS1-CLASP2 within the axon, which in turn may alter MT dynamics in LC3 lipidation-deficient neurons. To test this hypothesis,

first, levels of ELKS1 in axonal swellings were analyzed upon LC3 KD (see **Fig.13e,f** for siRNA validation). In line with our hypothesis, LC3 KD not only rescued axonal swellings after 7 days post-transfection (**13g,h**), but also caused a 30% reduction of ELKS1 protein density within spheroids (**Fig.30a,b**). Interestingly, these data suggested that reduction of ELKS1 levels in axons might also rescue the formation of spheroids in ATG5 KO neurons. Thus, smart pools of siRNAs against *Elks1* were used. **Fig.30c,d** shows ELKS1 KD validation in NSC34 cells after 72h post-transfection. In neurons, although only a 30% of reduction in ELKS1 protein levels was detected after 7 days of transfection (**Fig.30e,f**), this KD period was enough to significantly reduce the average size of axonal swellings in ATG5 KO neurons (**Fig.30e,g**). Moreover, ELKS KD was also accompanied by a significant reduction of CLASP2 protein levels within spheroids (**Fig.30h,i**). Ultimately, the deletion of ELKS1 in autophagy-deficient neurons was sufficient to completely rescue impaired MT dynamics, monitored by the expression of EB3-tdTomato in WT and ATG5 cultured neurons (**Fig.30j,k**). Taken together, these data demonstrate that dysfunctional LC3 lipidation, and its subsequent accumulation, alters MT dynamics via controlling the abundance of ELKS1-CLASP2 within axons.

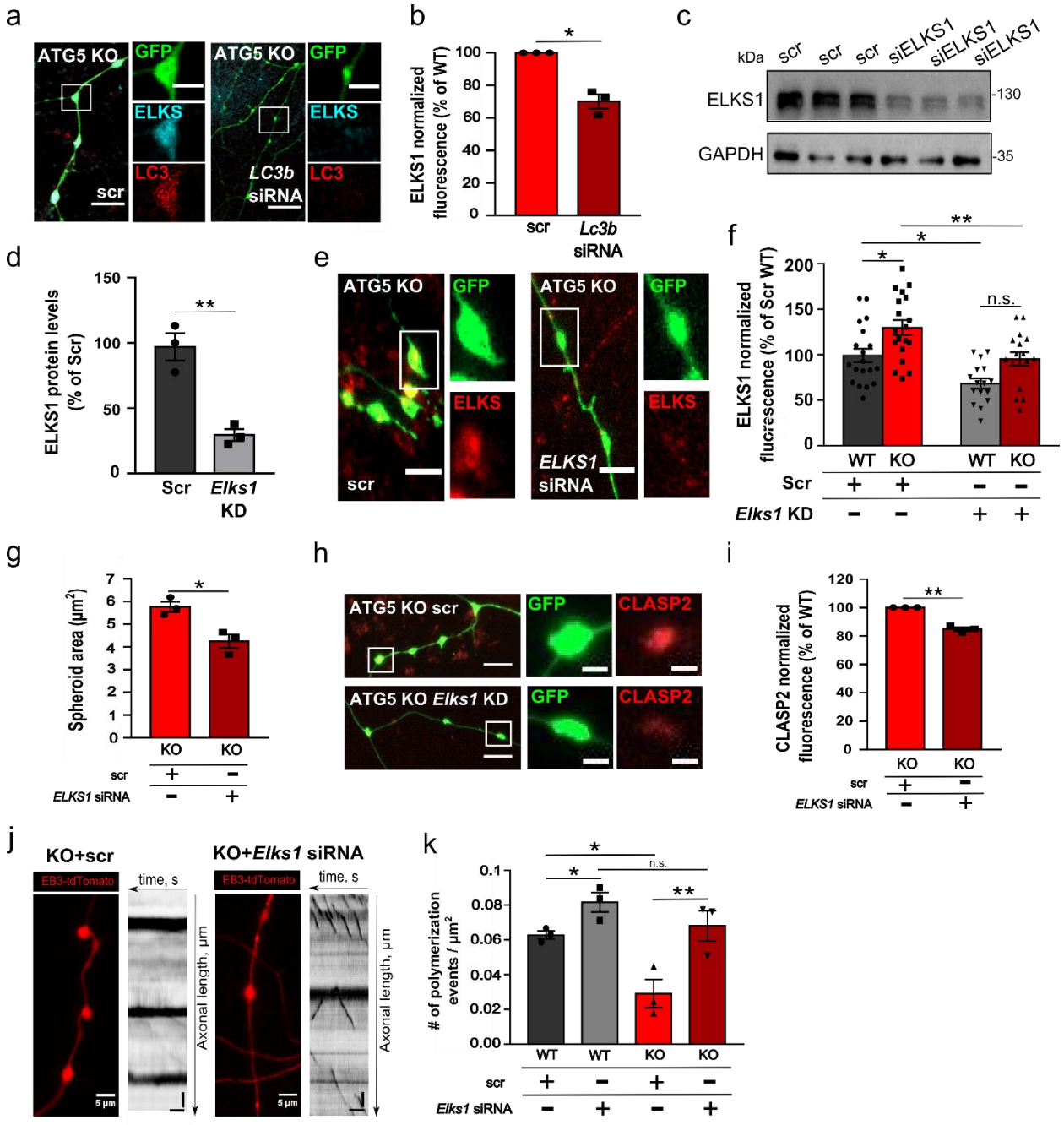

Figure 30. Autophagy lipidation machinery regulates MT dynamics in neurons via ELKS1/CLASP2-dependent mechanism. (**a**)Immunostained for LC3 (red) cultured ATG5 KO neurons, transfected with eGFP (green) and co-transfected either with scrambled siRNA (scr) or siRNA directed against *LC3b*. Scale bars, 10 μm upper panels, 4 μm lower panels. (**b**) ELKS1 levels are significantly decreased in ATG5 KO neurons treated with *LC3B* siRNA. KO^{siLC3B}: 70.1±4.37%. p=0.010.Protein levels in the KO^{siLC3B} were normalized to the KO^{scr} set to 100%. In total, 247 KO^{scr} and 281 KO^{siLC3B} axons from N=3. (**c**,**d**)Levels of ELKS1 are significantly decreased in NSC34 cells treated with either scrambled (scr) or *Elks1* siRNA after

72h. WT: 96.91±10.39%. KO: 29.45±4.58%. p=0.004. N=3 (**e**) Immunostained for ELKS1 (red) WT and ATG5 KO neurons transfected with eGFP (green) and co-transfected either with scr siRNA or *Elks1* siRNA. Scale bars, 5µm. (**f**) Fluorescence analysis of ELKS1 levels in WT or ATG5 KO axons upon scramble or *Elks1* siRNA after 7 days from transfection. WT^{Scr}: 99.09±7.53%, N=19; KO^{Scr}: 129.82±8.2%, N=19; $WT^{Elks1\ KD}$: 68.33±5.56, N=16, $KO^{Elks1\ KD}$: 95.25±7.27%, N=17. p WT^{Scr} vs KO^{Scr}= 0.016, p WT^{Scr} vs $WT^{Elks1\ KD}$=0.023, p KO^{Scr} vs $WT^{Elks1\ KD}$< 0.000, p KO^{Scr} vs $KO^{Elks1\ KD}$= 0.007. (**g**) The spheroid areain ATG5 KO neurons treated with *ELKS1* siRNA ($KO^{siElks1}$: 5.76±0.23µm^2) compared with scramble KO controls (KO^{scr}: 4.25±0.30µm^2). p=0.018. In total, 142 spheroids for KO^{scr} and 125 spheroids for $KO^{siElks1}$, from N=3. (**h**,**i**) Confocal analysis of CLASP2 levels in ATG5 KO axons upon scramble or *Elks*1 siRNA co-transfection with eGFP. KO^{Scr}= 84.82±1.38%. p=0.004. Protein levels in $KO^{Elks1\ KD}$ condition were normalized to the KO^{Scr} set to 100%. N=3. (**j**) Representative fluorescent images from time-lapse videos of ATG5 KO neurons transfected with EB3-tdTomato and co-transfected with either scrambled siRNA (scr) or with siRNA directed against *Elks1*. Corresponding kymographs are shown to the right. Scale bars, x: 5µm, y: 30s. (**k**) EB3 comet density. WT^{scr}: 0.06±0.00, KO^{scr}: 0.03±0.01, *Elks1*siRNA: $WT^{siElks1}$: 0.08±0.01, $KO^{siElks1}$: 0.07±0.01. pWT^{scr} vs KO^{scr} =0.025, pKO^{scr} vs $KO^{siElks1}$=0.004, pWT^{scr} vs $WT^{siElks1}$ =0.041.In total, 53 WT and 55 KO axons from N=3.n.s.-non significant. All data shown represent the mean ± SEM from N independent experiments.

3.7 Loss of MT dynamics in ATG5 KO neurons impairs BDNF/TRKB neurotrophic signaling

Previous work from our laboratory reported that ATG5-deficient neurons have reduced neuronal complexity, presumably due to defective retrograde transport of BDNF/TRKB-positive vesicles (Kononenko et al., 2017b). In line with this publication, data shown in **Fig.21** revealed defective retrograde transport of TRKB-positive vesicles in ATG5 KO neurons. Thus, in this final section, we investigated whether defective TRKB trafficking causes impaired neurotrophic signaling, leading to reduced neuronal arborization in ATG5 KO neurons. Indeed, levels of BDNF-activated TrkB (p-TrkBY816), as well as the main downstream targets, ERK1/2 and AKT, were observed to be reduced in ATG5-deficient neurons (**Fig. 31a,b**). Moreover, since BDNF gene expression is positively regulated by functional TRKB signaling (Tuvikene et al., 2016), we next analyzed *Trkb* and *Bdnf* mRNA expression levels as a readout of TRKB signaling. Analysis of qPCR results revealed that levels of *Bdnf* mRNA, but not *TrkB*, were dramatically diminished in ATG5 KO neurons, thus suggesting a loss of the positive feedback loop (**Fig.31c,d**). Although *TrkB* mRNA levels did not change in ATG5 KO, total protein levels of TRKB were found significantly downregulated compared to the WT (**Fig.31e,f**), thus suggesting that either mRNA translation of

TRKB is reduced, or degradation of the protein TRKB is enhanced in the KO condition. Interestingly, total TRKB expression levels were rescued upon inhibition of the proteasomal activity (also **Fig.31e,f**), a common drug that blocks the β5 subunit of the ß-ring complex in the 20S proteasome core (Goldberg, 2012)). On the other hand, TRKB signaling was also accompanied by a severe reduction in phosphorylated P6 ribosomal protein (pS6) (**Fig.31g,h**), a common marker of the activated mTORC1 pathway (Oh and Jacinto, 2011). Collectively, these data demonstrate that BNDF/TRKB signaling is defective in ATG5-deficient neurons.

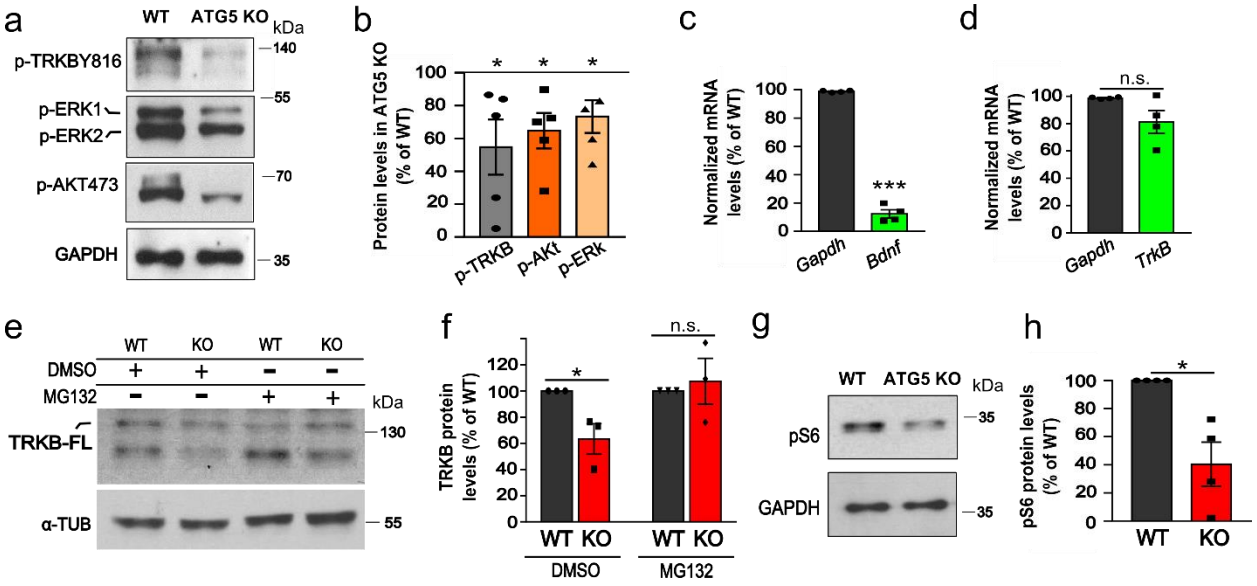

Figure 31. BDNF/TrkB signaling is significantly decreased in ATG5 KO neurons. (**a**,**b**) Lysates from cultured ATG5 KO neurons blotted for p-TRKBY816,ERK1/2, and AKT.Protein levels in the KO were normalized to the WT set to 100%.KO$^{p\text{-}TRKB}$: 54.68±16.78%, p=0.027; KO$^{p\text{-}ERK}$: 73.34±9.94%, p=0.028; KO$^{p\text{-}Akt}$: 64.70±10.82%, p=0.016. N=5. (**c**) *Bdnf* mRNA levels are significantly decreased in cultured ATG5 KO neurons (KO^{Bdnf}: 12.35±2.88%, KO^{Gapdh}: 98.79±0.36%). p<.000. N=4. mRNA levels in KO condition were normalized to the WT set to 100%. (**d**) *TrkB* mRNA levels are non-altered in ATG5 KO neurons (KO^{TrkB}: 81.25±8.37%, KO^{Gapdh}: 98.79±0.36%). mRNA levels in the KO were normalized to the WT set to 100%. (**e,f)** Protein levels of TRKB upon either DMSO or MG132 10μM treatment for16 hours in ATG5 KO neurons compared to the WT. KO^{DMSO}: 63.27±20.18%; KO^{MG132}: 107.37±40%. pWT^{DMSO} vs pKO^{DMSO} = 0.044, pWT^{MG132} vs pKO^{MG132} = 0.358. Protein levels in KO condition were normalized to the WT set to 100%. N=3. (**g**,**h**) Protein levels of phosphorylated S6 ribosomal protein (pS6) from cultured ATG5 KO neurons. Protein levels in the KO were normalized to the WT set to 100%. KO: 40.39±14.04%, p=0.016. p=0.016. N=4. n.s.-non significant. All data shown represent the mean ± SEM from N independent experiments.

Given that BDNF gene expression in ATG5 KO neurons may be dramatically decreased due to impaired retrograde transport and subsequent loss in BDNF/TRKB signaling, we sought to investigate whether the defective neuronal branching can be rescued by boosting BDNF/TRKB signaling. To test this hypothesis, cultured eGFP-expressing WT and ATG5 KO neurons were treated with BDNF for 14 days, and their neuronal branching was analyzed by Sholl analysis (Kononenko et al., 2017b). Indeed, BDNF supply rescued defective neuronal branching in ATG5 KO neurons (**Fig.32a-d**), but did not ameliorate the axonal dystrophy (**Fig.32e**). Interestingly, rescue of neuronal branching in ATG5-deficient neurons was accompanied by the upregulation of pS6 levels (**Fig.32f,g**), suggesting a cause/consequence relation with mTORC1 activation.

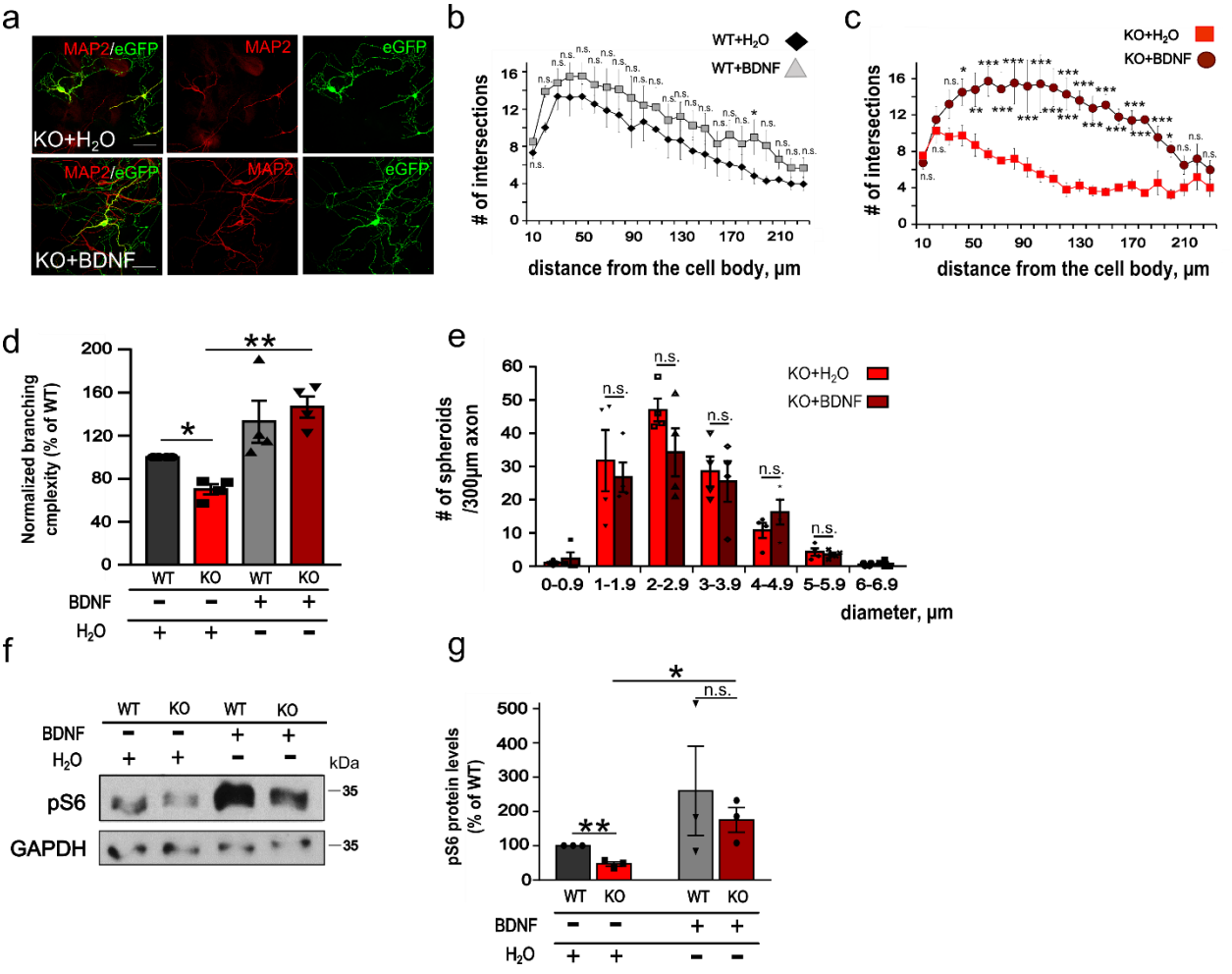

Figure 32. Exogenous administration of BDNF rescues defective branching of ATG5 KO neurons. (**a**) Representative confocal images of ATG5 KO neurons at DIV18 transfected with eGFP (green), stained for MAP2 (red), and either continuously treated with vehicle (H2O) or BDNF (50ng/mL). Sholl analysis of cultured WT (**b**) and ATG5 KO neurons (**c**) either treated with H2O or BDNF. Statistical significance was tested via two-way ANOVA repeated measures. N=4. (**d**) Normalized values from Sholl analysis: KO^{BDNF}:

121.97±9.88, KO^{H_2O}: 57.04±4.72, p=0.001. N=4. In total, 65 WT and 74 KO from N=4. (**e**) Histogram showing the number of axonal swellings in WT and ATG5 KO neurons upon BDNF treatment plotted as a function of their diameter.Statistical significance was tested via two-way ANOVA repeated measures. (**f,g**) pS6 protein levels are significantly increased in lysates of ATG5 KO neurons treated with BDNF (KO: 175.16±36.20%), comparing to H_2O-treated KO controls. KO: 46.61±6.40%. p=0.049. N=3, Protein levels in KO condition were normalized to the WT set to 100%.

4. DISCUSSION

My research data unravel a non-canonical function for LC3 and the autophagy lipidation machinery for the regulation of MT dynamism in neurons. Loss of the LC3-lipid conjugation function results in the accumulation of non-lipidated LC3 in axons, which in turn leads to the retention of the active zone protein ELKS1 and its partner CLASP2. The MT-stabilizing function of CLASP2 may be responsible for impaired MT dynamics within axons and explain the defective trafficking of neurotrophic signals, the accumulation of membranous cargo, and the subsequent formation of axonal swellings (**Fig.33**). However, although defective neurotrophic signaling is causative of reduced neuronal branching, autophagy-deficient neurons show no signs of neuronal death in both, *in vitro* and *in vivo*. In contrast, these data suggest that the loss of neuronal connectivity due to axonal degeneration, but not neuronal apoptosis, may be responsible for the appearance of seizures in ATG5-deficient forebrain excitatory neurons. Here below, these pivotal findings will be extensively discussed.

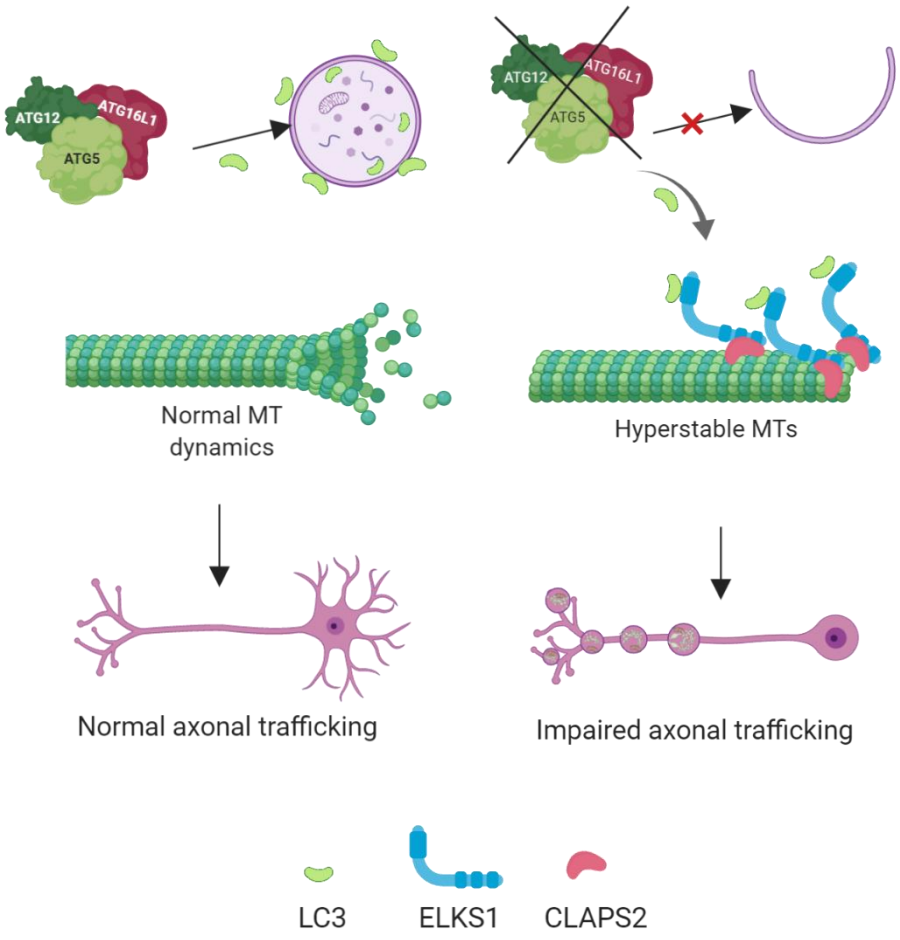

Figure 33. Schematic model illustrating the role of LC3 in MT-based trafficking and axonal homeostasis. Impaired LC3 conjugation and its subsequent accumulation in axons upregulate MT stability via ELKS1-CLASP2 retention in axons, which in turn impairs axonal trafficking of neurotrophic signals and the accumulation of membranous cargo.

4.1 Loss of ATG5 or ATG16L1 in forebrain excitatory neurons does not cause neuronal cell death

Several studies have reported the association between the accumulation of ubiquitin-positive aggregates and neuronal cell death in brain-confined KOs for several core autophagy proteins, including ATG5 (Hara et al., 2006), ATG7 (Komatsu et al., 2006), FIP200 (Liang et al., 2010). Such transgenic mice models revealed neuronal degeneration across brain regions, including the cortex and the hippocampus. Moreover, observed neuronal cell death in autophagy-deficient neurons was suggested to be mediated by apoptosis (Hara et al., 2006; Liang et al., 2010). Surprisingly, our *in vivo* data from *Atg5*$^{flox/flox}$:*CamkIIα*-Cre and *Atg16L1*$^{flox/flox}$;*CamkIIα*-Cre models, revealed no apparent signs of apoptosis in cortiohippocampal neurons, where most of the CamKIIα-expressing neurons are located. Similarly, cultured corticohippocampal neurons lacking ATG5 and ATG16 did not show apoptosis as well. The first noticeable difference between our work and other publications is the utilization of different promoters. In the prior studies, Cre recombinase was expressed under the Nestin promoter, which is mostly expressed in neural stem and progenitor cells (NSCs and NPC, respectively), which further differentiate to both neurons and glia (Hendrickson et al., 2011; Shimada et al., 2012). Thus, the cellular populations affected, as well as the time when each promoter starts to induce the Cre-recombinase expression, are two crucial aspects to take into account. Calcium/calmodulin-dependent protein kinase II alpha subunit (CamKIIα)-expressing neurons represent up to 70% of granule and pyramidal neurons of the hippocampus, and 10-35% of pyramidal neurons in the cortex (Tsien et al., 1996; Wang et al., 2013b). On the other hand, Nestin, an intermediate filament protein, is mostly expressed in NSCs and NPCs, and afterward replaced by the expression of cell-specific intermediate filaments during the differentiation to neurons or glia (Hendrickson et al., 2011). Interestingly, whereas the Nestin promoter is active during early embryonical stages (E7.75) (Dahlstrand et al., 1995; Mignone et al., 2004), CamKIIα promoter has been shown to be activated several days after birth (Burgin et al., 1990), when some fundamental neural circuits are already established (Farhy-Tselnicker and Allen, 2018). Thus, whereas the Nestin promoter affects most of the neuronal and glial populations during early embryogenesis, CamKIIα-activated promoter is mostly found in

differentiated forebrain excitatory neurons from postnatal stages. In addition, it has been previously reported that NSCs undergo apoptosis by the loss of autophagy (Xi et al., 2016; Yazdankhah et al., 2014). Hence, it remains unclear whether the reported neurodegeneration under the Nestin promoter in autophagy-deficient neurons could be also due to deficient NSCs proliferation and subsequent apoptosis. Apart from neurons, NSCs also generate glia populations, including astrocytes and oligodendrocytes (Hendrickson et al., 2011). Both mentioned above glial cells are generated in embryonal stages, and assist neurons for their correct development and functioning (Farhy-Tselnicker and Allen, 2018; Le Bras et al., 2005). Thus, it cannot be excluded that Nestin promoter-driven autophagy deficient glia might undergo cell death. In fact, astrocytes have been observed to degrade damaged mitochondria from neighboring neurons by a process termed transmitophagy (Davis et al., 2014).

Alternatively, although no sign of apoptosis could be detected in 13 weeks old KO mice, one could consider whether some CamKIIα-positive ATG5 KO neurons may die at earlier and/or later stage. Ongoing research is trying to decipher that hypothesis, although preliminary data from 3 week-old mice also revealed no sign of apoptosis. On the other hand, although neuronal cell death has been commonly monitored by apoptosis, different mechanisms of cellular death, such as ferroptosis, could be activated in autophagy-deficient mice as well (Galluzzi et al., 2018). Nevertheless, given the fact that no neuronal loss could be observed in either cortical/hippocampal brain areas or cultured neurons from ATG5 and ATG16L1 KO mice, our data indicate that ATG5 and/or ATG16L1-mediated autophagy is dispensable for the survival of forebrain excitatory neurons. Finally, another intriguing scenario suggests that CamKIIα-positive neurons are exceptionally resistant to the lack of autophagy. Indeed, ongoing data in our laboratory indicate a selective loss of specific classes on interneurons in autophagy-deficient brains, but further extensive research is needed to define whether autophagy has a particular role in different neuronal subtypes (current research of Dr. de Bruyckere in our laboratory).

4.2 Forebrain excitatory neurons lacking ATG5 display axonal degeneration, accompanied by weight reduction and epileptic seizures in KO mice

Axonal degeneration is an early hallmark of several neurodegenerative diseases, such as Alzheimer's disease, Amyotrophic lateral sclerosis, and Parkinson's disease (Lee et al., 2011; Salvadores et al., 2017). This phenotype is typically characterized by a dying-back mechanism, in which axons from the synaptic regions gradually degenerate toward the cell body (Wang et al.,

2012). ATG5 KO neurons revealed axonal pathology characterized by the formation of spheroids in axons, but not in dendrites. These data are consistent with previous reports for Nestin-driven KOs of ATG5 (Hara et al., 2006), ATG7 (Komatsu et al., 2006), and WIPI4 (Zhao et al., 2015) in mice. In contrast, although Nestin-driven KOs for FIP200 (Liang et al., 2010) and ATG9A (Yamaguchi et al., 2018) also revealed axonal pathology, this axonal pathology was characterized by progressive spongiosis, which consists in the clustering of vacuoles, a typical feature of prion diseases (Soto and Satani, 2011). Here in this thesis, axonal pathology was identified in cortical motor neurons of ATG5 KO mice projecting to ventral thalamic nuclei. Interestingly, posterior/ventral nuclei were the unique areas with apparent neuronal loss, although the thalamus has no CamKIIα-expressing neurons. Thus, this data suggests that axonal pathology in ATG5-deficient mice may interfere with the proper connectivity of the cortex with the thalamus, which in turn may mediate the degeneration of selective brain areas. However, a deeper anatomical and electrophysiological study will be required to verify impaired connectivity between these two areas.

Why ATG5 KO mice are leaner and reveal reduced weight gain? Current research is focusing on answering that question. Although ATG5 KO mice are smaller than the WT littermates, magnetic resonance imaging (MRI) measurements did not reveal changes in fat, lean, and total water content when compared to body weight (data not shown). Thus, this data may point to retardation in whole-body development. To further investigate this phenotype, ATG5 KO mice will be analyzed by PhenoMaster, a metabolic cage which measures the energy consumption, the amount of food and water consumed, and the distance that they move within the cage. Despite the data acquired so far, the cause for the reduction of weight gain remains intriguing. Even though the neuronal loss is detected in the thalamus, this area is not known to control energy homeostasis in mice (Price and Drevets, 2010). In contrast, the hypothalamus is reported to mediate the endocrine function, including the homeostasis of growth hormones (Janowski et al., 1993). Since forebrain cortical areas have been shown to project to the hypothalamus and integrate endocrine functions (Saper, 2000), it would be interesting to study the cortical/hypothalamic connectivity in mice lacking autophagy in forebrain excitatory neurons.

On the other hand, autophagy-deficient mouse models studied here displayed epileptic seizures, followed by compromised viability. In fact, it is reported that neurons with CamKIIα activity prevent epilepsy in mice (Perlin et al., 1992), whereas inhibition of CamKII activity induces hyperexcitability (Ashpole et al., 2012). Thus, whether unbalance of excitatory/inhibitory inputs is dysregulated, and triggers epileptic seizures in CamKIIα-positive ATG5 KO neurons, is currently

being studied. Interestingly, we have also generated ATG5 KO mice under the vesicular GABA transporter (VGAT) promoter, which targets inhibitory neurons within the whole brain. Surprisingly, these mice do not display seizures, further suggesting a selective role for ATG5 in defined populations of neurons in the brain.

4.3 Impaired LC3 lipid conjugation and subsequent accumulation of non-lipidated LC3 is responsible for selective axonal pathology

ATG5-deficient forebrain excitatory neurons exhibited the formation of axonal swellings, a phenotype which was reproducible in ATG5 and ATG16L1 KO cortical/hippocampal cultured neurons. Intriguingly, only 25-30% of cultured neurons showed axonal pathology in ATG5 and ATG16L1 KO neurons. Cultured neurons contain different neuronal populations, and it is likely that they respond differently to the lack of ATG5 or ATG16L1. Moreover, unequal autophagy responses have also been observed by fasting or upon bafilomycinA1 treatment in different brain regions (Nikoletopoulou et al., 2017). Thus, the presence of axonal pathology in a fraction of all cultured neurons may be due to a specific axonal sensitivity for some certain neuronal types. Future studies will elucidate which neuronal populations are more sensitive to axonal pathology.

In this thesis, axonal pathology was only observed in neurons with impaired LC3 processing or conjugation to autophagosomes, whereas knockdown of genes implicated in autophagy initiation, such as FIP200 and ULK1, did not reveal spheroids. These data contrast with previously reported Nestin-driven KO mouse models for FIP200 and ATG9A, another protein not directly involved in LC3 lipid conjugation, which displayed axonal spheroids in the brain (Liang et al., 2010; Yamaguchi et al., 2018). Nevertheless, FIP200 and ATG9A KO brains were observed to generate axonal swellings by the selective accumulation of vacuoles (also termed spongiosis), a phenotype which was not reported neither in ATG5 nor ATG7 KO mice (Hara et al., 2006; Komatsu et al., 2006), nor in this thesis. Collectively, these data further suggest that impaired LC3 lipidation causes axonal pathology in neurons by a different mechanism reported in FIP200 and ATG9 KO mice.

Our data unravel a mechanism by which the accumulation of non-lipidated LC3 in axons and presynaptic terminals causes the formation of axonal swellings. Although non-lipidated LC3 levels were significantly increased by 50% and 25% in ATG5 and ATG16L1 KO cultured neurons, respectively, no significant upregulation was observed in ATG5 KO brain lysates. This is due to the fact that CamKIIα-positive neurons represent a small neuronal fraction when compared to the

rest of neuronal and glial cells in the cortex, thus masking the KO effect. Accumulation of LC3I was also published for Nestin-driven WIPI4 KO, which in line with our results, reported a massive formation of axonal swellings in neurons (Zhao et al., 2015). WIPIs are a family of proteins which bridge the phosphatidylinositol 3-phosphate generated in the forming phagophore with other core autophagy proteins (Menzies et al., 2017). This is the case of WIPI2, which recruits ATG16L1 to the phagophore for the LC3 lipidation (Polson et al., 2010). The function of WIPI4 is not well-known, and it is reported to act downstream and upstream of LC3 lipidation (Bakula et al., 2017; Lu et al., 2011). Importantly, this thesis demonstrated that modulation of non-lipidated LC3, via both LC3G120A overexpression or LC3A/B KD, enhanced or rescued the formation of axonal swellings, respectively. Moreover, presumable non-lipidated LC3 was found to accumulate in axonal swellings of ATG5 KO neurons, which disappeared from spheroids upon LC3B KD.

Maday and Holzbaur (2014) reported that autophagy biogenesis in axons mostly occurs in the distal parts of the neurite. Moreover, they also showed that autophagy biogenesis in distal tips of hippocampal neurons isolated from GFP-LC3B transgenic mice (Mizushima et al., 2004) has a rate of around 1 event every 8 minutes. These transgenic mice cells are characterized by a substantial accumulation of non-lipidated GFP-LC3, which has been shown to reveal much slower lipidation dynamics comparing to the endogenous LC3 (Ni et al., 2011). This raises the question of whether GFP-LC3 transgenic mice display the neurodegeneration or axonal pathology as well (Mizushima et al., 2004)(Katsumata et al., 2010)(Maday and Holzbaur, 2014). Currently, this question is being addressed in our laboratory. In support of our hypothesis, our preliminary data indicate that the overexpression of tagRFP-proLC3 itself causes axonal swellings comparing to an empty GFP construct. However, future experiments are needed to elucidate this hypothesis in details.

4.4 Is there defective degradation of membranous organelles in axons with impaired LC3 conjugation machinery?

Defective protein degradation and accumulation of p62- and UB-positive inclusions have been extensively reported in cells lacking autophagy, including neurons (Mizushima and Levine, 2010)(Hara et al., 2006). Our data reported here are in line with previous reports and show that neurons lacking either ATG5 or ATG16L1 accumulate p62- and UB-positive puncta in the soma. However, these protein inclusion bodies were not found in axonal swellings, indicating that, indeed, axonal swellings may not result from defective protein clearance, as previously suggested

(Komatsu et al., 2007a). Furthermore, although some previous *in vivo* studies reported p62- and UB-positive puncta within spheroids, these puncta only appeared occasionally, and not in all axonal swellings (Komatsu et al., 2007b; Nishiyama et al., 2007; Zhao et al., 2015). Thus, it appears that defective protein clearance is not the leading cause for the formation of axonal swellings in LC3 lipidation-deficient neurons.

Accumulation of aberrant membranous structures has been previously reported in brain-confined KOs for ATG5 (Nishiyama et al., 2007) and ATG7 (Komatsu et al., 2007b). Accordingly, enormous multilamellar structures were found within the soma of ATG5 cultured neurons. Although the nature of such structures in neurons remains elusive, this phenotype has also been reported in liver cells defective for ATG7 (Komatsu et al., 2005). In this thesis, axonal swellings also revealed the accumulation of membranous structures, including mitochondria, late endosomes, and ER-like tubular structures. Whereas the first two organelles are known to be trafficked along the axon, little is known about the expansion of the ER within autophagy-deficient axons (Gurel et al., 2014). In fact, in the last years, axonal ER functions have started to emerge, including the biosynthesis of lipids, transport of mRNAs and proteins, calcium dynamics, and the regulation of other membrane organelles (Luarte et al., 2018). Here in this thesis, the accumulation of massive amounts of tubular ER is reported. Identification of such structures could only be observed by the electron microscopy (Ivankovic et al., 2019; Wu et al., 2017), since immunostainings for the common ER marker proteins such as disulfide isomerase (PDI) (Hewett et al., 2000; Merianda et al., 2009) and the targeting sequence KDEL (Valdes et al., 2012) failed to localize in axonal swellings. Despite that, future experiments may identify these ER structures by using other commonly reported markers such as reticulons (i.e., reticulon-4) (Farias et al., 2019). Importantly, this thesis raises some questions about why tubular ER-like structures accumulate in axonal swellings from ATG5-deficient neurons: (1) Given that ER serves as a platform to generate autophagosomes (Uemura et al., 2014), are pre-autophagic structures accumulating due to deficient maturation of phagophores when LC3-lipidation machinery is impaired? (2) Is ER degradation defective? (3) Or maybe ER trafficking is altered?

Regarding the first question, published ultrastructural studies in ATG5 KO MEF cells reported the presence of pre-autophagic structures unable to properly enclose, followed by subsequent enlargement and formation of whorl-like structures (see figure 34) (Kishi-Itakura et al., 2014; Sou et al., 2008). However, these structures do not really match with ER structures found in this thesis, which instead resemble the tubular ER (Ivankovic et al., 2019; Wu et al., 2017). Indeed, preliminary data from the lab have revealed no enrichment of pre-autophagic markers such as

FIP200, WIPI2, ATG9A, or ATG13 (Kishi-Itakura et al., 2014), thus suggesting that immature phagophores do not massively accumulate within spheroids of LC3 conjugation-deficient neurons.

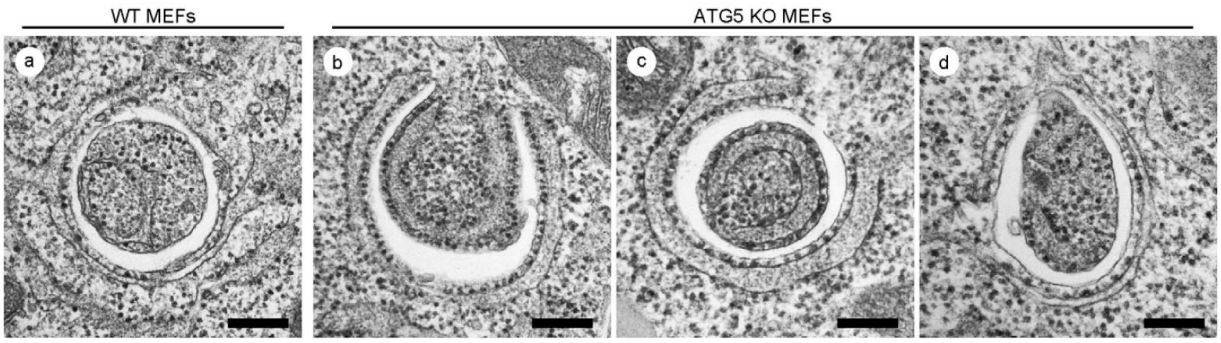

Figure 34. Electron micrographs of isolation membranes formed in WT (**a**) **or ATG5 KO MEFs** (**b-d**)**.** The figure is taken from Kishi-Itakura et al. (2014).

Second, tubular ER accumulations might result from their defective degradation via autophagy. This process, also called ER-phagy, is shown to be independent of either ubiquitination or p62, and instead require ER-resident receptors that bind to LC3/GABARAPs, such as FAM134B (Khaminets et al., 2015; Mochida et al., 2015). In line with this hypothesis, Ivankovic et al. (2019) reported that neurons deficient for the adaptor protein-4 (AP-4) reveal the missorting of ATG9A-positive vesicles (involved in the transport of core ATG proteins) into axons, with subsequent autophagy flux retardation and generation of axonal swellings containing tubular ER. Interestingly, in this publication, they also revealed that both WT and AP-4 KO axons develop spheroids during axonal growth. Moreover, although both conditions led to the accumulation of tubular ER, WT spheroids disappeared after a few minutes, whereas KOs spheroids persisted during a few hours. In addition, autophagosomes could be observed engulfing ER in the KO condition, but no sign of pre- or mature autophagosomes were showed in WT axonal swellings. Thus, although autophagy is suggested to be involved in the degradation of ER in axonal swellings, it remains elusive whether impaired ER-phagy is the cause of enhanced accumulation of ER, or rather autophagosomes are recruited to axonal swellings as a consequence of impaired ER homeostasis. Hence, the third question arises, is there impaired ER trafficking along the axons with defective LC3 conjugation machinery?

Little is known about the trafficking of ER in cells, and less in polarized structures like axons. There is evidence that ER can be transported along MTs through two mechanisms: via motor protein-dependent transport, and via EB1-dependent dragging during the MT polymerization

(Friedman et al., 2010; Gurel et al., 2014; Waterman-Storer and Salmon, 1998). In this thesis, MT motor movements and MT polymerization events are reduced in both ATG5 and ATG16L1 KO axons, suggesting a possible impairment in the ER trafficking. However, more fundamental understanding of ER trafficking in axons is needed to highlight the interconnection between ER trafficking and MT dynamics. Examples of MT and ER links are found in some cases of hereditary spastic paraplegia (HSP), where mutations in different proteins, such as the two MT-binding proteins, REEP1 (Beetz et al., 2013) and spastin (Park et al., 2010), are found to dysregulate ER homeostasis in neurons. Interestingly, mutations of spastin results in the loss of its MT-severing function, which causes reduced MT-dynamics, impaired axonal trafficking, and formation of axonal swellings (Fassier et al., 2013). Taken together, all these cumulative evidence, followed by the results of this thesis, suggest a succulent interconnection among autophagy, MT dynamics, and ER homeostasis.

On the other hand, this thesis also showed the accumulation of mitochondria and late endosomes in spheroids of ATG5-deficient neurons. Mitochondria were to found to be slowly trafficked along axons, and appeared to be more accumulated in axonal swellings. Whether mitophagy is impaired in LC3 lipidation-deficient neurons cannot be ruled out from these data. It is commonly reported that damaged mitochondria undergo mitophagy via Parkin- and p62- mediated mitophagy, although this process is flexible and may not always require these two proteins (Palikaras et al., 2018). Ongoing research is investigating whether mitochondria are functional in ATG5 and ATG16L1 KO neurons. Studies using brain-confined deletion of ATG5 and ATG7 did not report mitochondria damage (Komatsu et al., 2007b; Nishiyama et al., 2007), although it was observed in FIP200 KO mice (Liang et al., 2010). These differences among published data may result from the reported action of ATG5/ATG7-independent alternative autophagy, which is dependent on ULK1/2 and FIP200 (Nishida et al., 2016). Alternatively, mitochondria can be degraded via endosomal invagination and fusion to lysosomes, a process, which is mediated by the ESCRT complex and requires the Beclin1 (Hammerling et al., 2017; Tekirdag and Cuervo, 2018).

4.5 Non-lipidated LC3 stabilizes ELKS1-CLAPS2 at the presynapse and causes the hyperstabilization of MTs

Here we report that the regulation of MT stability in axons is promoted by the action of a protein complex comprising the scaffolding active zone ELKS1 and the MT-stabilizing CLASP2. CLASP2 is the brain-enriched member of the CLASPs family (Akhmanova et al., 2001), known to play roles

during neuronal polarity, synaptic function, and brain development (Beffert et al., 2012; Dillon et al., 2017). In agreement with data from HeLa cells (Lansbergen et al., 2006), CLASP2 function in MT stabilization in ATG5 KO axons was found to require its interaction with ELKS1. In addition, this work suggests that ELKS1-CLAPS2 complex is stabilized in axonal swellings via ELKS1 interaction with non-lipidated LC3. Several lines of evidence support this hypothesis. First, we demonstrated that LC3 directly associates with ELKS1 *in vitro* (**Fig.26**). Second, levels of ELKS1 were found upregulated in ATG5 KO axonal swellings (**Fig.28c**) and were decreased in LC3 KD condition (**Fig. 30a,b**). Finally, downregulation of ELKS1 levels in ATG5 KO neurons rescued impaired MT-dynamics and diminish axonal pathology (**Fig.30g-k**). Furthermore, data from another PhD student in the lab have revealed that ELKS1 and LC3 form a complex in the mouse brain. On the other hand, this thesis also showed that CLASP2 levels are upregulated in brains of ATG5 KO mice. Moreover, CLASP2 levels were found slightly but significantly decreased in axonal swellings upon ELKS1 KD in ATG5 KO neurons. Collectively, data presented here, taken together with previous reports indicating the MT-stabilizing action of ELKSs-CLASPs interaction in cells (Lansbergen et al., 2006), suggest that ELKS1-CLASP2 function may be directly involved in the hyperstabilization of axonal MTs in ATG5 KO neurons. Current experiments are focusing on the analysis of MT-dynamics upon CLASP2 overexpression or downregulation in neurons. Interestingly, upregulation of CLASP2 levels in cultured neurons was reported to alter neuronal morphology and increased presynaptic terminal circumference (Beffert et al., 2012).

ELKS proteins are known to mediate the exocytosis of synaptic vesicles in presynaptic terminals, and ELKS KO reduces Ca^{+2} influx and neurotransmitter release in neurons (Held and Kaeser, 2018; Liu et al., 2014). Our data indicated that increased ELKS1 levels in axonal swellings and presynaptic terminals do not impair the exocytosis of synaptic vesicles, suggesting a regular synaptic activity of ATG5 KO neurons. However, the physiological role of LC3-ELKS interaction in WT neurons is enigmatic. ELKS was initially identified as a RAB6 interacting protein mediating the endosome-to-Golgi dependent transport (Monier et al., 2002), a pathway also involving the intra-Golgi and Golgi-to-ER retrograde transport (White et al., 1999)(Held and Kaeser, 2018). Although no published work currently connects autophagy and RAB6-positive vesicles, the involvement of RAB6-dependent trafficking in the delivery of catalytic hydrolases to lysosomes has been published in *D. melanogaster* (Ayala et al., 2018). Alternatively, LC3-ELKS1 binding could control autophagosomes at presynaptic sites. Indeed, another scaffolding protein, Bassoon, known to interact with ELKS, has been reported to sequester ATG5 and inhibit autophagy at presynaptic sites (Okerlund et al., 2017). How LC3 and ELKS regulate autophagy and axonal trafficking along the axon in physiological conditions will require more research. However, here in

this thesis, we suggest a model by which autophagy lipidation machinery regulates MT dynamics for the correct trafficking of autophagosomes from presynaptic sites.

In line with upregulated CLASP2 levels and defective MT dynamics, analysis of the PTM of tubulin revealed a shift to stabilized MTs in LC3 lipidation-deficient neurons. This phenotype was characterized by increased levels of detyrosinated, Δ2, and acetylated α-tubulins in KO neurons, levels of which correlate with stable MTs. Interestingly, the levels of tyrosinated α-tubulin, which are found in labile MTs, were decreased upon ATG5 and ATG16L1 KO in neurons. This phenotype was further demonstrated by increased resistance of ATG5 KO neurons to nocodazole treatment, a MT depolymerizing drug. In fact, there are several publications reporting that bidirectional imbalance between dynamic and stable MTs hallmarks several neurodegenerative diseases (Dubey et al., 2016; Tarrade et al., 2006). Interestingly, autophagy induction is shown to promote MT stability and avoid a dramatic retraction of axons upon spinal cord injury (He et al., 2016). This function of autophagy in stabilizing MTs is consistent with the hypothesis that LC3-ELKS-CLASP2 may stabilize MTs to facilitate the trafficking of autophagosomes in physiological conditions.

4.6 Reduced neurotrophic signaling matches defective neuronal branching in ATG5 deficient neurons

Data coming from our laboratory indicate that ATG5 deficient neurons have impaired neuronal complexity, presumably due to defective trafficking of BDNF/TRKB-positive vesicles (Kononenko et al., 2017b). In agreement with prior results, this thesis showed that ATG5 KO neurons suffer from impaired trafficking of TRKB-positive vesicles in axons, decreased BDNF/TRKB signaling, and subsequent loss of BDNF expression in ATG5 KO neurons. Similarly, mouse models for Huntington disease (Gauthier et al., 2004) and Alzheimer disease (Poon et al., 2011) reported that impaired neurotrophic signaling in the axon is sufficient to affect the rest of the cell and cause neurodegeneration (Gauthier et al., 2004). In addition, mRNA levels of BDNF were severely decreased. It is known that BDNF expression is regulated via a positive feedback system dependent on TRKB signaling, concretely through the MAPK pathway (ERK1/2) (Tuvikene et al., 2016). Moreover, this positive feedback loop is reported to regulate the paracrine stimulation of neighboring neurons *in vitro* (Lindholm et al., 1996) and *in vivo* (Wang et al., 2015). Given that both ERK1/2 activation and BDNF expression are downregulated, these data suggest that the positive feedback system is lost in ATG5 KO neurons.

This thesis also reports that the total levels of TRKB are found downregulated in ATG5 KO cultured neurons, which could also explain why downstream TRKB signaling is reduced. Interestingly, levels of total TRKB could be rescued upon inhibition of the proteasome activity by MG132. It is published that TRK receptors, including the TRKB, are ubiquitinated to facilitate their internalization into RAB7-positive endosomes and their subsequent lysosomal degradation. Importantly, UB-dependent internalization of TRKB was also showed to decrease the viability of BDNF-dependent primary neurons (Murray et al., 2019). Other reports have indicated that p62 serves as a shuttling protein for the interaction of TRKA receptors and the proteasome, which promote the de-ubiquitination of TRKA-internalized proteins prior to degradation by lysosomes (Geetha et al., 2008; Geetha and Wooten, 2008). Collectively, plausible hypothesis would suggest that there is either an increased TRKB UB-dependent internalization or/and increased p62-dependent de-ubiquitination and subsequent lysosomal degradation of TRKB. However, further research is required to elucidate the mechanism by which proteasome inhibition rescue TRKB receptors in ATG5 KO neurons.

On the other hand, impaired neuronal complexity could be rescued by the exogenous supply of BDNF, although axonal pathology was not improved. In fact, TRKB receptors are expressed throughout the plasma membrane, including the soma (Haapasalo et al., 2002). Thus, the effect observed upon BDNF application to cultured neurons may occur through receptors located on the soma or other areas of neurites, thus circumventing the long-distance trafficking in the axon. In contrast with our data, Ivankovic et al. (2019) reported no alterations of neuronal branching in AP4 KO neurons with impaired ATG9A trafficking. Although neurons displayed a similar phenotype of axonal pathology and accumulation of tubular ER, autophagy was not completely blocked in this model, suggesting a possible milder phenotype compared to our model.

BDNF neurotrophic signaling is known to strengthen synapses, modulate synaptic plasticity, and induce long-term potentiation for memory consolidation (Bekinschtein et al., 2008; Nagahara and Tuszynski, 2011), which is also reported to depend on local protein synthesis via mTORC1 activation (Slipczuk et al., 2009; Takei et al., 2004). This thesis revealed that mTORC1 activity is downregulated in ATG5 KO neurons, which is rescued to WT levels upon BDNF supply. Given the role of proper axonal trafficking (Wang et al., 2013a) and BDNF signaling in memory consolidation, one could speculate whether memory acquisition is impaired in LC3 lipidation-deficient mice. Currently, another PhD student is investigating this hypothesis. In conclusion, this thesis reveals a decreased MT dynamics and subsequent dysfunction of retrograde neurotrophic signals in axons with impaired LC3 conjugation machinery.

5. CONCLUDING REMARKS AND DIRECTIONS FOR FUTURE WORK

The work performed in the frame of this doctoral dissertation aimed: (I) to investigate whether the selective loss of autophagy in forebrain excitatory neurons is detrimental for the brain function of mice; (II) to decipher the molecular and cellular mechanism leading to axonal pathology in autophagy-deficient neurons; (III) to characterize the link between autophagy and the neurotrophic signaling. Throughout my research, the following key findings have been revealed:

1. Selective loss of ATG5 or ATG16 in forebrain excitatory neurons is not causative of either apoptosis or neuronal death in the cortex and the hippocampus, although it is responsible for a gradual loss of weight and the manifestation of seizures in mice. These results contrast with previously published neuronal death in brain-confined KOs for several autophagy genes (Hara et al., 2006; Komatsu et al., 2006; Zhao et al., 2015). Indeed, my work invites to reconsider the utilization of the nestin promoter for the specific study of neurons, since nestin-driven KOs may also affect the function of NSCs, astrocytes, and oligodendrocytes, and thus explain the more severe phenotype. On the other hand, these data also suggest that distinct neuronal populations may have a different vulnerability to the lack of autophagy. Hence, interesting future research may elucidate whether some neuronal subtypes are more vulnerable to the lack of autophagy and whether indeed this could be relatedto some neurodegenerative diseases.

2. Loss of core autophagy machinery involved in the LC3 lipid conjugation and processing causes the formation of axonal swellings in neurons*in vitro* and *in vivo*. This is revealed to be dependent on LC3 since (a) LC3I is upregulated and accumulates in axonal swellings; (b) overexpression of a LC3 lipidation-deficient mutant in WT neurons causes axonal pathology; (c) knockdown of LC3 improves axonal shape by reducing the size of spheroids; and (d) impaired function of ATG proteins involve in LC3 conjugation lead to the defective axonal morphology, a phenotype not observed in deficient ATG proteins involved in autophagy induction. This data is in agreement with previously suggested that FIP200, ATG9A, and ULK1/2 KOs display a distinct axonal pathology when compared to ATG5 and ATG7 KOs (Hara et al., 2006; Joo et al., 2016; Komatsu et al., 2006; Liang et al., 2010; Yamaguchi et al., 2018).

3. My research further indicates that axonal swellings are not a result of defective protein clearance, but rather a consequence of defective axonal trafficking due to MT hyperstability in LC3 lipidation-deficient neurons. PTMs of tubulin highlighted the presence

increased stable MTs, which was followed by decreased EB3-dependent polymerization dynamics in ATG5 and ATG16L1-deficient neurons. Moreover, MT-based trafficking machinery was found to accumulate within spheroids, a phenotype accompanied by defective trafficking of mitochondria and TRKB-positive vesicles. Intriguingly, my results are not sufficient to elucidate whether LC3 lipidation-deficient neurons may suffer from defective degradation of membranous organelles. In fact, a massive accumulation of tubular ER is observed within spheroids, suggesting a connection between autophagy, ER, and axonal degeneration,an exciting topic to be addressed in the future.

4. Non-lipidated LC3 regulates MT stability at synapses via modifying the abundance of the active zone protein ELKS1 and the MT stabilizing protein CLAPS2. Both ELKS1 and CLASP2 are known to associate in non-neuronal cells and mediate the stabilization of MTs (Lansbergen et al., 2006). Moreover, my data not only shows that ELKS1 and CLASP2 are upregulated in ATG5 KO neurons but also reveals a direct association between LC3A/B and ELKS1. Interestingly, knockdown of ELKS1 was sufficient to rescue MT dynamics and reduce axonal pathology in ATG5 KO neurons. Hence, taken together with all these results, I strongly suggest in a model where impairment of LC3 lipidation to autophagosomes drives its accumulation in axons, accompanied by the retention of ELKS1 and CLAPS2, which subsequently hyperstabilze MTs and alters the axonal trafficking. To further demonstrate this model, current research is investigating the association of LC3-ELKS1-CLAPS2 complex in neurons, and the potential alterations in MT dynamics upon modulation of CLASP2 levels.

5. Finally, this thesis exemplifies the consequences of impaired axonal trafficking by the reduced velocity of TRKB-positive vesicles in ATG5 KO neurons. A phenotype which is accompanied by decreased TRKB levels and its downstream signaling, including the expression of BDNF. Indeed, these data suggest that impaired axonal arborization of neurons is caused by the loss of TRKB-BDNF signaling in ATG5 KO neurons. Despite these new results, it remains unclear how levels of total TRKB are reduced in ATG5 KO neurons. Moreover, given the fact that BDNF-TRKB signaling is involved in the modulation of synaptic plasticity and strengthening of synaptic activities, it would be interesting to study whether this phenotype could impair the connectivity between brain areas and be responsible for the seizures found in ATG5 KO mice.

6. MATERIALS AND METHODS

6.1 Materials

6.1.1 General laboratory equipment

Instrument	Manufacturer	Identifier
Cabinet, Horizontal laminar flow	Thermo Fisher Scientific	Heraguard ECO
Cabinet, Vertical laminar flow cabinet **(cell lines)**	Scanlaf	Mars Safety Class 2
Cabinet, vertical laminar flow **(primary cells)**	Thermo Fisher Scientific	Safe 2020
Centrifuges	Eppendorf Hettich VWR	5702R 320R MicroSTAR 17R
Electrophoresis Power Source	VWR	300V
Electrophoresis chamber **(PCR)**	VWR	700-0569
Electrophoresis chamber **(WB)**	Bio-Rad	Mini-Protean Tetra Cell
Dissection tools Forceps Scissors Scalpel	FST	 11253-27 16020-14 11270-20 14090-09 13002-10 14002-13 10073-14
Freezer **(-20°C)**	LIEBHERR	9988187-12
Fridge **(4°C)**	LIEBHERR	9983491-10
Gel imager system (PCRs)	Bio-Rad	Gel Doc™ XR+
Incubator CO_2 **(cell lines)**	Binder	C170
Incubator CO_2**(primary neurons)**	Eppendorf	Galaxy 1705
Incubator Shaker	Eppendorf	M1335-0002
Microscope, inverted **(cell culture)**	Leica	Leica DMi1
Microscope, inverted fluorescence **Camera** **Temperature module** **LED Light source** **Software** **Objectives:** **40x/1.4 oil DIC** **63x/1.4 oil** **10x/0.3**	Zeiss Hamamatsu Zeiss CoolLED Micro-Manager Zeiss Zeiss Zeiss	Axiovert 200M C11440 TempMoudleS pE-4000 MicroManager1.4 420762-9900 420780-9900 420304-9901

Microscope, inverted confocal **Camera** **Detector** **Software** **Objectives:** **40x/0.85** **63x/1.20**	Leica Leica Leica Leica Leica Leica	TCS SP8 HyVolution 2 4 HyD's, 1 PMT LAS X Apo CORR CS PL APO W motCORR CS2
Microscope, light **(histoscanner)** **Software**	Leica Leica	SCN400 Digital Image Hub
Microscope, stereo **(dissection)**	Leica	Leica M80
Microscope, transmission electron **Camera** **Software**	Jeolusa Gatan Gatan	JEM-2100 Plus OneView 4K 16 bit DigitalMicrograph
Microtom	Thermo Fisher Scientific	Microm HM 430
Microwave	Inverter	Sharp
Neubauer chamber	Marienfeld	0640110
Osmometer	Gonotec	Osmomat 3000
Perfusion pump	WPI	Peri-Star Pro
pH-meter	Mettler Toledo	Seven Easy
Photometer	Eppendorf	Bio Photomer plus
Real-time PCR Thermocyler	Applied Biosciences	7500 RealTimePCR System
Sonicator	BRANSON	Sonifier 250
Scales	OHAUS VWR	EX225D T1502746
Thermocycler	VWR	peqSTAR
Thermoschaker	CellMedia	Thermomixer basic
Water bath	VWR	VWB6
Vortex	Scientific Industries	Vortex-Genie 2

6.1.2 Chemicals

Chemical	Manufacturer	Identifier
2-ß-Mercaptoethanol	Roth	4227.1
2-Propanol	Roth	CP41.3
Acetic acid 100%	Roth	3738.4
Acetone	Roth	5025.1
Ammonium chloride	Roth	K298.2

Ammonium peroxidisulfate (APS)	Merck	1.012.001.000
Ampicillin sodium salt	Roth	K029.2
Boric acid	VWR	J67202
Bovine Serum Albumin	Sigma	A7906
Bromophenol blue	Sigma	B5525
Calcium chloride dihydrate	Roth	5239.2
Calcium chloride hexahydrate	Roth	T886.1
Cresyl violet acetate	Sigma	C5042
D-(+)-Glucose	Sigma	G5767
D-Manitol	Sigma	M4125
Digitonin	Roth	4005.1
Dimethyl sulfoxide (DMSO)	Roth	A994.2
di-Potassium hydrogenphoshate	Roth	6875.1
di-Sodium hydrogen phosphate dihydrate	Roth	4984.1
di-Sodium hydrogen phosphate anhydrous	Merck	106559
EDTA	AppliChem	A1104.1000
EGTA	Roth	3054.2
Ethanol	Omnilabs	A1613.2500PE
Gelatin from porcine skin	Sigma	G2500
Glycerol	Roth	7530.1
Glycine	Roth	3908.3
HEPES	Sigma	H4034
Hydrochloric acide 32%	Roth	X896.2
IGEPAL	Sigma	I8896
Kanamycinsulfat	Roth	T832
LB-Agar (Lennox)	Roth	X965.2
LB-Medium (Lennox)	Roth	X964.2
Luminol	Roth	4203.1
Magnesium chloride hexahydrate	Roth	2189.1
Magnesium sulphate heptahydrate	Roth	P027.2
Methanol	Roth	4627.5
Milk powder	Roth	T145.2
Normal Goat Serum (NGS)	Thermo Fisher Sci	16210064
Paraformaldehyde (PFA)	Merck	104.005.100
p-coumaric acid	Sigma	C9008
Phenol red	Sigma	P3532
PIPES	Sigma	P8203
Ponceau S	Roth	5938.1
Potassium acetate	Roth	T874.1
Potassium chloride	Roth	6781.1
Potassium dihydrogen phosphate	Roth	3904.1
Potassium disulfite	Sigma	60508
Potassium hypochlorid	Carl Roth	9062.3

Saponin	Serva	34655
Sodium chloride	Roth	3957.1
Sodium hydrogen carbonate	Roth	6885.1
Sodium hydroxide	Roth	6771.1
Sodium dodecyl sulfate (SDS) ultra-pure	Roth	2326.2
Sodium tetraborate	VWR	1303964
Sucrose	Sigma	S0389
Tetramethylenediamine (TEMED)	AppliChem	A1148.0028
Tris (hydrogenmethyl) aminomethane (Tris-base)	VWR	28.808.294
Trizma hydrochloride (Tris-HCl)	Sigma	T3253
Trypan blue	Roth	CN76.1
Tween 20	VWR	663684B

6.1.3 Reagents

6.1.3.1 Reagents for molecular biology

Reagent	Manufacturer	Identifier
Acryl/Bis™ solution (30%) 37.5:1	VWR	E347
Bradford Reagent	Sigma	B6916
Complete Mini Protease Inhibitor	Roche	11836153001
DNA ladder (100 bp/ 1 kb)	Thermo Fisher Sci	SM0323/SM0311
DNA Gel Loading Dye (6X)	Thermo Fisher Sci	R0611
DreamTaq DNA polymerase	Thermo Fisher Sci	EP0703
ECL™ WB detection reagents	GE Healthcare	RPN2106
LongAmp Taq DNA polymerase	BioLabs	M03235
Normal Goat Serum	Gibco	16210064
Nuclease-free water	Ambion	AM9938
PageRuler Plus Prestained Prot. Ladder	Thermo Fisher Sci	26619
Pierce™ Protease and phosphatase inhibitor mini tablets	Thermo Fisher Sci	A32959
Proteinase K	Sigma	AM2546
SuperSignal™ West Femto	Thermo Fisher Sci	34094
SYBR Safe DNA Gel Stain	Thermo Fisher Sci	S33102
Trizol Reagent	Life Technologies	15596-026

6.1.3.2 Cell culture media and reagents

Reagent	Manufacturer	Identifier
B-27 Supplement (50X)	Thermo Fisher Sci	17504-044
Conconamycin A	Sigma	C9705
BDNF	Almone	DE2457539
Cytosine ß-D-arabinofuranpsode hydrochloride	Sigma	C6645
DMEM (1X)+GlutaMAX™	Thermo Fisher Sci	31966-021
Deoxyribonuclease I from bovine pancreas	Sigma	D5025
EBSS	Thermo Fisher Sci	14155-048
Fetal Bovine Serum	Merck	S0115
Fetal Bovine Serum (sterile filtered) (FBS)	Sigma	F7524
GlutaMAX™	Thermo Fisher Sci	35050-061
HBSS (1X) [-] $CaCl_2$, [-] $MgCl_2$	Thermo Fisher Sci	14175-053
HEPES (1M)	Thermo Fisher Sci	15630-080
Insulin, human recombinant zinc	Thermo Fisher Sci	12585-014
MEM	Thermo Fisher Sci	51200-046
MG132	Sigma	M7449
Penicillin/Streptomycin (P/S)	Thermo Fisher Sci	15140-122
Poly-D-lysine (1mg/mL)	Merck	A-003-E
Sodium Pyrubate	Thermo Fisher Sci	11360-039
Transferrin, Holo, Bovine Plasma	Merck	616420
Trypsin from bovine pancreas	Sigma	T1005
(Z)-4-Hydroxytamoxifen (Tamoxifen)	Sigma	

6.1.3.3 Reagents for animals

Reagent	Manufacturer	Identifier
Isofluran	Piramal	B73E16A
Ketamin hydrochloride	Sigma	K2753
Rompun 2% (Xylazine)	Bayer	KP0BZPE

6.1.4 Kits and other equipment

Reagent	Manufacturer	Identifier
Endotoxin-free plasmid DNA purification	Macherey-Nagel	740420.10
High Capacity cDNA Reverse Transcription	Thermo Fisher Sci	4368814
Lipofectamine 3000	Thermo Fisher Sci	L3000-008

Lipofectamine RNAiMAX	Thermo Fisher Sci	13778-030
LIVE/DEAD™ Cell Imaging Kit	Thermo Fisher Sci	R37601
ProFection Mammalian Transfection System- Calcium Phosphate	Promega	E1200
qPCRBIO SyGreen Mix Lo-ROX	PC3 Biosystems	PB20.11
TaqMan™ Gene Expression Assay	Thermo Fisher Sci	4331182

6.1.5 Antibodies

Antibody				Manufacturer	Identifier
	WB	**ICC**	**IHC**		
Rabbit polyclonal anti-ATG16L1	1:1000	-	-	MBL	PM040
Rabbit monoclonal anti-ATG5	1:1000	-	-	Abcam	ab108327
Rabbit polyclonal anti-CASPASE-3 cleaved (Asp175)	1:1000	-	1:200	Cell Signaling	9661
Rabbit polyclonal anti-CLASP2	1:1000	-	1:500	Millipore	ABT263
Goat polyclonal anti-DNCT1	-	1:200	-	Abcam	ab11806
Rabbit polyclonal anti-ELKS1	1:1000	1:500	-	Novus Biologicals	NBP1-88178
Rabbit monoclonal anti-FIP200	1:1000	-	-	Cell Signaling	12436
Mouse monoclonal anti-GAPDH	1:1000	-	-	Sigma-Aldrich	G8795
Chicken polyclonal anti-GFP	-	1:2000	1:1000	Abcam	ab13970
Mouse monoclonal anti-GFP	1:5000	-	-	Takara Bio Clontech	632375
Rabbit polyclonal anti-LC3B	1:2000	-	-	Novus Biologicals	NB600-1384SS
Mouse monoclonal anti-LC3A/B	-	1:300	-	MBL	M152-3
Mouse monoclonal anti-MAP2	-	1:500	-	Sigma-Aldrich	M9942
Mouse monoclonal anti-MAPK activated (P-ERK-1&2)	1:1000	-	-	Sigma-Aldrich	M8159
Mouse monoclonal anti-mCherry	-	1:5000	-	Novus Biologicals	NBP1-96752
Rabbit polyclonal anti-mCherry	1:2000	-	-	Abcam	ab167453

Rabbit polyclonal anti-P-S6 Ribosomal Protein (Ser235/236)	1:1000	-	-	Cell Signaling	2211
Guinea pig polyclonal anti-p62	1:1000	1:500	1:1000	Progen	GP62-C
Rabbit monoclonal anti-P-AKT (Ser473)	1:1000	-	-	Cell Signaling	4060
Rabbit monoclonal anti-RAB7	-	1:250	-	Cell Signaling	9367S
Rabbit polyclonal anti-SYB2	-	1:800	-	Synaptic Systems	104 202
Rabbit polyclonal anti-TRKB	1:1000	1:250	-	Almone	ANT-019
Rabbit polyclonal anti-P-TRKB (Y816)	1:1000	1:250	-	Abcam	ab75173
Mouse monoclonal anti-α-TUBULIN	1:1000	1:500	-	Synaptic Systems	302 211
Mouse monoclonal anti- beta-3-TUBULIN	-	-	1:500	Thermo Fisher Sci	14-4510-80
Rabbit monoclonal anti-α-TUBULIN acetylated (Lys40)	1:1000	-	-	Cell Signaling	5335
Mouse monoclonal anti-α-TUBULIN tyrosinated	1:1000	-	-	Sigma-Aldrich	T9028
Rabbit polyclonal anti-α-TUBULIN detyrosinated	1:1000	-	-	Millipore	AB3201
Rabbit polyclonal anti-α-TUBULIN Δ2	1:1000	1:500	-	Synaptic Systems	302 213
Rabbit antiserum anti-UBIQUITIN	1:1000	1:200	-	Sigma-Aldrich	U5379
Goat anti-Mouse IgG (H+L) peroxidase-conjugated	1:5000	-	-	Jackson ImmunoResearch	115-035-003
Goat anti-Mouse IgG, light chain specific, peroxidase conjugated	1:5000	-	-	Jackson ImmunoResearch	115-035-174
Goat anti-Rabbit IgG (H+L) peroxidase-conjugated	1:5000	-	-	Jackson ImmunoResearch	111-035-003
Goat anti-Guinea Pig IgG (H+L) peroxidase-conjugated	1:5000	-	-	Jackson ImmunoResearch	106-035-003
Normal Rabbit IgG	1:5000	-	-	Cell Signaling	2729
Normal Mouse IgG	1:5000	-	-	Millipore	12-371
Alexa Fluor 488 Goat anti-Mouse IgG	-	1:500	-	Thermo Fisher Sci	A-11029
Alexa Fluor 488 Goat anti-Rabbit IgG	-	1:500	1:500	Thermo Fisher Sci	A-11034

Alexa Fluor 488 Goat anti-Chicken IgG	-	1:500	1:500	Thermo Fisher Sci	A-11039
Alexa Fluor 568 Goat anti-Mouse IgG	-	1:500	1:500	Thermo Fisher Sci	A-11031
Alexa Fluor 568 Goat anti-Rabbit IgG	-	1:500	1:500	Thermo Fisher Sci	A-11036
Alexa Fluor 568 Donkey anti-Goat IgG	-	1:500	1:500	Thermo Fisher Sci	A-11057
Alexa Fluor 647 Goat anti-Mouse IgG	-	1:500	1:500	Thermo Fisher Sci	A-21236
Alexa Fluor 647 Goat anti-Rabbit IgG	-	1:500	1:500	Thermo Fisher Sci	A-21245
Alexa Fluor 647 Goat anti-Guinea Pig IgG	-	1:500	1:500	Thermo Fisher Sci	A-21450
Abberior STAR 635P Goat anti-mouse IgG	-	1:1000	-	Abberior	ST635P

6.1.6 Oligonucleotides and vectors

Virus strain

Virus strain	Manufacturer	Identifier
AAV9-*CamKIIα*-eGFP	Penn Vector Core. University of Pennsylvania School of Medicine	AV-9-pV1917

6.1.6.1 Genotyping primers

Gene	Sequence (5'- 3')	Annealing temp (°C)
*Atg5*forward 1	GAA TAT GAA GCC ACA CCC CTG AAA TG	65
Atg5 forward 2	ACA ACG TCG AGC ACG CTG GCG AAG G	65
Atg5 reverse	GTA CTG CAT AAT GGT TTA ACT CTT GC	65
Atg16l1 forward	CAG AAT AAT TTC CGG CAG AGA CCG G	65
Atg16l1 reverse	AGC CAA AGA AGG AAG GTA AGC AAC GAA	65
Cre forward	CCG GGC TGC CAC GAC CAA	55
Cre reverse	GGC GCG GCA ACA CCA TTT TT	55
tdTomato forward	CTG TTC CTG TAC GGC ATG G	65
tdTomato reverse	AAG GGA GCT GCA GTG GAG TA	65
Postive control forward	CCG AAA ATC TGT GGG AAG TC	65
Positive control reverse	AAG GGA GCT GCA GTG GAG TA	65

6.1.6.2 qRT-PCR primers

Gene; Sequence (5'- 3')	Manufacturer	Annealing temp (°C)
Primer: *Bdnf* Forward: GGG TCA CAG CGG CAG ATA AA	Burbach et al. (2004)	58
Primer: *Bdnf* Reverse: GCC TTTGGATACCGGGACTT	Burbach et al. (2004)	58
Primer: *Ntrk2* Forward: CCG CTA GGA TTT GGT GTA CTG	PrimerBank ID: 6679150a1	58
Primer: *Ntrk2* Reverse: CCG GGT CAA CGC TGT TAG G	PrimerBank ID: 6679150a1	58
Primer: *Gapdh* Forward: AAC TTT GGC ATT GTG GAA GG	Kye et al. (2011)	58
Primer: *Gapdh* Reverse: ACA CAT TGG GGG TAG GAA CA	Kye et al. (2011)	58
Bcl-xl: Mm00437783_m1	Applied Biosystems	60
cFLIP: Mm01255580_m1	Applied Biosystems	60
Bax: Mm00432051_m1	Applied Biosystems	60
Chop: Mm00492097_m1	Applied Biosystems	60

6.1.6.3 siRNAs

Gene	Manufacturer	Annealing temp (°C)
siRNA *Erc1* (*Elks1*) smart pool	Dharmacon	L-058829-01-0005
siRNA *Maplc3b* smart pool	Dharmacon	M-040989-01-0005
siRNA *Mallc3a* smart pool	Dharmacon	L-056203-01-0005
siRNA *Fip200* smart pool	Dharmacon	L-041191-01-0005
siRNA Scrambled non-targeting smart pool	Dharmacon	D-001206-13-05

6.1.6.4 Plasmids

Plasmid (source gene)	Manufacturer	Identifier
pFUGW-H1-eGFP	Kononenko et al., 2013	N/A
pmCherry-N1	Kind gift from Dr. M. Kreutz	N/A
ptagRFP-C	Kind gift from Dr. M. Kreutz	N/A

pmStrawberry-ATG4BC74A (mouse)	Addgene	#21076
TRKB-mRFP (mouse)	Kononenko et al., 2017	N/A
EB3-tdTomato (human)	Addgene	#50708
Tubulin-eGFP (chicken)	Addgene	#66105
Plasmid: pEGFP-C1-mApg5 (mouse)	Kind gift from Prof M. Lammers	N/A
mito-mCherry	Kind gift from Prof E. Rugarli	N/A
ptagRFP-C-LC3B (pro LC3) (rat)	Kononenko Lab	N/A
ptagRFP-C-LC3BG120A (rat)	Kononenko Lab	N/A
eGFP-GABARAPL1	Kind gift from Dr Michael Schramm	N/A
eGFP-LC3B (rat)	Kind gift from Dr. M. Kreutz	N/A
eGFP-LC3A (human)	Kononenko Lab	N/A
tdTomato- ELKS1 (rat)	Kind gift from Dr. H. Kawabe and Prof. Nils Brose	N/A
SYB2-pHluorin (rat)	Kononenko et al., 2013	N/A

6.1.7 Cell lines

Cell line	Manufacturer	Identifier
Mouse embryonic fibroblast (MEFs)	Kind gift from Prof Dr. Thomas Langer	N/A
Human embryonic kidney (HEK) 293T	Kind gift from Prof Dr. Thomas Langer	N/A
Mouse motor neuron-like hybrid cell line (NSC-34)	Kind gift from Prof Dr. Brunhilde Wirth	N/A

6.1.8 Mouse models

Mouse model	Manufacturer	Identifier
C57BL/6J	CECAD *in vivo* facility	N/A
*Atg5*lox/lox: tamoxifen inducible CAG-Cre	Kononenko et al. (2017)	N/A
*Atg16*lox/lox: tamoxifen inducible CAG-Cre	Kononenko lab	N/A
*Atg5*lox/lox: *CamKIIα*-Cre	Kononenko lab	N/A
tdTomato:*CamKIIα*-Cre	The Jackson Laboratory	Ai9(RCL-tdT) line

6.1.9 Solutions and Media

6.1.9.1 Routinely used solutions

If not mentioned, solutions were stored at room temperature (RT)

Name	Composition
1.5M Tris pH 8.8	181.65g Tris Base; 0.4% (w/v) SDS; 1L ddH_2O ; pH 8.8
0.5M Tris pH 6.8	6g Tris Base; 0.4% (w/v) SDS; 100 mL ddH_2O; pH 6.8
10% Acrylamide gel	8.04 ml H_2O; 5ml 1.5M Tris pH 8.8, 6.67ml 30% acrylamide/bis, 200µl 10% SDS, 100µl APS 10%, 10µL TEMED
15% Acrylamide gel	5.04 ml H_2O; 5ml 1.5M Tris pH 8.8, 9.67ml 30% acrylamide/bis, 200µl 10% SDS, 100µl APS 10%, 10µL TEMED
4% Acrylamide gel (Stacking)	6mL ddH_2O; 2.52 mL 0.5 M Tris pH 6.8, 1.32 mL acrylamide/bis, 100µL 10%SDS, 50µL 10% APS, 10µL TEMED
2% agarose gel	2% (w/v) agarose in TBE 1X
B buffer	35.6g Na_2HPO_4*2H_2O, 31.7g Na_2HPO_4 in 500mL, pH=7.4 in 500mL H_2O
Blocking solution WB (BSA)	5% (w/v) BSA in TBS-T
Blocking solution WB (milk powder)	5% (w/v) milk powder in TBS-T
DMSO post-fixation	31.25 mL 0.4M PB, 46.75 mL H2O, 25.2g glycerin, 2mL DMSO
ICC blocking/permeabilizing solution	5% (v/v) NGS; 0.3% (w/v) Saponin, in PBS
Imaging Buffer	1mL B buffer; 100µL NaCl 5M; 4.9 µL $MgCl_2$, 13µL $CaCl_2$ 1M; total volume 10 mL
Neutralization Buffer	1.3g Tris-HCl in 200Ml dd$H_2$0. pH=5
Lammeli Buffer (4x)	250mM Tris-HCL;1% (w/v) SDS; 40% (v/v) Glycerol; 4% (v/v) ß-mercaptoethanol; 0.02% Bromophenol
PFA 4% (perfusion)	4% (w/v) PFA in PB 0.125 M, 60°C. pH 7.4
PFA 4% (ICC fixation)	4% (w/v) PFA, 4% (w/v) Sucrose, dissolved in PBS. pH 7.4
PBS	0.137M NaCl; 0.0027M KCl; 0.01M Na_2HPO_4; 1.8mM KH2PO4
Phosphate Buffer 0.4M (PB)	27.6g NaH_2PO_4, 35.6g Na_2HPO_4*2H_2O, 31.7g Na_2HPO_4 in 500mL, pH=7.4
Proteinase K solution	50mM Tris-HCl; 1mM $CaCl_2$; 50% Glycerol, in ddH_2O to generate dilution Buffer. + 20g Proteinase K for 1mL of dilution buffer.
Ponceau staining solution	1% (w/v) Ponceau S; 2% (v/v) acetic acid in ddH_2O
Ringer	0.85% (w/v) NaCl, 0.025% (w/v) KCl, 0.02% (w/v) $NaHCO_3$ in ddH_2O
RIPA buffer	50mM Tris-Base; 150 mM NaCl ; 1% (v/v) IGEPAL; 0.5% (w/v) Sodim deoxycholate; 0.1% (w/v) SDS dissolved in ddH2O (1

	tablet of protease inhibitor and phosphatase inhibitor/10mL RIPA buffer)
Running Buffer 10X	25mM Tris-Base; 192mM Glycine; 0.1% (w/v) SDS in ddH_2O
Transfer Buffer 10X	25mM Tris-Base; 192mM Glycine; 0.025% (w/v) SDS in ddH_2O
Transfer Buffer 1X	10% (v/v) Transfer Buffer 10X; 20% (v/v) methanol; 70% (v/v) ddH_2O
Tail lysis buffer	1M Tris-Base; 0.5M EDTA; 20% (w/w) SDS, 5M NaCl, in ddH_2O, pH 8.5
TBE 10X	108g Tris-Base; 55g Boric acid; 7.4g EDTA in 1L ddH_2O
TBS-T	20mM Tris; 137 Mm NaCl; 0.1% (v/v) Tween 20
Lysis buffer for IP (Co-IP buffer)	50 mM Tris-HCl; 1% IGEPAL; 100mM NaCl; 2mM $MgCl_2$ in ddH_2O (1 tablet of protease and phosphatase inhibitors/10Ml of lysis buffer)

6.1.9.2 Cell culture media

All cell culture media was filtered through 0.2 µm pore size membranes and stored at 4°C

Name	Composition
Basic Media	1L MEM; 5g Glucose; 200mg $NaHCO_3$, 100mg Transferrin
Borate Buffer 0.1M	1.24g boric acid; 1.9g sodium tetraborate in 400ml autoclaved ddH2O
Digestion Solution	137mM NaCl; 5mM KCl; 7mM Na_2HPO_4; 25mM HEPES dissolved in autoclaved ddH_2O. pH 7.2
Dissociation Solution	Hank's + 12mM MgSO4x7H_2O
Growth Media	100mL Basic Media; 5mL sterile filtered FBS; 0.25mL GlutaMAX; 2mL B-27; 1mL P/S
Hank's solution	500 mL HBSS; 5mL Sodium pyrubate; 5mL HEPES; 5mL P/S
Hank's + 20% FBS	Hank's + 20% (v/v) sterile filtered FBS
Plating Media	100 mL Basic Media; 10 mL sterile filtered FBS; 1mL GlutaMAX; 625µL Insulin; 1.1 mL P/S
Cell line media	DMEM + 10% (v/v) FBS + 0.1% (v/v) P/S

6.2 Methods

6.2.1 Animals

C57/BL/6 mice were housed in polycarbonate cages at standard 12/12 day-night cycles and water, and food was provided *ad libitum*. All animal experiments were approved by the ethics committee of LANUV Cologne and were conducted according to the committee's guidelines. Conditional tamoxifen-inducible ATG5 KO ($ATG5^{flox/flox}$: B6.Cg-Tg(CAG-cre/Esr1*)5Amc/J) is described inthe results section, and Kononenko et al.(2017). Conditional forebrain confined ATG5 KO mice were created by crossing $Atg5^{flox/flox}$ mice with CamKIIα-Cre line (Dragatsis and Zeitlin, 2000b), kindly provided by Prof. Aleksandra Trifunovic (CECAD, Cologne, Germany). $Atg16l1^{flox/flox}$ mice (Adolph et al., 2013a) were received from Prof. Philip Rosenstiel (University Hospital Kiel, Germany). Conditional tamoxifen-inducible ATG16L1 KO mice were created by crossing $Atg16l1^{lox/lox}$ mice with a Tamoxifen-inducible CAG-Cre line (B6.Cg-Tg(CAG-cre/Esr1*)5Amc/J; The Jackson Laboratory).Ai9(RCL-tdT) (tdTomato) line (The Jackson Laboratory) was received from Dr. Matteo Bergami (CECAD, Cologne, Germany). To reveal the CamKIIα-Cre activity in the brain Ai9(RCL-tdT) mice were crossed with CamKIIα-Cre line.

6.2.2 Genotyping

DNA extraction. Newborn pups were tattooed after birth, and subsequently, a 1mm of the tail from each pup was collected for genotyping. DNA extraction from each tail sample was performed by the incubation of samples in 300 µL of tail lysis buffer plus 3 µL of proteinase K solution at 55°C overnight (ON). For the isolation of DNA, digested samples were centrifuged at 13 000 revolutions per minute (rpm) for 5 min. Next, the supernatant was discarded, and the pellet was resuspended with 400 µL of isopropanol and gently mixed prior centrifugation at 13 000 rpm for 15 min. Again, the supernatant was discarded, and DNA was washed once with 70% ethanol, followed by another centrifugation of 13 000 rpm for 10 min. Finally, the supernatant was discarded, the pellet dried out, and resuspended with 100 µL of autoclaved water.

PCR. DNA samples were diluted in PCR tubes following the master mix showed below. Note that working primers were diluted at 10pmols/µL.

Atg5, Cre, tdTomato	Volum (µL)
Sample	1
Dream Taq Buffer	2
$MgCl_2$ 25mM	2
Primer mix	1 each primer
DNTPs 2 mM	1.5
Dream Taq pol.	0.2µL
H2O till 20 µL total	

Atg16l1	Volum (µL)
Sample	1
LongAmp Buffer	5
Primer Mix	1 each primer
DNTPs 2 mM	3.75
LongAmp Taq pol.	1
H2O till 20 µL total	

PCR program:

Step		*Atg5* (36 cycles)		*Atg16l1* (35 cycles)		*Cre* (35 cycles)	
		T (°C)	Time	T (°C)	Time	T (°C)	Time
Initial denaturation		94	4min	94	2 min	95	5min
cycles	**denaturation**	94	30s	94	30s	95	30s
	Anneling	63	30s	65	30s	62	30s
	Elongation	72	60s	68	300s	72	30s
Final extension		72	60s	68	480s	72	5min
Hold		4		4		4	

Step		*tdTomato*	
		T (°C)	Time
Initial denaturation		94	2min
10 cycles	**Denaturation**	94	30s
	Anneling	65 (-0.5 each cycles)	30s
	Elongation	68	60s
28 cycles	**Denaturation**	94	15s
	Anneling	60	15s
	Elongation	72	10s
Final extension		72	2 min
Hold		4	

Elctrophoresis. PCR results were subsequently mixed with DNA loading sample and charged in a 2% Agarose gel with SYBR safe, at a concentration indicated by the manufacture by guideline. Finally, electrophoresis was done at 120V for 40 min (1% agarose gel, 120V, and 120 min for *Atg16l1* samples) and results were visualized by the gel imager system (Bio-Rad).

6.2.3 Preparation of neuronal cultures and transfections

Neuronal cell culture. Cortex and hippocampi were isolated from postnatal pups at P1–5, cut in small pieces, washed twice in Hank's+20%FBS and Hank's, and digested with 10 mg trypsin and 10 µL DNasedissolved in 2 mL of digestion solution, which was then incubated at 37°C for 15 min.Trypsination was stopped by washingtwice with Hank's+20%FBS and Hank's, prior addition of 2 mL of dissociation solution containing 10 µL of DNAse. Samples were mechanically dissociated by pipetting 2-3 times with a fire-polished glass pipette, followed by the centrifugation of cells at 0.3 rcf, 8 min at 4°C. The supernatant was discarded, and the pellet of cells was re-suspended in plating media, which were then counted with a solution of trypan blue and a Neubauer chamber. 50µL solution containing 110 000 cells were plated in pre-coated 24mm diameter coverslips or 3 cm diameter dishes. The coating was performed the day before by dissolving the PDL with borate buffer 0.1M and adding it on the coverslips or dishes for 2 to 16 hours, which afterward were washed with autoclaved water and dried. Once cells are attached to the surface of the coverslip or dish (1-2 h), 2 mL of prewarmed plating media was added to each well and cells were placed inside the incubator at 37°C/5% CO_2. After 24 h, half of the media was removed, and the same amount of Growth media with 2 µM ofcytosine ß-D-arabinofuranoside hydrochloride was added. 48 h after the cell culture preparation, the same volume of media used after 24 h was added with 4 µM of cytosine ß-D-arabinofuranoside hydrochloride. No further media was added afterward.

Induction of homologous recombination of Atg5 or Atg16l1 KO alleles by tamoxifen. To initiate homologous recombination in neurons from floxed animals expressing a tamoxifen-inducible Cre recombinase, cultured neurons were treated with 0.2 µM (Z)-4-hydroxytamoxifen immediately after plating. After 24h hours, cells weretreated with 0.4 µM of tamoxifen during medium removal. Ethanol was added to control neurons (WT) in an amount equal to the tamoxifen.

Plasmid and siRNA transfections. Neurons were transfected at DIV 7–9 using an optimized calcium phosphate protocol (Kononenko et al., 2013). In brief, 6µg plasmid DNA, 12.5µL of $CaCl_2$2M, and 81.5 µL of water (for each well of a 6-well plate) were mixed with an equal volume of 2x HEPES buffered saline (100µl) (ProFection Mammalian Transfection System- Calcium Phosphate) and incubated for 20 min, allowing for precipitate formation. Meanwhile, neurons were incubated in NBA medium for the same time at 37°C, 5% CO2. Subsequently, precipitates were added to the cells and incubated at 37°C, 5% CO2 for 30 min. Finally, neurons were washed twice with HBSS medium and transferred back to the medium. Note that the osmolarity of NBA and HBSS media was readjusted the original cellular media of the neurons with D-mannitol.In the case

of siRNA knockdown experiments,eGFP plasmid was always co-transfected with 100nM siRNAs on DIV-7-9, and the cells were analyzed 5-8 days posttransfection.

6.2.4 Stereotaxic injection of AAV9-CamKIIα-eGFP

Stereotactic injections were performed on 12-13 week-old *Atg5*$^{flox/flox}$:*CamKIIα*-Cre WT and KO mice. Mice were anesthetized with a mixture of Ketamine (100mg/kg)/ Xylazin (20mg/kg)/ Acepromazine (3 mg/kg) and mounted in a Kopf stereotactic frame. For the injection, a small hole was made in the skull of the mouse and a 1µl Hamilton syringe filled with 300nl of AAV9-CamKIIα-eGFP was lowered into the M1 area of the primary motor cortex, using following coordinates: AP- 1.25, DL- 1.8, Depth- 0.52. A volume of 300 nl AAV was delivered during 5 min, with a 5-min delay after the penetration, and waiting another 15 min before withdrawing of the syringe. The animal was given a dose of carprofen to reduce postsurgical pain (s.c, 5 mg/kg) before the end of the surgery. Suturing the skin over the wound completed surgery and the animal was then allowed to recover. Animals were sacrificed by transcardial perfusion 10-14 days after surgery, and the eGFP expression was analyzed by confocal microscopy (see Immunohistochemical analysis of brain sections).

6.2.5 Generation and use of plasmids

Cloning and generation of plasmids were performed by Dr Sujoy Bera. Briefly, Rat *Lc3b* sequence (GeneID: 64862) was cloned in ptagRFP-C vector (Gift from Dr Michael Kreutz) using Bgl II and EcoRI restriction enzymes. For generating the LC3BG120A, Glycine at 120 was mutated to alanine, and a stop codon was introduced after the alanine 120 by side-directed mutagenesis. pFUGW-H1-eGFP, TRKB-mRFP, and Syb2-pHluorin were described previously ((Kononenko et al., 2017a; Kononenko et al., 2013). pmCherry-N1 and ptagRFP-C were kindly provided by Dr. Michael Kreutz (LIN, Magdeburg, Germany). pmStrawberry-ATG4BC74A, EB3-tdTomato, and Tubulin-eGFP were purchased from Addgene. pEGFP-C1-mApg5 and mito-Cherry were kind gifts from Prof. Michael Lammers (University of Greifswald, Germany) and Prof. Elena Rugarli (CECAD, Germany), accordingly.

6.2.6 Long-term treatment with BDNF

Neurons were treated with 50 ng/mL of recombinant BDNF (the same amount of water was used as a control) at DIV 2, 6, 10 and 14. Neurons were fixed or harvested at DIV 16 for ICC or WB, respectively.

6.2.7 MG132 treatment of cultured neurons

For inhibiting the proteasome system, cultured DIV 15 neurons were treated for 16 h with 10 µM of MG132 (the same amount of DMSO was used as a control). After the treatment, neurons were harvested for WB analysis.

6.2.8 Immunocytochemistry and analysis of cultured neurons

Neurons were fixed at DIV 16-18 in 4% PFA/sucrose in phosphate-buffered saline (PBS) for 15 min at room temperature (RT), washed three times, permeabilized and blocked with PBS containing 5% NGS, 0.3% Saponin for 1 h. After blocking, neurons were incubated with primary antibodies for 1 h blocking solution. Coverslips were rinsed four times with PBS (2-5 min each) and incubated with corresponding secondary antibodies, which were diluted againin blocking solution, for 30 min. Subsequently, coverslips were washed three times in PBS and mounted in Immu-mount (Thermo Fisher Sci). Fixed neurons were imaged using either Zeiss Axiovert 200M microscope equipped with 40x/1.4 oil DIC objective and the Micro-Manager software (Micro-Manager1.4, USA) or with Leica SP8 confocal microscope (Leica Microsystems) equipped with a 63x/1.32 oil DIC objective and a pulsed excitation white light laser (WLL; ~80-ps pulse width, 80-MHz repetition rate; NKT Photonics). For quantitative analysis of fluorescent protein levels (or fluorescent puncta), the area of the neuron, cell body, axon or spheroid (depending on the experiment) was manually selected using ImageJ selection tools (ROI), and the mean gray value was quantified within the ROI after the background subtraction. Fluorescent puncta were determined by applying the autothreshold “minimum” algorithm implemented in ImageJ and analyzed using the “Analyze particles” ImageJ module to determine the number of fluorescent puncta per 1 μm^2. For quantifying the number of neurons containing axonal swellings, coverslips were imaged by using EVOS FL Auto 2 (Invitrogen, USA). For quantifying the number of spheroids per axon, the quantity and the diameter of spheroids from WT and KO neurons were analyzed in

the last 300µm of the axon by the ImageJ. The number of dendritic spines was quantified per 10 µm of the primary dendrite per neuron.

6.2.9 Immunostaining of αTubulin in cultured neurons

Neurons were treated on DIV 16 either with 0.2 µg/ml Nocodazole (Sigma) or with 0.2 µg/ml DMSO for 1 h. Afterward, they were rinsed with warm PHEM buffer (60 mM PIPES, 25 mM HEPES, 10 mM EGTA, 4 mM $MgCl_2$), followed by an incubation step in PHEM buffer containing 0.05% Triton-X-100 and a protease inhibitor cocktail (Roche) at 37°C for 1.5 min to remove the soluble Tubulin. Afterward, neurons were fixed with cold methanol (-20°C) for 8 min, permeabilized and blocked with PBSS (PBS containing 0.2% saponin and 2.5 BSA) for 30 min at RT and incubated with primary antibodies diluted in PBSS for 2 h. Coverslips were washed twice in PBSS (2 min each) and incubated with corresponding secondary antibodies (diluted 1:500) in PBSS for 30 min. Finally, coverslips were washed four times in PBSS and mounted in Immu-mount.

6.2.10 STED imaging

Cultured cortical/hippocampal neurons were fixed under MTs stabilization conditions, as previously described (Zempel et al., 2017). Subsequent MT extraction of neurons was performed by using 0.5% Triton X-100, 5% BSA in PBS, followed by antibody incubation without further blocking reagents or detergents. Finally, coverslips were mounted in ProLong Gold (Thermo Fisher Scientific) and imaged with SP8 STED imaging. STED imaging with time-gated detection was performed using a commercial Leica SP8 TCS STED microscope (Leica Microsystems) equipped with a pulsed excitation white light laser (WLL; ~80-ps pulse width, 80-MHz repetition rate; NKT Photonics) and two STED lasers for depletion (continuous wave at 592 nm, pulsed at 775 nm). The pulsed 775-nm STED laser was triggered by the WLL. Fluorescence signals were detected sequentially by hybrid detectors at appropriate spectral regions separated from the STED laser by corresponding dichroic filters. Images were acquired with an HC PL APO CS2 × 100/1.40-N.A. oil objective (Leica Microsystems), a scanning format of 1,024 × 1,024, eight-bit sampling, and 4.5 zoom, yielding a pixel dimension of 25.25 nm and 25.25 nm in the *x* and *y* dimensions, respectively.

6.2.11 Sholl analysis of cultured neurons

Neurons were transfected with eGFP on DIV 8. Cells were either fixed on DIV 16-18 and processed as above. Neurons were imaged with a Leica SP8 confocal microscope using a Plan-Apochromat 63X/1.32 Oil DIC objective, corrected for both chromatic and spherical aberrations. Neurons were scanned at a resolution of 1024×1024, eight-bit sampling, zoom 1 and z-increment of 0.5 µm. Sholl analysis of single cells was performed using the ImageJ Sholl Analysis Macro. The complexity of neuronal branching was calculated by summing the number of intersections within 200 µm from the cell body.

6.2.12 Live imaging of cultured neurons

Neurons were imaged on DIV 16-18 at 37ºC in imaging buffer (see above) using Zeiss Axiovert 200M microscope (Observer. Z1, Zeiss, USA) equipped with 63X/1.40 Oil DIC objective;a pE-4000 LED light source (CoolLED) and a Hamamatsu Orca-Flash4.O V2 CMOS digital camera. Time-lapse images of neurons expressing TRKB-mRFP were acquired every second using Micro-Manager software (Micro-Manager1.4, USA) for 30 s. In the case of experiments with EB3-Tdtomato and Mito-Cherry plasmids videos were acquired every second for 60 s. Kymographs were generated using the software KymoMaker (Chiba et al., 2014) and analyzed by ImageJ. To monitor the exocytosis of synaptic vesicles via SYB2-pHluorin assay, neurons were subjected to electrical field stimulation at 50Hz for 4 s using an RC-47FSLP stimulation chamber (Warner Instruments) and imaged as described above (Time-lapse images were acquired every second for 2 min). To prevent the activation of postsynaptic receptors, 10 µM CNQX and 50 µM AP-5 were added to the imaging buffer prior to imaging.

To image the percentage of live and dead neurons, LIVE/DEAD^{TM} Cell Imaging Kit (Thermo Fisher Scientific) was used. Following manufacturer indications, an equal amount of imaging buffer was mixed with the dye and added to WT and ATG5 KO neurons (DIV 16) for 15 min at RT. Subsequently, neurons were imaged using Zeiss Axiovert 200M microscope (Observer. Z1, Zeiss, USA) equipped with 20X objective;a pE-4000 LED light source (CoolLED) and a Hammatsu Orca-Flash4.O V2 CMOS digital camera. The analysis was performed using ImageJ.

6.2.13 Electron microscopy

Cortical/hippocampal neurons cultured on 18 mm Ø coverslips were fixed with a pre-warmed fixative solution (2% glutaraldehyde, 2.5% sucrose, 3 mM $CaCl_2$, 100 mM HEPES, pH 7.4) at RT for 30 min, followed by the post-fixation at 4°C for 30 min. Afterward, cells were washed with 0.1 M sodium cacodylate buffer, incubated with 1% OsO_4, 1.25% sucrose, 10mg/ml $K_4[Fe(CN)_6]\cdot 3H_2O$ in 0.1 M cacodylate buffer for 1 h on ice and washed three times with 0.1 M cacodylate buffer. Subsequently, cells were dehydrated at 4°C using ascending ethanol series (50, 70, 90, 100%, 7 min each), incubated with climbing EPON series (EPON with ethanol (1+1) for 1 h; EPON with ethanol (3+1) for 2 h; EPON alone ON; 2 x 2 h with fresh EPON at RT) and finally embedded for 48-72 h at 62°C. Coverslips were removed with liquid nitrogen and heat, consecutively. Ultrathin sections of 70 nm were made using an ultramicrotome (Leica, UC7) and stained with uranyl acetate for 15 min at 37°C and lead nitrate solution for 4 min. Electron micrographs were taken with a JEM-2100 Plus Electron Microscope (JEOL), Camera OneView 4K 16 bit (Gatan) and software DigitalMicrograph (Gatan).

6.2.14 Immunohistochemical analysis of brain sections

Mice were euthanized at 12-15 week-old by an overdose of ketamine/xylazine, 1.2%/0.16%, respectively in PBS (i.p., 10 µl per 10 g body weight) and transcardially perfused with 50 ml saline solution (Ringer) (0.85% NaCl, 0.025% KCl, 0.02% $NaHCO_3$, pH 6.9, 0.01% heparin, body temperature), followed by 50 ml cold (7–15 °C) freshly depolymerized 4% (w/v) PFA in 0.125 M Phosphate buffer (PB), pH 7.4. Brains were carefully taken out of the skull, postfixed overnight in the same fixative solution, and placed in a mixture of 20% (v/v) glycerol and 2% (v/v) dimethylsulfoxide in 0.4 M PB for 24 h for cryoprotection. Frozen horizontal sections (40 µm) were collected in six series in DMSO using the microtome. For immunostaining, corresponding sections from WT and KO littermates were processed simultaneously. Sections were washed three times in PB (3 × 15 min each), followed by permeabilization with PB containing 0.3% Triton X-100 (9 × 20 min each). Sections were preincubated with PB containing 5% (v/v) NGS and 0.3% (v/v) Triton X-100 for 1 h and subsequently incubated with primary antibody at 4 °C for 48 h. Then, sections were washed nine times for 20 min each in 0.3% Triton X-100 in 0.125 M PB and incubated with Alexa-conjugated secondary antibodies (1:500) for 2 h using standard techniques. The sections were washed three times for 15 min each in 0.125 M PB. Finally, sections were mounted on gelatin-coated glass slides (see also Kononenko et al., 2013).

6.2.15 Nissl staining

Sections were mounted in 0.2% gelatin solution in 250 mM Tris-HCl and dried overnight at 40 °C on a heating plate. Mounted parts were re-hydrated for 1 min in water and stained for 5–10 min in 0.1% cresyl violet solution. Subsequently, sections were rinsed three times (2 min each) in water and dehydrated using an ascending ethanol series (50, 70, 80, 90%) for 2 min each. After rinsing the sections in 96% ethanol, they were destained with 0.5% acetic acid and washed twice in 100% ethanol (2 min each), incubated with xylene for 2 min and subsequently mounted using Entellan (Kononenko et al., 2017a).

6.2.16 Western blotting

Mice were sacrificed at 12-15 week-old by cervical dislocation. Brains were dissected and immediately placed into liquid nitrogen to be stored at -80 °C for further use or directly homogenized with a Wheaton Potter-Elvehjem Tissue Grinder in RIPA buffer (50 mM Tris pH 8.0, 150 mM NaCl, 1.0% IGEPAL CA-630, 0.5% Sodium deoxycholate, 0.1% SDS) containing protease inhibitor cocktail (Roche), sonicated and incubated for 1 h on ice for the protein extraction. To extract protein from cortical/hippocampal primary cultures, neurons were harvested at DIV16-18 with RIPA buffer containing protease inhibitor and phosphatase inhibitor cocktail (Thermo Scientific), sonicated, and placed for 30 min on ice. The lysates were centrifuged at 13300 rpm at 4˚C and supernatants were collected and used for further analysis. Protein concentrations were determined by Bradford assay. Depending on the experiment, 2-20 µg of total protein were loaded onto the gel and separated by SDS-PAGE, and then transferred to a nitrocellulose or PVDF membrane (LC3 blots). Membranes were blocked for 1 h at RT in 5% skim milk (or with BSA, for phosphor antibodies) in TBS-T and incubated with primary antibodies ON at 4°C, followed by the washing of membranes three times (10 min each) with TBS-T. Afterward, the membranes were incubated with secondary antibodies diluted in 5% skim milk or BSA in TBS-T buffer for 1.5 h at RT. After the incubation, the membranes were washed three times as above and subsequently developed using ECL based autoradiography film system for documentation. The analysis was performed using Image J Analyze Gel plugin.

Starvation was induced by exchanging the original media with the osmolarity-adjusted Earle's Balanced Salt Solution (EBSS). Cells were incubated at 37°C/5% CO_2 ON for 16 h and harvested for WB analysis as described above.

In order to study the levels of acetylated α-tubulin, neuronal cultures were harvested with a lysis buffer containing 6 M Urea, 50 mM Tris, 150 mM NaCl, 0.1% SDS, 1% Triton, pH 7.4. Protein samples were then processed as described above.

6.2.17 Extraction of soluble and polymerized tubulin fractions

To fractionate soluble and polymerized microtubules from cultured cortical/hippocampal neurons, first the lysis Buffer A1 (137 mM NaCl, 20 mM Tris-HCl, 1% Triton X-100 and 10% Glycerol) was added to the cells at DIV 16 at 4°C for 3 min, plates were gently swirled two to three times, and the supernatant was collected as a soluble fraction (Sharma et al., 2011b). Immediately after, polymerized tubulin was extracted using lysis Buffer B (Buffer A+1% SDS), which was added to the cells for 1 min, and the cells were harvested as a polymerized fraction. Both soluble and polymerized fractions were briefly sonicated, incubated on ice 30 min, and protein levels were quantified using Bradford assay. Samples were processed using SDS-PAGE sample buffer and analyzed by Western blotting.

6.2.18 Extraction of dynamic microtubule fraction

A similar protocol as above with minor modifications was used to fractionate the dynamic microtubule fraction. To isolate the dynamic microtubules, first, the soluble fraction was extracted at DIV 16 with the lysis Buffer A2 containing 137 mM NaCl, 20 mM Tris-HCl and 0.1% digitonin (Sigma) for 10 min at RT. Next, to induce the depolymerization of stable microtubules, neurons were incubated with Buffer A2 at 4°C for 1 h. The supernatant was collected and saved as dynamic microtubule fraction. Cold-stable microtubules were extracted with Buffer B (Buffer A2+1% SDS) and proceeded as above.

6.2.19 Co-immunoprecipitation assays

To immunoprecipitate α-tubulin from cultured WT and ATG5 KO neurons, first, the soluble MT fraction was extracted as described above (under “Extraction of soluble and polymerized tubulin fractions”**)**. Remaining cells were then incubated with the Co-IP buffer (50 mM Tris-HCl, 1% NP-40, 100 mM NaCl, 2 mM $MgCl_2$, a protease inhibitor (Roche), pH 7.4) and the extraction of polymerized tubulin was performed by incubating the cell lysates at 4°C for 45 min. Following

incubation, the lysates were centrifuged at 3000 rpm for 5 min at 4°C and supernatants were collected and used as polymerized fractions for immunoprecipitation (IP) assay. For the IP, Dynabeads Protein G (Invitrogen) were coupled either to the α-tubulin antibody or to an equivalent amount of non-specific IgG as a control. After the coupling, the unbound antibody was removed by carefully placing the tubes on the magnetic bar. Antibody-coupled Dynabeads were then incubated with soluble and polymerized tubulin fractions. For the IP from the soluble fraction, the Dynabeads were incubated overnight at 4°C to avoid the polymerization of tubulin, while the polymerized fraction was incubated for 1 h at RT. Samples were then washed 3 times using Co-IP buffer. Proteins were eluted in 4XSDS sample buffer and analyzed by Western blotting.

For experiments in HEK293T cells, cells were maintained in DMEM medium (GIBCO), containing 10 % FCS, penicillin (255 Units/ml) and streptomycin (255 µg/ml). 24 hours after seeding, the cells were transfected with eGFP or eGFP-LC3B, eGFP-LC3A, eGFP-GABARAPL1 along with tdTomato-ELKS1. Following 20 hours of overexpression, cells were harvested and lysed with the Co-IP buffer, and immunoprecipitation assays were performed by incubating the cell lysates with magnetic GFP-microbeads (Miltenyibiotech, Germany). The samples were analyzed by WB as described above.

6.2.20 *In-vitro* pull-down

Full-length human LC3B was expressed from pRSF-Duet-1 (G2P) as His_6-tagged fusion protein. The expression was performed in *Escherichia coli* BL21 (DE3). The cells were harvested by centrifugation (15 min, 4000 rpm, 4°C), resuspended in buffer A (100 mM NaCl, 50 mM Tris/HCl pH 7.4, 5 mM $MgCl_2$, 2 mM □-mercaptoethanol, 100 µM Pefabloc) and lysed by sonication. The His_6-LC3B containing supernatant after centrifugation (45 min, 20.000 rpm) was loaded onto an equilibrated Ni-NTA column (Ni Sepharose 6 Fast Flow, GE Healthcare) using buffer B (100 mM NaCl, 50 mM Tris/HCl pH 7.4, 5 mM $MgCl_2$, 2 mM □-mercaptoethanol) plus 20 mM Imidazole. The column was washed 10 times with column volumes of washing buffer C (300 mM NaCl, 50 mM Tris/HCl pH 7.4, 5 mM $MgCl_2$, 20 mM Imidazole, 2 mM □-mercaptoethanol) and the His_6-LC3 protein eluted using a 20 mM to 500 mM Imidazole gradient in buffer B. The His_6-LC3B containing fractions were pooled and concentrated using a 3 kDa MWCO Amicon ultrafiltration unit for the subsequent size-exclusion chromatography on a HiLoad 26/600 Superdex 75 pg column (GE Healthcare) in buffer D (50 mM HEPES pH 7.9, 100 mM NaCl, 5 mM $MgCl_2$, 2 mM □-mercaptoethanol). The His_6-LC3 containing fractions were pooled, shock-frozen in liquid nitrogen,

and stored at -80°C. Purified recombinant MYC/DDK tagged human ERC1 protein was purchased from (OriGene CAT#: TP313864). For the assay 2 µg of His_6-LC3B was mixed with 1 µg of MYC/DDK-ERC1 in reaction buffer (50 mM Tris, pH 7.6, 500 mM NaCl, 5 mM $MgCl_2$, 2 mM □-mercaptoethanol, 10% Glycerol, 30 mM Imidazole) with 30 µl of Ni-NTA magnetic agarose beads (Qiagen). For the control group, only MYC/DDK-ECR1 was added to the Ni-NTA magnetic beads. The reaction mixture was incubated for 1 hour at 4°C with gentle shaking. Following the incubation, the beads were washed three times with the reaction buffer, and proteins were eluted from the beads by adding 4X SDS-PAGE sample buffer, and the samples were analyzed by immunoblotting using ELKS1 and LC3B antibodies.

6.2.21 Knockdown experiments in MEF or NSC-34 cells

Mouse embryonic fibroblasts (MEFs) or mouse motor neuron-like hybrid cell line (NSC-34) were transfected with 300pM siRNA using Lipofectamine RNAiMAX Reagent. Gene silencing was achieved by two consecutive rounds of transfections with the interval of 24h. 48h after the first transfection cells were harvested and cell lysates were then analyzed by WB.

6.2.22 Quantitative RT-PCR

RNA isolation was performed under RNase-free condition: using sterile tubes and pipette tips, nuclease-free water, and a mask to cover the mouth. RNA isolation was performed using Trizol (Thermo Fisher Scientific) following manufacturing indications. To obtain complementary DNA (cDNA) for qRT-PCR analysis, RNA was reversely transcribed with the High-capacity cDNA Reverse Transcription Kit. 20 ng of total RNA was used for reverse transcription following the manufacturer´s instructions. Quantitative real-time PCR allows to monitor the progress of the PCR reaction in real-time; thus, the photodetector 7500 Real-time PCR System was used for fluorescent detection. As a dye, qPCRBIO SyGreen Mix Kit was utilized for fluorescent detection, which is able to bind to double DNA and emit fluorescence when it unconjugated. qRT-PCR experiments were conducted in a 96-well plate with duplicates for each sample. Annealing temperatures for each couple of primers were optimized prioranalysis with ATG5 KO samples. The threshold of the cycle (Ct) value is given by the cycle number in which the fluorescence signal in the exponential amplifying phase passes the fixed threshold (0.1). The composition and reaction conditions were followed by manufacture instructions:

Component	Amount
2x qPCRBIO SyGreen Mix	20 µL
1 µM forward primer	4 µL
1 µM reverse primer	4 µL
cDNA	6µL (6ng)
Nuclease-free wáter to a final volumen of 40 µL	

Step		T (°C)	Time
Stage 1		50	2min
Stage 2		95	10 min
Stage 3 40 cycles	**Denaturation**	95	15s
	Annealing	58	40s
	Elongation	72	60s
Hold		4	

Gapdh housekeeping expression was evaluated using two other housekeeping genes, *Rrn18s* and *Hprt1*(Kye et al., 2011). qPCR analysis of the mRNA expression of pro-survival and pro-apoptotic genes was performed using a universal PCR master mix and TaqMan probes (Applied Biosystems; Bcl2l1/Bcl-xL: Mm00437783_m1, cflar/cFlipL: Mm01255580_m1, Dtit3/Chop: Mm00492097_m1, Bax: Mm00432051_m1) and the Ct values were normalized to TATA-box-binding protein (*Tbp*) that was used as reference gene. Relative expression of gene transcripts was assessed using the 2-ΔΔCt method (Kondylis et al., 2015).

6.2.23Statistical Analysis

For analysis of experiments, significant estimates were obtained from independent experiments (N). MS Excel and GraphPad Prism version 7 were used for the assessment of the statistical analysis. The statistical significance between two groups for all normally distributed raw data except growth factor treatments was evaluated with a two-tailed unpaired t-test student. Effect of BDNF on neuronal complexity wasassessed using paired student's t-tests. The statistical significance between more than two groups for all normally distributed raw data was evaluated using Two-Way ANOVA (Tukey posthoc test was used to determine the statistical significance between the groups). All normalized data were assessed using one-sample student’s t-test. Statistical significance on variables obtained from Sholl analysis was calculated using two-way

ANOVA with repeated measurements after data normalization using Ln transformation. Significant differences were accepted at $p<0.05$.

7. DATA CONTRIBUTION

In this thesis dissertation, other researchers have contributed by generating/analyzing some of the data presented in the results section. Next table clarify the contribution of external researchers.

Figure	**Contribution**	**Researcher**	**Institution/lab**
7b,d, g	Analysis	Dr Elodie De Bruyckere	CECAD/Kononenko lab
8c,d	Stereotaxic injection	DrNatalia L. Kononenko	CECAD/Kononenko lab
12b,d	Data generation/analysis	Melina Overhoff	CECAD/Kononenko lab
13d,h	Data generation/analysis	Melina Overhoff	CECAD/Kononenko lab
14c,g	Data generation/analysis	Melina Overhoff	CECAD/Kononenko lab
18d	Analysis	Dr Sujoy Bera	CECAD/Kononenko lab
26	Data generation	Dr Sujoy Bera	CECAD/Kononenko lab
26f	Protein synthesis/purification	Qin Chuan	Greifswald/Lammers lab
28a-d	Data generation/analysis	Melina Overhoff	CECAD/Kononenko lab
29a	Data generation	Melina Overhoff	CECAD/Kononenko lab
30a,b	Data generation/analysis	Melina Overhoff	CECAD/Kononenko lab

8. REFFERENCES

Adolph, T.E., Tomczak, M.F., Niederreiter, L., Ko, H.-J., Bock, J., Martinez-Naves, E., Glickman, J.N., Tschurtschenthaler, M., Hartwig, J., Hosomi, S*., et al.* (2013a). Paneth cells as a site of origin for intestinal inflammation. Nature *503*, 272-276.

Adolph, T.E., Tomczak, M.F., Niederreiter, L., Ko, H.J., Bock, J., Martinez-Naves, E., Glickman, J.N., Tschurtschenthaler, M., Hartwig, J., Hosomi, S*., et al.* (2013b). Paneth cells as a site of origin for intestinal inflammation. Nature *503*, 272-276.

Aher, A., Kok, M., Sharma, A., Rai, A., Olieric, N., Rodriguez-Garcia, R., Katrukha, E.A., Weinert, T., Olieric, V., Kapitein, L.C*., et al.* (2018). CLASP Suppresses Microtubule Catastrophes through a Single TOG Domain. Dev Cell *46*, 40-58 e48.

Akhmanova, A., Hoogenraad, C.C., Drabek, K., Stepanova, T., Dortland, B., Verkerk, T., Vermeulen, W., Burgering, B.M., De Zeeuw, C.I., Grosveld, F*., et al.* (2001). Clasps are CLIP-115 and -170 associating proteins involved in the regional regulation of microtubule dynamics in motile fibroblasts. Cell *104*, 923-935.

Akhmanova, A., and Steinmetz, M.O. (2008). Tracking the ends: a dynamic protein network controls the fate of microtubule tips. Nat Rev Mol Cell Biol *9*, 309-322.

Akhmanova, A., and Steinmetz, M.O. (2010). Microtubule +TIPs at a glance. J Cell Sci *123*, 3415-3419.

Alushin, G.M., Lander, G.C., Kellogg, E.H., Zhang, R., Baker, D., and Nogales, E. (2014). High-resolution microtubule structures reveal the structural transitions in alphabeta-tubulin upon GTP hydrolysis. Cell *157*, 1117-1129.

Arancibia, S., Silhol, M., Mouliere, F., Meffre, J., Hollinger, I., Maurice, T., and Tapia-Arancibia, L. (2008). Protective effect of BDNF against beta-amyloid induced neurotoxicity in vitro and in vivo in rats. Neurobiol Dis *31*, 316-326.

Ariosa, A.R., and Klionsky, D.J. (2016). Autophagy core machinery: overcoming spatial barriers in neurons. J Mol Med (Berl) *94*, 1217-1227.

Ashkenazi, A., Bento, C.F., Ricketts, T., Vicinanza, M., Siddiqi, F., Pavel, M., Squitieri, F., Hardenberg, M.C., Imarisio, S., Menzies, F.M*., et al.* (2017). Polyglutamine tracts regulate beclin 1-dependent autophagy. Nature *545*, 108-111.

Ashpole, N.M., Song, W., Brustovetsky, T., Engleman, E.A., Brustovetsky, N., Cummins, T.R., and Hudmon, A. (2012). Calcium/calmodulin-dependent protein kinase II (CaMKII) inhibition induces neurotoxicity via dysregulation of glutamate/calcium signaling and hyperexcitability. J Biol Chem *287*, 8495-8506.

Ayala, C.I., Kim, J., and Neufeld, T.P. (2018). Rab6 promotes insulin receptor and cathepsin trafficking to regulate autophagy induction and activity in Drosophila. J Cell Sci *131*.

Bakula, D., Muller, A.J., Zuleger, T., Takacs, Z., Franz-Wachtel, M., Thost, A.K., Brigger, D., Tschan, M.P., Frickey, T., Robenek, H*., et al.* (2017). WIPI3 and WIPI4 beta-propellers are scaffolds for LKB1-AMPK-TSC signalling circuits in the control of autophagy. Nat Commun *8*, 15637.

Beetz, C., Koch, N., Khundadze, M., Zimmer, G., Nietzsche, S., Hertel, N., Huebner, A.K., Mumtaz, R., Schweizer, M., Dirren, E*., et al.*(2013). A spastic paraplegia mouse model reveals REEP1-dependent ER shaping. J Clin Invest *123*, 4273-4282.

Beffert, U., Dillon, G.M., Sullivan, J.M., Stuart, C.E., Gilbert, J.P., Kambouris, J.A., and Ho, A. (2012). Microtubule plus-end tracking protein CLASP2 regulates neuronal polarity and synaptic function. J Neurosci *32*, 13906-13916.

Bekinschtein, P., Cammarota, M., Katche, C., Slipczuk, L., Rossato, J.I., Goldin, A., Izquierdo, I., and Medina, J.H. (2008). BDNF is essential to promote persistence of long-term memory storage. Proc Natl Acad Sci U S A *105*, 2711-2716.

Binotti, B., Pavlos, N.J., Riedel, D., Wenzel, D., Vorbruggen, G., Schalk, A.M., Kuhnel, K., Boyken, J., Erck, C., Martens, H.*, et al.* (2015). The GTPase Rab26 links synaptic vesicles to the autophagy pathway. Elife *4*, e05597.

Blum, R., and Konnerth, A. (2005). Neurotrophin-mediated rapid signaling in the central nervous system: mechanisms and functions. Physiology (Bethesda) *20*, 70-78.

Bradke, F., Fawcett, J.W., and Spira, M.E. (2012). Assembly of a new growth cone after axotomy: the precursor to axon regeneration. Nature Reviews Neuroscience *13*, 183.

Brunden, K.R., Lee, V.M., Smith, A.B., 3rd, Trojanowski, J.Q., and Ballatore, C. (2017). Altered microtubule dynamics in neurodegenerative disease: Therapeutic potential of microtubule-stabilizing drugs. Neurobiol Dis *105*, 328-335.

Burbach, G.J., Hellweg, R., Haas, C.A., Del Turco, D., Deicke, U., Abramowski, D., Jucker, M., Staufenbiel, M., and Deller, T. (2004). Induction of brain-derived neurotrophic factor in plaque-associated glial cells of aged APP23 transgenic mice. J Neurosci *24*, 2421-2430.

Burgin, K.E., Waxham, M.N., Rickling, S., Westgate, S.A., Mobley, W.C., and Kelly, P.T. (1990). In situ hybridization histochemistry of Ca2+/calmodulin-dependent protein kinase in developing rat brain. J Neurosci *10*, 1788-1798.

Cambray-Deakin, M.A., and Burgoyne, R.D. (1987). Posttranslational modifications of alpha-tubulin: acetylated and detyrosinated forms in axons of rat cerebellum. J Cell Biol *104*, 1569-1574.

Chiba, K., Yuki, S., Masataka, K., Toshiharu, S., and Seiich, U. (2014). Simple and Direct Assembly of Kymographs from Movies Using KYMOMAKER. Traffic *15*, 1-11.

Chollat, C., Lecointre, M., Leuillier, M., Remy-Jouet, I., Do Rego, J.C., Abily-Donval, L., Ramdani, Y., Richard, V., Compagnon, P., Dureuil, B.*, et al.* (2019). Beneficial Effects of Remifentanil Against Excitotoxic Brain Damage in Newborn Mice. Front Neurol *10*, 407.

Ciechanover, A. (2006). The ubiquitin proteolytic system: from a vague idea, through basic mechanisms, and onto human diseases and drug targeting. Neurology *66*, S7-19.

Ciechanover, A., and Stanhill, A. (2014). The complexity of recognition of ubiquitinated substrates by the 26S proteasome. Biochim Biophys Acta *1843*, 86-96.

Dahlstrand, J., Lardelli, M., and Lendahl, U. (1995). Nestin mRNA expression correlates with the central nervous system progenitor cell state in many, but not all, regions of developing central nervous system. Brain Res Dev Brain Res *84*, 109-129.

Dantuma, N.P., and Bott, L.C. (2014). The ubiquitin-proteasome system in neurodegenerative diseases: precipitating factor, yet part of the solution. Front Mol Neurosci *7*, 70.

Davis, C.H., Kim, K.Y., Bushong, E.A., Mills, E.A., Boassa, D., Shih, T., Kinebuchi, M., Phan, S., Zhou, Y., Bihlmeyer, N.A.*, et al.* (2014). Transcellular degradation of axonal mitochondria. Proc Natl Acad Sci U S A *111*, 9633-9638.

Dieni, S., Matsumoto, T., Dekkers, M., Rauskolb, S., Ionescu, M.S., Deogracias, R., Gundelfinger, E.D., Kojima, M., Nestel, S., Frotscher, M.*, et al.* (2012). BDNF and its pro-peptide are stored in presynaptic dense core vesicles in brain neurons. J Cell Biol *196*, 775-788.

Dillon, G.M., Tyler, W.A., Omuro, K.C., Kambouris, J., Tyminski, C., Henry, S., Haydar, T.F., Beffert, U., and Ho, A. (2017). CLASP2 Links Reelin to the Cytoskeleton during Neocortical Development. Neuron *93*, 1344-1358 e1345.

Dragatsis, I., and Zeitlin, S. (2000a). CaMKIIalpha-Cre transgene expression and recombination patterns in the mouse brain. Genesis *26*, 133-135.

Dragatsis, I., and Zeitlin, S. (2000b). CaMKIIα-cre transgene expression and recombination patterns in the mouse brain. Genesis *26*, 133-135.

Dubey, J., Ratnakaran, N., and Koushika, S.P. (2016). Corrigendum: Neurodegeneration and microtubule dynamics: death by a thousand cuts. Front Cell Neurosci *10*, 26.

Efimov, A., Kharitonov, A., Efimova, N., Loncarek, J., Miller, P.M., Andreyeva, N., Gleeson, P., Galjart, N., Maia, A.R., McLeod, I.X.*, et al.* (2007). Asymmetric CLASP-dependent nucleation of noncentrosomal microtubules at the trans-Golgi network. Dev Cell *12*, 917-930.

Emoto, K. (2016). Dendrites : development and disease, 1st edition. edn (New York, NY: Springer Berlin Heidelberg).

Erck, C., Peris, L., Andrieux, A., Meissirel, C., Gruber, A.D., Vernet, M., Schweitzer, A., Saoudi, Y., Pointu, H., Bosc, C.*, et al.*(2005). A vital role of tubulin-tyrosine-ligase for neuronal organization. Proc Natl Acad Sci U S A *102*, 7853-7858.

Erdmann, R., Wiebel, F.F., Flessau, A., Rytka, J., Beyer, A., Frohlich, K.U., and Kunau, W.H. (1991). PAS1, a yeast gene required for peroxisome biogenesis, encodes a member of a novel family of putative ATPases. Cell *64*, 499-510.

Farhy-Tselnicker, I., and Allen, N.J. (2018). Astrocytes, neurons, synapses: a tripartite view on cortical circuit development. Neural Dev *13*, 7.

Farias, G.G., Freal, A., Tortosa, E., Stucchi, R., Pan, X., Portegies, S., Will, L., Altelaar, M., and Hoogenraad, C.C. (2019). Feedback-Driven Mechanisms between Microtubules and the Endoplasmic Reticulum Instruct Neuronal Polarity. Neuron *102*, 184-201 e188.

Fassier, C., Tarrade, A., Peris, L., Courageot, S., Mailly, P., Dalard, C., Delga, S., Roblot, N., Lefevre, J., Job, D.*, et al.* (2013). Microtubule-targeting drugs rescue axonal swellings in cortical neurons from spastin knockout mice. Dis Model Mech *6*, 72-83.

Ferguson, S.M. (2019). Neuronal lysosomes. Neurosci Lett *697*, 1-9.

Fink, J.K. (2013). Hereditary spastic paraplegia: clinico-pathologic features and emerging molecular mechanisms. Acta Neuropathol *126*, 307-328.

Forth, S., and Kapoor, T.M. (2017). The mechanics of microtubule networks in cell division. J Cell Biol *216*, 1525-1531.

Frickey, T., and Lupas, A.N. (2004). Phylogenetic analysis of AAA proteins. J Struct Biol *146*, 2-10.

Friedman, J.R., Webster, B.M., Mastronarde, D.N., Verhey, K.J., and Voeltz, G.K. (2010). ER sliding dynamics and ER-mitochondrial contacts occur on acetylated microtubules. J Cell Biol *190*, 363-375.

Gadadhar, S., Bodakuntla, S., Natarajan, K., and Janke, C. (2017). The tubulin code at a glance. J Cell Sci *130*, 1347-1353.

Galluzzi, L., Baehrecke, E.H., Ballabio, A., Boya, P., Bravo-San Pedro, J.M., Cecconi, F., Choi, A.M., Chu, C.T., Codogno, P., Colombo, M.I.*, et al.* (2017). Molecular definitions of autophagy and related processes. EMBO J *36*, 1811-1836.

Galluzzi, L., Vitale, I., Aaronson, S.A., Abrams, J.M., Adam, D., Agostinis, P., Alnemri, E.S., Altucci, L., Amelio, I., Andrews, D.W.*, et al.* (2018). Molecular mechanisms of cell death: recommendations of the Nomenclature Committee on Cell Death 2018. Cell Death Differ *25*, 486-541.

Gauthier, L.R., Charrin, B.C., Borrell-Pages, M., Dompierre, J.P., Rangone, H., Cordelieres, F.P., De Mey, J., MacDonald, M.E., Lessmann, V., Humbert, S.*, et al.* (2004). Huntingtin controls neurotrophic support and survival of neurons by enhancing BDNF vesicular transport along microtubules. Cell *118*, 127-138.

Geeraert, C., Ratier, A., Pfisterer, S.G., Perdiz, D., Cantaloube, I., Rouault, A., Pattingre, S., Proikas-Cezanne, T., Codogno, P., and Pous, C. (2010). Starvation-induced hyperacetylation of tubulin is required for the stimulation of autophagy by nutrient deprivation. J Biol Chem *285*, 24184-24194.

Geetha, T., Seibenhener, M.L., Chen, L., Madura, K., and Wooten, M.W. (2008). p62 serves as a shuttling factor for TrkA interaction with the proteasome. Biochem Biophys Res Commun *374*, 33-37.

Geetha, T., and Wooten, M.W. (2008). TrkA receptor endolysosomal degradation is both ubiquitin and proteasome dependent. Traffic *9*, 1146-1156.

Geisert, E.E., Jr., Johnson, H.G., and Binder, L.I. (1990). Expression of microtubule-associated protein 2 by reactive astrocytes. Proc Natl Acad Sci U S A *87*, 3967-3971.

Ginty, D.D., and Segal, R.A. (2002). Retrograde neurotrophin signaling: Trk-ing along the axon. Curr Opin Neurobiol *12*, 268-274.

Goldberg, A.L. (2012). Development of proteasome inhibitors as research tools and cancer drugs. J Cell Biol *199*, 583-588.

Gornstein, E., and Schwarz, T.L. (2014). The paradox of paclitaxel neurotoxicity: Mechanisms and unanswered questions. Neuropharmacology *76 Pt A*, 175-183.

Gorski, J.A., Zeiler, S.R., Tamowski, S., and Jones, K.R. (2003). Brain-derived neurotrophic factor is required for the maintenance of cortical dendrites. J Neurosci *23*, 6856-6865.

Gregersen, N., Bross, P., Vang, S., and Christensen, J.H. (2006). Protein misfolding and human disease. Annu Rev Genomics Hum Genet *7*, 103-124.

Guertin, D.A., Stevens, D.M., Thoreen, C.C., Burds, A.A., Kalaany, N.Y., Moffat, J., Brown, M., Fitzgerald, K.J., and Sabatini, D.M. (2006). Ablation in mice of the mTORC components raptor, rictor, or mLST8 reveals that mTORC2 is required for signaling to Akt-FOXO and PKCalpha, but not S6K1. Dev Cell *11*, 859-871.

Gumy, L.F., and Hoogenraad, C.C. (2018). Local mechanisms regulating selective cargo entry and long-range trafficking in axons. Curr Opin Neurobiol *51*, 23-28.

Gurel, P.S., Hatch, A.L., and Higgs, H.N. (2014). Connecting the cytoskeleton to the endoplasmic reticulum and Golgi. Curr Biol *24*, R660-R672.

Haapasalo, A., Sipola, I., Larsson, K., Akerman, K.E., Stoilov, P., Stamm, S., Wong, G., and Castren, E. (2002). Regulation of TRKB surface expression by brain-derived neurotrophic factor and truncated TRKB isoforms. J Biol Chem *277*, 43160-43167.

Haglund, K., Di Fiore, P.P., and Dikic, I. (2003). Distinct monoubiquitin signals in receptor endocytosis. Trends Biochem Sci *28*, 598-603.

Haller, M., Hock, A.K., Giampazolias, E., Oberst, A., Green, D.R., Debnath, J., Ryan, K.M., Vousden, K.H., and Tait, S.W. (2014). Ubiquitination and proteasomal degradation of ATG12 regulates its proapoptotic activity. Autophagy *10*, 2269-2278.

Hamasaki, M., Furuta, N., Matsuda, A., Nezu, A., Yamamoto, A., Fujita, N., Oomori, H., Noda, T., Haraguchi, T., Hiraoka, Y*., et al.* (2013). Autophagosomes form at ER-mitochondria contact sites. Nature *495*, 389-393.

Hammerling, B.C., Najor, R.H., Cortez, M.Q., Shires, S.E., Leon, L.J., Gonzalez, E.R., Boassa, D., Phan, S., Thor, A., Jimenez, R.E*., et al.* (2017). A Rab5 endosomal pathway mediates Parkin-dependent mitochondrial clearance. Nat Commun *8*, 14050.

Hara, T., and Mizushima, N. (2009). Role of ULK-FIP200 complex in mammalian autophagy: FIP200, a counterpart of yeast Atg17? Autophagy *5*, 85-87.

Hara, T., Nakamura, K., Matsui, M., Yamamoto, A., Nakahara, Y., Suzuki-Migishima, R., Yokoyama, M., Mishima, K., Saito, I., Okano, H*., et al.* (2006). Suppression of basal autophagy in neural cells causes neurodegenerative disease in mice. Nature *441*, 885-889.

He, M., Ding, Y., Chu, C., Tang, J., Xiao, Q., and Luo, Z.G. (2016). Autophagy induction stabilizes microtubules and promotes axon regeneration after spinal cord injury. Proc Natl Acad Sci U S A *113*, 11324-11329.

Held, R.G., and Kaeser, P.S. (2018). ELKS active zone proteins as multitasking scaffolds for secretion. Open Biol *8*.

Hendrickson, M.L., Rao, A.J., Demerdash, O.N., and Kalil, R.E. (2011). Expression of nestin by neural cells in the adult rat and human brain. PLoS One *6*, e18535.

Hewett, J., Gonzalez-Agosti, C., Slater, D., Ziefer, P., Li, S., Bergeron, D., Jacoby, D.J., Ozelius, L.J., Ramesh, V., and Breakefield, X.O. (2000). Mutant torsinA, responsible for early-onset torsion dystonia, forms membrane inclusions in cultured neural cells. Hum Mol Genet *9*, 1403-1413.

Hirokawa, N., Niwa, S., and Tanaka, Y. (2010). Molecular motors in neurons: transport mechanisms and roles in brain function, development, and disease. Neuron *68*, 610-638.

Hohfeld, J., and Hoppe, T. (2018). Ub and Down: Ubiquitin Exercise for the Elderly. Trends Cell Biol *28*, 512-522.

Howard, J., and Hyman, A.A. (2003). Dynamics and mechanics of the microtubule plus end. Nature *422*, 753-758.

Hu, Z., Yang, B., Mo, X., and Xiao, H. (2015). Mechanism and Regulation of Autophagy and Its Role in Neuronal Diseases. Mol Neurobiol *52*, 1190-1209.

Ito, C., Saito, Y., Nozawa, T., Fujii, S., Sawa, T., Inoue, H., Matsunaga, T., Khan, S., Akashi, S., Hashimoto, R.*, et al.* (2013). Endogenous nitrated nucleotide is a key mediator of autophagy and innate defense against bacteria. Mol Cell *52*, 794-804.

Ivankovic, D., Drew, J., Lesept, F., White, I.J., Lopez Domenech, G., Tooze, S.A., and Kittler, J.T. (2019). Axonal autophagosome maturation defect through failure of ATG9A sorting underpins pathology in AP-4 deficiency syndrome. Autophagy, 1-17.

Janke, C., and Bulinski, J.C. (2011). Post-translational regulation of the microtubule cytoskeleton: mechanisms and functions. Nat Rev Mol Cell Biol *12*, 773-786.

Janke, C., and Kneussel, M. (2010). Tubulin post-translational modifications: encoding functions on the neuronal microtubule cytoskeleton. Trends Neurosci *33*, 362-372.

Janowski, B.A., Ling, N.C., Giustina, A., and Wehrenberg, W.B. (1993). Hypothalamic regulation of growth hormone secretion during food deprivation in the rat. Life Sci *52*, 981-987.

Jaworski, J., Kapitein, L.C., Gouveia, S.M., Dortland, B.R., Wulf, P.S., Grigoriev, I., Camera, P., Spangler, S.A., Di Stefano, P., Demmers, J.*, et al.* (2009). Dynamic Microtubules Regulate Dendritic Spine Morphology and Synaptic Plasticity. Neuron *61*, 85-100.

Joo, J.H., Wang, B., Frankel, E., Ge, L., Xu, L., Iyengar, R., Li-Harms, X., Wright, C., Shaw, T.I., Lindsten, T.*, et al.* (2016). The Noncanonical Role of ULK/ATG1 in ER-to-Golgi Trafficking Is Essential for Cellular Homeostasis. Mol Cell *62*, 491-506.

Jung, C.H., Jun, C.B., Ro, S.H., Kim, Y.M., Otto, N.M., Cao, J., Kundu, M., and Kim, D.H. (2009). ULK-Atg13-FIP200 complexes mediate mTOR signaling to the autophagy machinery. Mol Biol Cell *20*, 1992-2003.

Kabeya, Y., Mizushima, N., Ueno, T., Yamamoto, A., Kirisako, T., Noda, T., Kominami, E., Ohsumi, Y., and Yoshimori, T. (2000). LC3, a mammalian homologue of yeast Apg8p, is localized in autophagosome membranes after processing. EMBO J *19*, 5720-5728.

Kaiser, S.E., Riley, B.E., Shaler, T.A., Trevino, R.S., Becker, C.H., Schulman, H., and Kopito, R.R. (2011). Protein standard absolute quantification (PSAQ) method for the measurement of cellular ubiquitin pools. Nat Methods *8*, 691-696.

Kapitein, L.C., and Hoogenraad, C.C. (2015). Building the Neuronal Microtubule Cytoskeleton. Neuron *87*, 492-506.

Kast, D.J., and Dominguez, R. (2017). The Cytoskeleton-Autophagy Connection. Curr Biol *27*, R318-R326.

Katsumata, K., Nishiyama, J., Inoue, T., Mizushima, N., Takeda, J., and Yuzaki, M. (2010). Dynein- and activity-dependent retrograde transport of autophagosomes in neuronal axons. Autophagy *6*, 378-385.

Kaul, N., Soppina, V., and Verhey, K.J. (2014). Effects of alpha-tubulin K40 acetylation and detyrosination on kinesin-1 motility in a purified system. Biophys J *106*, 2636-2643.

Kaur, J., and Debnath, J. (2015). Autophagy at the crossroads of catabolism and anabolism. Nat Rev Mol Cell Biol *16*, 461-472.

Kevei, E., and Hoppe, T. (2014). Ubiquitin sets the timer: impacts on aging and longevity. Nat Struct Mol Biol *21*, 290-292.

Khaminets, A., Behl, C., and Dikic, I. (2016). Ubiquitin-Dependent And Independent Signals In Selective Autophagy. Trends Cell Biol *26*, 6-16.

Khaminets, A., Heinrich, T., Mari, M., Grumati, P., Huebner, A.K., Akutsu, M., Liebmann, L., Stolz, A., Nietzsche, S., Koch, N.*, et al.*(2015). Regulation of endoplasmic reticulum turnover by selective autophagy. Nature *522*, 354-358.

Kim, M., Sandford, E., Gatica, D., Qiu, Y., Liu, X., Zheng, Y., Schulman, B.A., Xu, J., Semple, I., Ro, S.H.*, et al.* (2016). Mutation in ATG5 reduces autophagy and leads to ataxia with developmental delay. Elife *5*.

Kishi-Itakura, C., Koyama-Honda, I., Itakura, E., and Mizushima, N. (2014). Ultrastructural analysis of autophagosome organization using mammalian autophagy-deficient cells. J Cell Sci *127*, 4089-4102.

Knoferle, J., Koch, J.C., Ostendorf, T., Michel, U., Planchamp, V., Vutova, P., Tonges, L., Stadelmann, C., Bruck, W., Bahr, M.*, et al.*(2010). Mechanisms of acute axonal degeneration in the optic nerve in vivo. Proc Natl Acad Sci U S A *107*, 6064-6069.

Komarova, Y., De Groot, C.O., Grigoriev, I., Gouveia, S.M., Munteanu, E.L., Schober, J.M., Honnappa, S., Buey, R.M., Hoogenraad, C.C., Dogterom, M.*, et al.* (2009). Mammalian end binding proteins control persistent microtubule growth. J Cell Biol *184*, 691-706.

Komatsu, M., Waguri, S., Chiba, T., Murata, S., Iwata, J., Tanida, I., Ueno, T., Koike, M., Uchiyama, Y., Kominami, E.*, et al.*(2006). Loss of autophagy in the central nervous system causes neurodegeneration in mice. Nature *441*, 880-884.

Komatsu, M., Waguri, S., Koike, M., Sou, Y.S., Ueno, T., Hara, T., Mizushima, N., Iwata, J., Ezaki, J., Murata, S.*, et al.* (2007a). Homeostatic levels of p62 control cytoplasmic inclusion body formation in autophagy-deficient mice. Cell *131*, 1149-1163.

Komatsu, M., Waguri, S., Ueno, T., Iwata, J., Murata, S., Tanida, I., Ezaki, J., Mizushima, N., Ohsumi, Y., Uchiyama, Y.*, et al.* (2005). Impairment of starvation-induced and constitutive autophagy in Atg7-deficient mice. J Cell Biol *169*, 425-434.

Komatsu, M., Wang, Q.J., Holstein, G.R., Friedrich, V.L., Jr., Iwata, J., Kominami, E., Chait, B.T., Tanaka, K., and Yue, Z. (2007b). Essential role for autophagy protein Atg7 in the maintenance of axonal homeostasis and the prevention of axonal degeneration. Proc Natl Acad Sci U S A *104*, 14489-14494.

Kondylis, V., Polykratis, A., Ehlken, H., Ochoa-Callejero, L., Straub, Beate K., Krishna-Subramanian, S., Van, T.-M., Curth, H.-M., Heise, N., Weih, F.*, et al.* (2015). NEMO Prevents Steatohepatitis and Hepatocellular Carcinoma by Inhibiting RIPK1 Kinase Activity-Mediated Hepatocyte Apoptosis. Cancer Cell *28*, 582-598.

Kononenko, N.L., Claßen, G.A., Kuijpers, M., Puchkov, D., Maritzen, T., Tempes, A., Malik, A.R., Skalecka, A., Bera, S., Jaworski, J.*, et al.* (2017a). Retrograde transport of TrkB-containing autophagosomes via the adaptor AP-2 mediates neuronal complexity and prevents neurodegeneration. Nature Communications *8*, 1-16.

Kononenko, N.L., Classen, G.A., Kuijpers, M., Puchkov, D., Maritzen, T., Tempes, A., Malik, A.R., Skalecka, A., Bera, S., Jaworski, J.*, et al.* (2017b). Retrograde transport of TrkB-containing autophagosomes via the adaptor AP-2 mediates neuronal complexity and prevents neurodegeneration. Nat Commun *8*, 14819.

Kononenko, N.L., Diril, M.K., Puchkov, D., Kintscher, M., Koo, S.J., Pfuhl, G., Winter, Y., Wienisch, M., Klingauf, J., Breustedt, J.*, et al.*(2013). Compromised fidelity of endocytic synaptic vesicle protein sorting in the absence of stonin 2. Proc Natl Acad Sci U S A *110*, E526-535.

Kononenko, N.L., and Haucke, V. (2015). Molecular mechanisms of presynaptic membrane retrieval and synaptic vesicle reformation. Neuron *85*, 484-496.

Koyuncu, S., Fatima, A., Gutierrez-Garcia, R., and Vilchez, D. (2017). Proteostasis of Huntingtin in Health and Disease. Int J Mol Sci *18*.

Ktistakis, N.T., and Tooze, S.A. (2016). Digesting the Expanding Mechanisms of Autophagy. Trends Cell Biol *26*, 624-635.

Kulkarni, A., Chen, J., and Maday, S. (2018). Neuronal autophagy and intercellular regulation of homeostasis in the brain. Curr Opin Neurobiol *51*, 29-36.

Kulkarni, V.V., and Maday, S. (2018). Neuronal endosomes to lysosomes: A journey to the soma. J Cell Biol *217*, 2977-2979.

Kuma, A., Komatsu, M., and Mizushima, N. (2017). Autophagy-monitoring and autophagy-deficient mice. Autophagy *13*, 1619-1628.

Labbadia, J., and Morimoto, R.I. (2015). The biology of proteostasis in aging and disease. Annu Rev Biochem *84*, 435-464.

Lacroix, B., van Dijk, J., Gold, N.D., Guizetti, J., Aldrian-Herrada, G., Rogowski, K., Gerlich, D.W., and Janke, C. (2010). Tubulin polyglutamylation stimulates spastin-mediated microtubule severing. J Cell Biol *189*, 945-954.

Lansbergen, G., Grigoriev, I., Mimori-Kiyosue, Y., Ohtsuka, T., Higa, S., Kitajima, I., Demmers, J., Galjart, N., Houtsmuller, A.B., Grosveld, F.*, et al.* (2006). CLASPs attach microtubule plus ends to the cell cortex through a complex with LL5beta. Dev Cell *11*, 21-32.

Lazarov, E., Dannemeyer, M., Feulner, B., Enderlein, J., Gutnick, M.J., Wolf, F., and Neef, A. (2018). An axon initial segment is required for temporal precision in action potential encoding by neuronal populations. Sci Adv *4*, eaau8621.

Le Bras, B., Chatzopoulou, E., Heydon, K., Martinez, S., Ikenaka, K., Prestoz, L., Spassky, N., Zalc, B., and Thomas, J.L. (2005). Oligodendrocyte development in the embryonic brain: the contribution of the plp lineage. Int J Dev Biol *49*, 209-220.

Lee, S., Sato, Y., and Nixon, R.A. (2011). Lysosomal proteolysis inhibition selectively disrupts axonal transport of degradative organelles and causes an Alzheimer's-like axonal dystrophy. J Neurosci *31*, 7817-7830.

Levine, B., and Kroemer, G. (2019). Biological Functions of Autophagy Genes: A Disease Perspective. Cell *176*, 11-42.

Liang, C.C., Wang, C., Peng, X., Gan, B., and Guan, J.L. (2010). Neural-specific deletion of FIP200 leads to cerebellar degeneration caused by increased neuronal death and axon degeneration. J Biol Chem *285*, 3499-3509.

Lindholm, D., Carroll, P., Tzimagiorgis, G., and Thoenen, H. (1996). Autocrine-paracrine regulation of hippocampal neuron survival by IGF-1 and the neurotrophins BDNF, NT-3 and NT-4. Eur J Neurosci *8*, 1452-1460.

Lindholm, D., Dechant, G., Heisenberg, C.P., and Thoenen, H. (1993). Brain-derived neurotrophic factor is a survival factor for cultured rat cerebellar granule neurons and protects them against glutamate-induced neurotoxicity. Eur J Neurosci *5*, 1455-1464.

Lipinski, M.M., Zheng, B., Lu, T., Yan, Z.Y., Py, B.F., Ng, A., Xavier, R.J., Li, C., Yankner, B.A., Scherzer, C.R.*, et al.* (2010). Genome-wide analysis reveals mechanisms modulating autophagy in normal brain aging and in Alzheimer's disease. P Natl Acad Sci USA *107*, 14164-14169.

Liu, C., Bickford, L.S., Held, R.G., Nyitrai, H., Sudhof, T.C., and Kaeser, P.S. (2014). The active zone protein family ELKS supports Ca2+ influx at nerve terminals of inhibitory hippocampal neurons. J Neurosci *34*, 12289-12303.

Lodato, S., and Arlotta, P. (2015). Generating neuronal diversity in the mammalian cerebral cortex. Annu Rev Cell Dev Biol *31*, 699-720.

Lu, B., Nagappan, G., Guan, X., Nathan, P.J., and Wren, P. (2013). BDNF-based synaptic repair as a disease-modifying strategy for neurodegenerative diseases. Nat Rev Neurosci *14*, 401-416.

Lu, Q., Yang, P., Huang, X., Hu, W., Guo, B., Wu, F., Lin, L., Kovacs, A.L., Yu, L., and Zhang, H. (2011). The WD40 repeat PtdIns(3)P-binding protein EPG-6 regulates progression of omegasomes to autophagosomes. Dev Cell *21*, 343-357.

Luarte, A., Cornejo, V.H., Bertin, F., Gallardo, J., and Couve, A. (2018). The axonal endoplasmic reticulum: One organelle-many functions in development, maintenance, and plasticity. Dev Neurobiol *78*, 181-208.

Ly, N., Elkhatib, N., Bresteau, E., Pietrement, O., Khaled, M., Magiera, M.M., Janke, C., Le Cam, E., Rutenberg, A.D., and Montagnac, G. (2016). alphaTAT1 controls longitudinal spreading of acetylation marks from open microtubules extremities. Sci Rep *6*, 35624.

Maday, S., and Holzbaur, E.L. (2014). Autophagosome biogenesis in primary neurons follows an ordered and spatially regulated pathway. Dev Cell *30*, 71-85.

Maday, S., and Holzbaur, E.L. (2016). Compartment-Specific Regulation of Autophagy in Primary Neurons. J Neurosci *36*, 5933-5945.

Maday, S., Twelvetrees, A.E., Moughamian, A.J., and Holzbaur, E.L. (2014). Axonal transport: cargo-specific mechanisms of motility and regulation. Neuron *84*, 292-309.

Maday, S., Wallace, K.E., and Holzbaur, E.L. (2012). Autophagosomes initiate distally and mature during transport toward the cell soma in primary neurons. J Cell Biol *196*, 407-417.

Madisen, L., Zwingman, T.A., Sunkin, S.M., Oh, S.W., Zariwala, H.A., Gu, H., Ng, L.L., Palmiter, R.D., Hawrylycz, M.J., Jones, A.R.*, et al.* (2010). A robust and high-throughput Cre reporting and characterization system for the whole mouse brain. Nat Neurosci *13*, 133-140.

Mann, S.S., and Hammarback, J.A. (1994). Molecular characterization of light chain 3. A microtubule binding subunit of MAP1A and MAP1B. J Biol Chem *269*, 11492-11497.

Marino, G., Niso-Santano, M., Baehrecke, E.H., and Kroemer, G. (2014). Self-consumption: the interplay of autophagy and apoptosis. Nat Rev Mol Cell Biol *15*, 81-94.

Matusica, D., and Coulson, E.J. (2014). Local versus long-range neurotrophin receptor signalling: endosomes are not just carriers for axonal transport. Semin Cell Dev Biol *31*, 57-63.

Mauthe, M., Orhon, I., Rocchi, C., Zhou, X., Luhr, M., Hijlkema, K.J., Coppes, R.P., Engedal, N., Mari, M., and Reggiori, F. (2018). Chloroquine inhibits autophagic flux by decreasing autophagosome-lysosome fusion. Autophagy *14*, 1435-1455.

McKenney, R.J., Huynh, W., Vale, R.D., and Sirajuddin, M. (2016). Tyrosination of alpha-tubulin controls the initiation of processive dynein-dynactin motility. EMBO J *35*, 1175-1185.

Melentijevic, I., Toth, M.L., Arnold, M.L., Guasp, R.J., Harinath, G., Nguyen, K.C., Taub, D., Parker, J.A., Neri, C., Gabel, C.V.*, et al.* (2017). C. elegans neurons jettison protein aggregates and mitochondria under neurotoxic stress. Nature *542*, 367-371.

Menzies, F.M., Fleming, A., Caricasole, A., Bento, C.F., Andrews, S.P., Ashkenazi, A., Fullgrabe, J., Jackson, A., Jimenez Sanchez, M., Karabiyik, C.*, et al.* (2017). Autophagy and Neurodegeneration: Pathogenic Mechanisms and Therapeutic Opportunities. Neuron *93*, 1015-1034.

Mercer, T.J., Gubas, A., and Tooze, S.A. (2018). A molecular perspective of mammalian autophagosome biogenesis. J Biol Chem *293*, 5386-5395.

Merianda, T.T., Lin, A.C., Lam, J.S., Vuppalanchi, D., Willis, D.E., Karin, N., Holt, C.E., and Twiss, J.L. (2009). A functional equivalent of endoplasmic reticulum and Golgi in axons for secretion of locally synthesized proteins. Mol Cell Neurosci *40*, 128-142.

Mignone, J.L., Kukekov, V., Chiang, A.S., Steindler, D., and Enikolopov, G. (2004). Neural stem and progenitor cells in nestin-GFP transgenic mice. J Comp Neurol *469*, 311-324.

Miki, H., Setou, M., Kaneshiro, K., and Hirokawa, N. (2001). All kinesin superfamily protein, KIF, genes in mouse and human. Proc Natl Acad Sci U S A *98*, 7004-7011.

Minagar, A., Barnett, M.H., Benedict, R.H., Pelletier, D., Pirko, I., Sahraian, M.A., Frohman, E., and Zivadinov, R. (2013). The thalamus and multiple sclerosis: modern views on pathologic, imaging, and clinical aspects. Neurology *80*, 210-219.

Mizushima, N., and Komatsu, M. (2011). Autophagy: renovation of cells and tissues. Cell *147*, 728-741.

Mizushima, N., and Levine, B. (2010). Autophagy in mammalian development and differentiation. Nat Cell Biol *12*, 823-830.

Mizushima, N., Yamamoto, A., Matsui, M., Yoshimori, T., and Ohsumi, Y. (2004). In vivo analysis of autophagy in response to nutrient starvation using transgenic mice expressing a fluorescent autophagosome marker. Mol Biol Cell *15*, 1101-1111.

Mochida, K., Oikawa, Y., Kimura, Y., Kirisako, H., Hirano, H., Ohsumi, Y., and Nakatogawa, H. (2015). Receptor-mediated selective autophagy degrades the endoplasmic reticulum and the nucleus. Nature *522*, 359-362.

Monier, S., Jollivet, F., Janoueix-Lerosey, I., Johannes, L., and Goud, B. (2002). Characterization of novel Rab6-interacting proteins involved in endosome-to-TGN transport. Traffic *3*, 289-297.

Moutaux, E., Christaller, W., Scaramuzzino, C., Genoux, A., Charlot, B., Cazorla, M., and Saudou, F. (2018). Neuronal network maturation differently affects secretory vesicles and mitochondria transport in axons. Sci Rep *8*, 13429.

Muller, R., Heinrich, M., Heck, S., Blohm, D., and Richter-Landsberg, C. (1997). Expression of microtubule-associated proteins MAP2 and tau in cultured rat brain oligodendrocytes. Cell Tissue Res *288*, 239-249.

Murray, S.S., Wong, A.W., Yang, J., Li, Y., Putz, U., Tan, S.S., and Howitt, J. (2019). Ubiquitin Regulation of Trk Receptor Trafficking and Degradation. Mol Neurobiol *56*, 1628-1636.

Nagahara, A.H., and Tuszynski, M.H. (2011). Potential therapeutic uses of BDNF in neurological and psychiatric disorders. Nat Rev Drug Discov *10*, 209-219.

Nedelsky, N.B., Todd, P.K., and Taylor, J.P. (2008). Autophagy and the ubiquitin-proteasome system: collaborators in neuroprotection. Biochim Biophys Acta *1782*, 691-699.

Nguyen, T.N., Padman, B.S., Usher, J., Oorschot, V., Ramm, G., and Lazarou, M. (2016). Atg8 family LC3/GABARAP proteins are crucial for autophagosome-lysosome fusion but not autophagosome formation during PINK1/Parkin mitophagy and starvation. J Cell Biol *215*, 857-874.

Ni, H.M., Bockus, A., Wozniak, A.L., Jones, K., Weinman, S., Yin, X.M., and Ding, W.X. (2011). Dissecting the dynamic turnover of GFP-LC3 in the autolysosome. Autophagy *7*, 188-204.

Nikoletopoulou, V., Sidiropoulou, K., Kallergi, E., Dalezios, Y., and Tavernarakis, N. (2017). Modulation of Autophagy by BDNF Underlies Synaptic Plasticity. Cell Metab *26*, 230-242 e235.

Nishida, Y., Arakawa, S., Fujitani, K., Yamaguchi, H., Mizuta, T., Kanaseki, T., Komatsu, M., Otsu, K., Tsujimoto, Y., and Shimizu, S. (2016). Corrigendum: Discovery of Atg5/Atg7-independent alternative macroautophagy. Nature *533*, 130.

Nishiyama, J., Miura, E., Mizushima, N., Watanabe, M., and Yuzaki, M. (2007). Aberrant membranes and double-membrane structures accumulate in the axons of Atg5-null Purkinje cells before neuronal death. Autophagy *3*, 591-596.

Niwa, H., Yamamura, K., and Miyazaki, J. (1991). Efficient selection for high-expression transfectants with a novel eukaryotic vector. Gene *108*, 193-199.

Nunez, J. (1988). Immature and mature variants of MAP2 and tau proteins and neuronal plasticity. Trends Neurosci *11*, 477-479.

Oh, W.J., and Jacinto, E. (2011). mTOR complex 2 signaling and functions. Cell Cycle *10*, 2305-2316.

Okerlund, N.D., Schneider, K., Leal-Ortiz, S., Montenegro-Venegas, C., Kim, S.A., Garner, L.C., Waites, C.L., Gundelfinger, E.D., Reimer, R.J., and Garner, C.C. (2017). Bassoon Controls Presynaptic Autophagy through Atg5. Neuron *93*, 897-913 e897.

Palikaras, K., Lionaki, E., and Tavernarakis, N. (2018). Mechanisms of mitophagy in cellular homeostasis, physiology and pathology. Nat Cell Biol *20*, 1013-1022.

Pandey, U.B., Nie, Z., Batlevi, Y., McCray, B.A., Ritson, G.P., Nedelsky, N.B., Schwartz, S.L., DiProspero, N.A., Knight, M.A., Schuldiner, O*., et al.* (2007). HDAC6 rescues neurodegeneration and provides an essential link between autophagy and the UPS. Nature *447*, 859-863.

Panja, D., Kenney, J.W., D'Andrea, L., Zalfa, F., Vedeler, A., Wibrand, K., Fukunaga, R., Bagni, C., Proud, C.G., and Bramham, C.R. (2014). Two-stage translational control of dentate gyrus LTP consolidation is mediated by sustained BDNF-TrkB signaling to MNK. Cell Rep *9*, 1430-1445.

Park, H., and Poo, M.M. (2013). Neurotrophin regulation of neural circuit development and function. Nat Rev Neurosci *14*, 7-23.

Park, S.H., Zhu, P.P., Parker, R.L., and Blackstone, C. (2010). Hereditary spastic paraplegia proteins REEP1, spastin, and atlastin-1 coordinate microtubule interactions with the tubular ER network. J Clin Invest *120*, 1097-1110.

Perlin, J.B., Churn, S.B., Lothman, E.W., and DeLorenzo, R.J. (1992). Loss of type II calcium/calmodulin-dependent kinase activity correlates with stages of development of electrographic seizures in status epilepticus in rat. Epilepsy Res *11*, 111-118.

Philippidou, P., Valdez, G., Akmentin, W., Bowers, W.J., Federoff, H.J., and Halegoua, S. (2011). Trk retrograde signaling requires persistent, Pincher-directed endosomes. Proc Natl Acad Sci U S A *108*, 852-857.

Polson, H.E., de Lartigue, J., Rigden, D.J., Reedijk, M., Urbe, S., Clague, M.J., and Tooze, S.A. (2010). Mammalian Atg18 (WIPI2) localizes to omegasome-anchored phagophores and positively regulates LC3 lipidation. Autophagy *6*, 506-522.

Poon, W.W., Blurton-Jones, M., Tu, C.H., Feinberg, L.M., Chabrier, M.A., Harris, J.W., Jeon, N.L., and Cotman, C.W. (2011). beta-Amyloid impairs axonal BDNF retrograde trafficking. Neurobiol Aging *32*, 821-833.

Price, J.L., and Drevets, W.C. (2010). Neurocircuitry of mood disorders. Neuropsychopharmacology *35*, 192-216.

Qiang, L., Yu, W., Andreadis, A., Luo, M., and Baas, P.W. (2006). Tau protects microtubules in the axon from severing by katanin. J Neurosci *26*, 3120-3129.

Raybin, D., and Flavin, M. (1977). Enzyme which specifically adds tyrosine to the alpha chain of tubulin. Biochemistry *16*, 2189-2194.

Remondelli, P., and Renna, M. (2017). The Endoplasmic Reticulum Unfolded Protein Response in Neurodegenerative Disorders and Its Potential Therapeutic Significance. Front Mol Neurosci *10*, 187.

Ren, Y., Jiang, H., Hu, Z., Fan, K., Wang, J., Janoschka, S., Wang, X., Ge, S., and Feng, J. (2015). Parkin mutations reduce the complexity of neuronal processes in iPSC-derived human neurons. Stem Cells *33*, 68-78.

Riley, B.E., Kaiser, S.E., Shaler, T.A., Ng, A.C., Hara, T., Hipp, M.S., Lage, K., Xavier, R.J., Ryu, K.Y., Taguchi, K*., et al.* (2010). Ubiquitin accumulation in autophagy-deficient mice is dependent on the Nrf2-mediated stress response pathway: a potential role for protein aggregation in autophagic substrate selection. J Cell Biol *191*, 537-552.

Romanov, J., Walczak, M., Ibiricu, I., Schuchner, S., Ogris, E., Kraft, C., and Martens, S. (2012). Mechanism and functions of membrane binding by the Atg5-Atg12/Atg16 complex during autophagosome formation. EMBO J *31*, 4304-4317.

Rubinsztein, D.C. (2006). The roles of intracellular protein-degradation pathways in neurodegeneration. Nature *443*, 780-786.

Rubinsztein, D.C., Marino, G., and Kroemer, G. (2011). Autophagy and aging. Cell *146*, 682-695.

Rubinsztein, D.C., Shpilka, T., and Elazar, Z. (2012). Mechanisms of autophagosome biogenesis. Curr Biol *22*, R29-34.

Saftig, P., and Klumperman, J. (2009). Lysosome biogenesis and lysosomal membrane proteins: trafficking meets function. Nat Rev Mol Cell Biol *10*, 623-635.

Saitsu, H., Nishimura, T., Muramatsu, K., Kodera, H., Kumada, S., Sugai, K., Kasai-Yoshida, E., Sawaura, N., Nishida, H., Hoshino, A*., et al.* (2013). De novo mutations in the autophagy gene WDR45 cause static encephalopathy of childhood with neurodegeneration in adulthood. Nat Genet *45*, 445-449, 449e441.

Salvadores, N., Sanhueza, M., Manque, P., and Court, F.A. (2017). Axonal Degeneration during Aging and Its Functional Role in Neurodegenerative Disorders. Front Neurosci-Switz *11*.

Sanchez-Huertas, C., and Luders, J. (2015). The augmin connection in the geometry of microtubule networks. Curr Biol *25*, R294-299.

Saper, C.B. (2000). Hypothalamic connections with the cerebral cortex. Prog Brain Res *126*, 39-48.

Sarkar, S. (2013). Regulation of autophagy by mTOR-dependent and mTOR-independent pathways: autophagy dysfunction in neurodegenerative diseases and therapeutic application of autophagy enhancers. Biochem Soc Trans *41*, 1103-1130.

Sasi, M., Vignoli, B., Canossa, M., and Blum, R. (2017). Neurobiology of local and intercellular BDNF signaling. Pflugers Arch *469*, 593-610.

Schonecker, S., Neuhofer, C., Otto, M., Ludolph, A., Kassubek, J., Landwehrmeyer, B., Anderl-Straub, S., Semler, E., Diehl-Schmid, J., Prix, C*., et al.*(2018). Atrophy in the Thalamus But Not Cerebellum Is Specific for C9orf72 FTD and ALS Patients - An Atlas-Based Volumetric MRI Study. Front Aging Neurosci *10*, 45.

Sharma, N., Kosan, Z.A., Stallworth, J.E., Berbari, N.F., and Yoder, B.K. (2011a). Soluble levels of cytosolic tubulin regulate ciliary length control. Mol Biol Cell *22*, 806-816.

Sharma, N., Kosan, Z.A., Stallworth, J.E., Berbari, N.F., and Yoder, B.K. (2011b). Soluble levels of cytosolic tubulin regulate ciliary length control. Molecular Biology of the Cell *22*, 806-816.

Sharp, D.J., and Ross, J.L. (2012). Microtubule-severing enzymes at the cutting edge. J Cell Sci *125*, 2561-2569.

Shen, W., and Ganetzky, B. (2009). Autophagy promotes synapse development in Drosophila. J Cell Biol *187*, 71-79.

Shimada, I.S., LeComte, M.D., Granger, J.C., Quinlan, N.J., and Spees, J.L. (2012). Self-renewal and differentiation of reactive astrocyte-derived neural stem/progenitor cells isolated from the cortical peri-infarct area after stroke. J Neurosci *32*, 7926-7940.

Singh, A., Saha, T., Begemann, I., Ricker, A., Nusse, H., Thorn-Seshold, O., Klingauf, J., Galic, M., and Matis, M. (2018). Polarized microtubule dynamics directs cell mechanics and coordinates forces during epithelial morphogenesis. Nat Cell Biol *20*, 1126-1133.

Slipczuk, L., Bekinschtein, P., Katche, C., Cammarota, M., Izquierdo, I., and Medina, J.H. (2009). BDNF activates mTOR to regulate GluR1 expression required for memory formation. PLoS One *4*, e6007.

Smith, B.N., Ticozzi, N., Fallini, C., Gkazi, A.S., Topp, S., Kenna, K.P., Scotter, E.L., Kost, J., Keagle, P., Miller, J.W*., et al.* (2014). Exome-wide rare variant analysis identifies TUBA4A mutations associated with familial ALS. Neuron *84*, 324-331.

Snyder, H., Mensah, K., Theisler, C., Lee, J., Matouschek, A., and Wolozin, B. (2003). Aggregated and monomeric alpha-synuclein bind to the S6' proteasomal protein and inhibit proteasomal function. J Biol Chem *278*, 11753-11759.

Song, Y., and Brady, S.T. (2015). Post-translational modifications of tubulin: pathways to functional diversity of microtubules. Trends Cell Biol *25*, 125-136.

Soto, C., and Satani, N. (2011). The intricate mechanisms of neurodegeneration in prion diseases. Trends Mol Med *17*, 14-24.

Sou, Y.S., Waguri, S., Iwata, J., Ueno, T., Fujimura, T., Hara, T., Sawada, N., Yamada, A., Mizushima, N., Uchiyama, Y*., et al.*(2008). The Atg8 conjugation system is indispensable for proper development of autophagic isolation membranes in mice. Mol Biol Cell *19*, 4762-4775.

Soykan, T., Kaempf, N., Sakaba, T., Vollweiter, D., Goerdeler, F., Puchkov, D., Kononenko, N.L., and Haucke, V. (2017). Synaptic Vesicle Endocytosis Occurs on Multiple Timescales and Is Mediated by Formin-Dependent Actin Assembly. Neuron *93*, 854-866 e854.

Stavoe, A.K., Hill, S.E., Hall, D.H., and Colon-Ramos, D.A. (2016). KIF1A/UNC-104 Transports ATG-9 to Regulate Neurodevelopment and Autophagy at Synapses. Dev Cell *38*, 171-185.

Stepanova, T., Slemmer, J., Hoogenraad, C.C., Lansbergen, G., Dortland, B., De Zeeuw, C.I., Grosveld, F., van Cappellen, G., Akhmanova, A., and Galjart, N. (2003). Visualization of microtubule growth in cultured neurons via the use of EB3-GFP (end-binding protein 3-green fluorescent protein). J Neurosci *23*, 2655-2664.

Stiess, M., Maghelli, N., Kapitein, L.C., Gomis-Ruth, S., Wilsch-Brauninger, M., Hoogenraad, C.C., Tolic-Norrelykke, I.M., and Bradke, F. (2010). Axon extension occurs independently of centrosomal microtubule nucleation. Science *327*, 704-707.

Stifani, N. (2014). Motor neurons and the generation of spinal motor neuron diversity. Frontiers in Cellular Neuroscience *8*, 1-22.

Sweeney, H.L., and Holzbaur, E.L.F. (2018). Motor Proteins. Cold Spring Harb Perspect Biol *10*.

Takei, N., Inamura, N., Kawamura, M., Namba, H., Hara, K., Yonezawa, K., and Nawa, H. (2004). Brain-derived neurotrophic factor induces mammalian target of rapamycin-dependent local activation of translation machinery and protein synthesis in neuronal dendrites. J Neurosci *24*, 9760-9769.

Tan, J.M., Wong, E.S., Kirkpatrick, D.S., Pletnikova, O., Ko, H.S., Tay, S.P., Ho, M.W., Troncoso, J., Gygi, S.P., Lee, M.K*., et al.* (2008). Lysine 63-linked ubiquitination promotes the formation and autophagic clearance of protein inclusions associated with neurodegenerative diseases. Hum Mol Genet *17*, 431-439.

Tandon, P., Yang, Y., Das, K., Holmes, G.L., and Stafstrom, C.E. (1999). Neuroprotective effects of brain-derived neurotrophic factor in seizures during development. Neuroscience *91*, 293-303.

Tarrade, A., Fassier, C., Courageot, S., Charvin, D., Vitte, J., Peris, L., Thorel, A., Mouisel, E., Fonknechten, N., Roblot, N*., et al.* (2006). A mutation of spastin is responsible for swellings and impairment of transport in a region of axon characterized by changes in microtubule composition. Hum Mol Genet *15*, 3544-3558.

Tas, R.P., Chazeau, A., Cloin, B.M.C., Lambers, M.L.A., Hoogenraad, C.C., and Kapitein, L.C. (2017). Differentiation between Oppositely Oriented Microtubules Controls Polarized Neuronal Transport. Neuron *96*, 1264-1271 e1265.

Tas, R.P., and Kapitein, L.C. (2018). Exploring cytoskeletal diversity in neurons. Science *361*, 231-232.

Teixido-Travesa, N., Roig, J., and Luders, J. (2012). The where, when and how of microtubule nucleation - one ring to rule them all. J Cell Sci *125*, 4445-4456.

Tekirdag, K., and Cuervo, A.M. (2018). Chaperone-mediated autophagy and endosomal microautophagy: Joint by a chaperone. J Biol Chem *293*, 5414-5424.

Terenzio, M., Schiavo, G., and Fainzilber, M. (2017). Compartmentalized Signaling in Neurons: From Cell Biology to Neuroscience. Neuron *96*, 667-679.

Tirnauer, J.S., and Bierer, B.E. (2000). EB1 proteins regulate microtubule dynamics, cell polarity, and chromosome stability. J Cell Biol *149*, 761-766.

Tong, L., and Perez-Polo, R. (1998). Brain-derived neurotrophic factor (BDNF) protects cultured rat cerebellar granule neurons against glucose deprivation-induced apoptosis. J Neural Transm *105*, 905-914.

Tsien, J.Z., Chen, D.F., Gerber, D., Tom, C., Mercer, E.H., Anderson, D.J., Mayford, M., Kandel, E.R., and Tonegawa, S. (1996). Subregion- and cell type-restricted gene knockout in mouse brain. Cell *87*, 1317-1326.

Tsuboyama, K., Koyama-Honda, I., Sakamaki, Y., Koike, M., Morishita, H., and Mizushima, N. (2016). The ATG conjugation systems are important for degradation of the inner autophagosomal membrane. Science *354*, 1036-1041.

Tuvikene, J., Pruunsild, P., Orav, E., Esvald, E.E., and Timmusk, T. (2016). AP-1 Transcription Factors Mediate BDNF-Positive Feedback Loop in Cortical Neurons. J Neurosci *36*, 1290-1305.

Uemura, T., Yamamoto, M., Kametaka, A., Sou, Y.S., Yabashi, A., Yamada, A., Annoh, H., Kametaka, S., Komatsu, M., and Waguri, S. (2014). A cluster of thin tubular structures mediates transformation of the endoplasmic reticulum to autophagic isolation membrane. Mol Cell Biol *34*, 1695-1706.

Valdes, V., Valenzuela, J.I., Salas, D.A., Jaureguiberry-Bravo, M., Otero, C., Thiede, C., Schmidt, C.F., and Couve, A. (2012). Endoplasmic reticulum sorting and kinesin-1 command the targeting of axonal GABAB receptors. PLoS One *7*, e44168.

van Beuningen, S.F.B., Will, L., Harterink, M., Chazeau, A., van Battum, E.Y., Frias, C.P., Franker, M.A.M., Katrukha, E.A., Stucchi, R., Vocking, K.*, et al.* (2015). TRIM46 Controls Neuronal Polarity and Axon Specification by Driving the Formation of Parallel Microtubule Arrays. Neuron *88*, 1208-1226.

Vijayan, V., and Verstreken, P. (2017). Autophagy in the presynaptic compartment in health and disease. J Cell Biol *216*, 1895-1906.

Wang, D., Chan, C.C., Cherry, S., and Hiesinger, P.R. (2013a). Membrane trafficking in neuronal maintenance and degeneration. Cell Mol Life Sci *70*, 2919-2934.

Wang, D., Xu, Q., Yuan, Q., Jia, M., Niu, H., Liu, X., Zhang, J., Young, C.Y., and Yuan, H. (2019). Proteasome inhibition boosts autophagic degradation of ubiquitinated-AGR2 and enhances the antitumor efficiency of bevacizumab. Oncogene *38*, 3458-3474.

Wang, J.T., Medress, Z.A., and Barres, B.A. (2012). Axon degeneration: molecular mechanisms of a self-destruction pathway. J Cell Biol *196*, 7-18.

Wang, L., Chang, X., She, L., Xu, D., Huang, W., and Poo, M.M. (2015). Autocrine action of BDNF on dendrite development of adult-born hippocampal neurons. J Neurosci *35*, 8384-8393.

Wang, X., Zhang, C., Szabo, G., and Sun, Q.Q. (2013b). Distribution of CaMKIIalpha expression in the brain in vivo, studied by CaMKIIalpha-GFP mice. Brain Res *1518*, 9-25.

Wang, Y., Liu, X., Biederer, T., and Sudhof, T.C. (2002). A family of RIM-binding proteins regulated by alternative splicing: Implications for the genesis of synaptic active zones. Proc Natl Acad Sci U S A *99*, 14464-14469.

Wang, Y.C., Lauwers, E., and Verstreken, P. (2017). Presynaptic protein homeostasis and neuronal function. Curr Opin Genet Dev *44*, 38-46.

Waterman-Storer, C.M., and Salmon, E.D. (1998). Endoplasmic reticulum membrane tubules are distributed by microtubules in living cells using three distinct mechanisms. Curr Biol *8*, 798-806.

Watson, F.L., Heerssen, H.M., Bhattacharyya, A., Klesse, L., Lin, M.Z., and Segal, R.A. (2001). Neurotrophins use the Erk5 pathway to mediate a retrograde survival response. Nat Neurosci *4*, 981-988.

Webb, J.L., Ravikumar, B., Atkins, J., Skepper, J.N., and Rubinsztein, D.C. (2003). Alpha-Synuclein is degraded by both autophagy and the proteasome. J Biol Chem *278*, 25009-25013.

White, J., Johannes, L., Mallard, F., Girod, A., Grill, S., Reinsch, S., Keller, P., Tzschaschel, B., Echard, A., Goud, B.*, et al.* (1999). Rab6 coordinates a novel Golgi to ER retrograde transport pathway in live cells. J Cell Biol *147*, 743-760.

Wiegert, J.S., Bengtson, C.P., and Bading, H. (2007). Diffusion and not active transport underlies and limits ERK1/2 synapse-to-nucleus signaling in hippocampal neurons. J Biol Chem *282*, 29621-29633.

Wilhelm, B.G., Mandad, S., Truckenbrodt, S., Krohnert, K., Schafer, C., Rammner, B., Koo, S.J., Classen, G.A., Krauss, M., Haucke, V.*, et al.*(2014). Composition of isolated synaptic boutons reveals the amounts of vesicle trafficking proteins. Science *344*, 1023-1028.

Witte, H., Neukirchen, D., and Bradke, F. (2008). Microtubule stabilization specifies initial neuronal polarization. J Cell Biol *180*, 619-632.

Wu, Y., Whiteus, C., Xu, C.S., Hayworth, K.J., Weinberg, R.J., Hess, H.F., and De Camilli, P. (2017). Contacts between the endoplasmic reticulum and other membranes in neurons. Proc Natl Acad Sci U S A *114*, E4859-E4867.

Xi, Y., Dhaliwal, J.S., Ceizar, M., Vaculik, M., Kumar, K.L., and Lagace, D.C. (2016). Knockout of Atg5 delays the maturation and reduces the survival of adult-generated neurons in the hippocampus. Cell Death Dis *7*, e2127.

Yamaguchi, J., Suzuki, C., Nanao, T., Kakuta, S., Ozawa, K., Tanida, I., Saitoh, T., Sunabori, T., Komatsu, M., Tanaka, K.*, et al.* (2018). Atg9a deficiency causes axon-specific lesions including neuronal circuit dysgenesis. Autophagy *14*, 764-777.

Yang, Y., Coleman, M., Zhang, L., Zheng, X., and Yue, Z. (2013). Autophagy in axonal and dendritic degeneration. Trends Neurosci *36*, 418-428.

Yao, I., Takagi, H., Ageta, H., Kahyo, T., Sato, S., Hatanaka, K., Fukuda, Y., Chiba, T., Morone, N., Yuasa, S.*, et al.* (2007). SCRAPPER-dependent ubiquitination of active zone protein RIM1 regulates synaptic vesicle release. Cell *130*, 943-957.

Yau, K.W., Schatzle, P., Tortosa, E., Pages, S., Holtmaat, A., Kapitein, L.C., and Hoogenraad, C.C. (2016). Dendrites In Vitro and In Vivo Contain Microtubules of Opposite Polarity and Axon Formation Correlates with Uniform Plus-End-Out Microtubule Orientation. J Neurosci *36*, 1071-1085.

Yau, K.W., van Beuningen, S.F., Cunha-Ferreira, I., Cloin, B.M., van Battum, E.Y., Will, L., Schatzle, P., Tas, R.P., van Krugten, J., Katrukha, E.A.*, et al.* (2014). Microtubule minus-end binding protein CAMSAP2 controls axon specification and dendrite development. Neuron *82*, 1058-1073.

Yazdankhah, M., Farioli-Vecchioli, S., Tonchev, A.B., Stoykova, A., and Cecconi, F. (2014). The autophagy regulators Ambra1 and Beclin 1 are required for adult neurogenesis in the brain subventricular zone. Cell Death Dis *5*, e1403.

Yoshii, S.R., Kuma, A., and Mizushima, N. (2017). Transgenic rescue of Atg5-null mice from neonatal lethality with neuron-specific expression of ATG5: Systemic analysis of adult Atg5-deficient mice. Autophagy *13*, 763-764.

Young, J.E., Martinez, R.A., and La Spada, A.R. (2009). Nutrient deprivation induces neuronal autophagy and implicates reduced insulin signaling in neuroprotective autophagy activation. J Biol Chem *284*, 2363-2373.

Yu, L., Chen, Y., and Tooze, S.A. (2018). Autophagy pathway: Cellular and molecular mechanisms. Autophagy *14*, 207-215.

Zang, S., Ali, Y.O., Ruan, K., and Zhai, R.G. (2013). Nicotinamide mononucleotide adenylyltransferase maintains active zone structure by stabilizing Bruchpilot. EMBO Rep *14*, 87-94.

Zempel, H., Dennissen, F., Kumar, Y., Luedtke, J., Biernat, J., Mandelkow, E.-M., and Mandelkow, E. (2017). Axodendritic sorting and pathological missorting of Tau is isoform specific and determined by axon initial segment architecture. Journal of Biological Chemistry.

Zempel, H., and Mandelkow, E. (2014). Lost after translation: missorting of Tau protein and consequences for Alzheimer disease. Trends Neurosci *37*, 721-732.

Zhang, R., Alushin, G.M., Brown, A., and Nogales, E. (2015). Mechanistic Origin of Microtubule Dynamic Instability and Its Modulation by EB Proteins. Cell *162*, 849-859.

Zhao, Y.G., Sun, L., Miao, G., Ji, C., Zhao, H., Sun, H., Miao, L., Yoshii, S.R., Mizushima, N., Wang, X.*, et al.* (2015). The autophagy gene Wdr45/Wipi4 regulates learning and memory function and axonal homeostasis. Autophagy *11*, 881-890.

Zheng, Q., Huang, T., Zhang, L., Zhou, Y., Luo, H., Xu, H., and Wang, X. (2016). Dysregulation of Ubiquitin-Proteasome System in Neurodegenerative Diseases. Front Aging Neurosci *8*, 303.

9. PUBLICATIONS

Publications

Negrete-Hurtado, A., Overhoff, M., Bera, S. *et al.* Autophagy lipidation machinery regulates axonal microtubule dynamics but is dispensable for survival of mammalian neurons. *Nat Commun* **11,** 1535 (2020). https://doi.org/10.1038/s41467-020-15287-9

Bera S., Camblor-Perujo S., Calleja-Barca E., **Negrete-Hurtado A**., *et al*. AP-2 prevents amyloidogenesis by promoting BACE1 trafficking and degradation in neurons. *EMBO Rep* vol. 21,6 (2020). https://doi.org/10.15252/embr.201947954

AKNOWLEDGEMENTS

Foremost all I would like to thank my supervisor Dr. Natalia L. Kononenko, who gave me the opportunity to work in her group. She has provided me an excellent guidance and motivational discussions, and taught me many lessons about how to be a better scientist. I really feel that I have evolved a lot since the first time I stepped in the lab, and this is mostly thanks to her.

I thank Prof. Dr Thorsten Hoppe and Prof. Dr Matthias Hammerschmidt who kindly agreed to take part of my dissertation defense, as well as to Prof Dr Elena Rugarli and Prof. Dr Brunhilde Wirth, for their feedbacks as members of my thesis advisory committee. I acknowledge Dr Min Kye for her constant advice and help during the developing of this project, and the contribution of Dr Vangelis Kondylis.

I deeply appreciate the nice and professional support from CECAD's facilities, mostly from the Animal and Imaging facilities. In addition, I am grateful with the doctoral programme Research Training Network- Neural Circuit Analysis on the Cellular and Subcellular Level (RTG-NCA). They provided me a complete structural programme in all aspects of neurosciences, and an excellent support for attending seminars and conferences.

Finally, yet importantly, I am very thankful to all members from Kononenko's lab, including the former ones, who always supported me in the bad and good times. Especially to Melina Overhoff and Sujoy Bera, for their big contribution in this work, and Nina Ellrich and Marvin Schäfer for expert technical assistance.

EIDESSTATTLICHE ERKLÄRUNG

Ich versichere, dass ich die von mir vorgelegte Dissertation selbständig angefertigt, die benutzten Quellen und Hilfsmittel vollständig angegeben und die Stellen der Arbeit − einschließlich Tabellen, Karten und Abbildungen −, die anderen Werken im Wortlaut oder dem Sinn nach entnommen sind, in jedem Einzelfall als Entlehnung kenntlich gemacht habe; dass diese Dissertation noch keiner anderen Fakultät oder Universität zur Prüfung vorgelegen hat; dass sie − abgesehen von unten angegebenen Teilpublikationen − noch nicht veröffentlicht worden ist, sowie, dass ich eine solche Veröffentlichung vor Abschluss des Promotionsverfahrens nicht vornehmen werde. Die Bestimmungen der Promotionsordnung sind mir bekannt. Die von mir vorgelegte Dissertation ist von Dr Natalia L. Kononenko betreut worden.

Teilpublikationen sind in Kapitel 8 angegeben

Ich versichere, dass ich all Angaben wahrheitsgemäß nach bestem Wissen und Gewissen gemacht habe und verpflichte mich, jedmögliche, die obigen Angaben betreffende Veränderungen dem Promotionsausschuss unverzüglich